Charged-Particle Production in Au+Au Collisions at $\sqrt{s_{NN}} = 130$ GeV and $\sqrt{s_{NN}} = 200$ GeV

Hironori Ito

Abstract

Charged-particle production in the pseudorapidity range $|\eta| < 4.7$ has been measured for Au+Au collisions at $\sqrt{s_{NN}}$ = 130 GeV and 200 GeV using several subcomponents of the BRAHMS experiment at the Relativistic Heavy-Ion Collider (RHIC). A coaxial arrangement of silicon strip and scintillator tile detectors determined particle production near mid-rapidity ($|\eta| < 3$). Two arrays of Cherenkov radiators mounted to photomultiplier tubes established the charged-particle yields at larger pseudorapidities. Additionally, a time-projection chamber at the front of a movable mid-rapidity spectrometer arm was used for an independent confirmation of the results. The charged-particle pseudorapidity density at midrapidity, $dN_{ch}/d\eta|_{\eta=0}$, is found to be 553 ± 36 and 625 ± 55 at 130 GeV and 200 GeV, respectively. Also, the total numbers of charged particles within the pseudorapidity range $|\eta| < 4.7$ was established as 3860±300 and 4630±370 at the two energies, respectively. The observed charged-particle density scaled by the number of participant pairs, $\frac{dN_{ch}}{d\eta}\frac{2}{<N_{part}>}$, is found to increase 13% from the lower to higher energy. Comparing the scaled Au+Au pseudorapidity density at $\sqrt{s_{NN}}$ = 200 GeV/A to p+$\bar{\text{p}}$ collision results, an increase of 40% is observed. The observed level of particle production is in the range expected if conditions are met for the production of a Quark-Gluon Plasma. These results constrain the current understanding of particle production at RHIC energies.

Dedication

To my wife, Sarah, who supported me patiently during the entire time spent on this work.

Acknowledgment

First of all, I would like to thank Dr. Stephen Sanders for providing me the opportunity to work on the BRAHMS experiment. Through this experiment, he has taught me about the very basics of the experimental physics all the way to the intricacy of leading-edge nuclear physics.

Secondly, I would like to thank Pat De Lurgio who designed the amplifier electronics for this project. He was my classmate for undergraduate and graduate courses, and he is the person who invited me to join the nuclear group. I really enjoyed working with him on this project. Also, I would like to thank Allen Hase and Bruce Janus for their excellent work in machining many of our detector systems. Their amazing skills made this project successful.

I would also like to thank all of the people from Brookhaven National Laboratory. During the three years I spent on the BRAHMS experiment, their expert advice and in-depth knowledge have helped me learn the entire project inside and out. I particularly enjoyed listening to their insightful stories.

Last but not least, I would like to thank my parents who gave me the freedom to do the things I wanted to do. Without their entire support, I would not have been able to do this work.

Contents

List of Figures

List of Tables

Chapter 1

Introduction

1.1 A Brief History up to the Finding of Quarks

Of what and how is our world made? This seems to be one of the many questions that the human race has been asking since the dawn of civilization. In the Greek era, Aristotle thought it was made up of water, air, fire and earth. In the theory by Leucippus and Democritus, the world consisted of "a-toma", which is the Greek word for a thing that can not be divided. While developing many great theories without any concrete proof, these men's interests did not stop at pondering the structure of their world. They also studied how to make new substances from known matters. Since the Egyptian era of the Great Pyramid, alchemists had been hard at work mixing several materials to form new substances.

The human race's fascination with new substances continued through the Middle Age to the era of the Industrial Revolution. In 1869, the Russian chemist Dimitri Mendelïev constructed a chemical table that classified all of the chemical elements known at that time according to their chemical properties. Later, this table was used to classify atoms according to their atomic numbers. In 1897, while chemists were busy finding new elements predicted by the atomic table, British physicist J. J. Thomson discovered the electron by the study of cathode rays [1]. This discovery, in which an atom is not a fundamental point-like element but has some inner structures, opened a new era for physics, and it led to the current branches of atomic, solid state, nuclear and particle physics. Obviously, the study of the structures of atoms became a very popular subject at the turn of the 20th Century: Japanese physicist Hantaro Nagaoka

developed a Saturn-like model of atomic structure, proposing that is a ring of negatively charged particles of the same mass circling around an attractive center [2]. J. J. Thomson developed an alternative idea of atomic structures, based on having a number of negatively-charged electrons (or corpuscles) being enclosed in a sphere of uniform positive objects [3, 4].

Following Thomson, British/New Zealander Ernest Rutherford, who studied under Thomson for two years, presented his idea of atomic structures [5, 6] after his students, Hans Geiger and Ernest Marsden, discovered the large deflection of alpha particles by a thin gold foil [7, 8]. Rutherford's idea was that an atom consists of a point-like positive charge surrounded by a spherical distribution of negative charge of an equal amount. In 1913, Danish physicist Niels Bohr supported this idea by developing an explanation based on quantum mechanics [9]. With the discovery of the electron and the proton, there was one more missing element, the neutron. It was known that for many atoms, the mass number of an atom was almost twice its atomic number. However, this was not the case for all atoms, which puzzled physicists at that time. To solve this puzzle, in 1920 Rutherford predicted the existence of the neutron, which is a neutral particle with the same mass as a proton. However, it took another twelve years for this particle to be discovered by a student of Rutherford, James Chadwick [10, 11].

After the discovery of the neutron, it seemed that the subatomic domain was fully explored. This was not the case, as shown with the prediction and discovery of the positron by British theoretical physicist Paul Dirac [12] and American experimental physicist Carl Anderson[13]. This lead to the idea of anti-matter. For example, the positron is the anti-matter partner of the electron and the anti-proton is the anti-matter partner of the proton. Also, to describe the mechanism of a proton and neutron bound together inside an atom, Yukawa postulated the meson theory of the strong force and, based on this theory, postulated the existence of a new particle [14]. This particle, called the pion, was discovered in 1947 by a group from Bristol [15] with the use of a cloud chamber to detect cosmic rays. This discovery occured after Carl Anderson and Seth Neddermeyer earlier in 1937 misidentified muons as the mediator of the strong force.

While the theory of atomic structure using quantum mechanics was established in the early Twentieth Century, the experimental bases relied on relatively low energy particles from natural decays of atoms in the laboratory and cosmic rays. In the early 1930s there were two American inventions that propelled this field into the "atom-smashing" business: the Van der Graaff ac-

celerator by Robert J. Van der Graaff and the cyclotron accelerator by E. O. Lawrence. With these inventions, it became possible to make particles of a specified energy and to smash these particles into targets. With further improvements, these inventions set the course for the second half of the 20th Century, where machines were constructed to produce particles of specific characteristics at ever higher energies.

Man's curiosity for an understanding of matter did not stop at finding the pion. Soon after, the kaon, lambda, and other particles were found. With this many particles it became very difficult to comprehend how the proton, neutron, electron, and pion could be "the" fundamental particles. In 1961, just as Mendelïev made his atomic table, Murray Gell-Mann [16] and Yuval Ne'eman [17] independently constructed a table, named the "Eightfold Way" by Gell-Mann, to list baryons and mesons systematically according to two quantum numbers: strangeness and charge. Later, to explain the underlying reason for this table, Gell-Mann [18] and Zweig independently proposed a quark model of matter. In this model, a meson such as a pion is made of two quarks, whereas a baryon such as a proton consists of three quarks. At the time, they proposed three quarks: up, down, and strange. The model later added three more quarks: charm, top, and bottom. Strong experimental evidence for the model came in 1969 by a group from the Massachusetts Institute of Technology and the Stanford Linear Accelerator Center. Just as Rutherford and his students found the constituent of atoms by hitting an alpha particle into a gold atom, this group hit an electron into a hydrogen atom to study the inner workings of a proton [19, 20]. The conclusion was that the proton has some inner structures.

1.2 Quark-Gluon Soup

The story of the search for "Of what and how is the world made?" did not end by finding quarks since the detailed mechanism of the strong force, which holds protons and neutrons inside a nucleus, is still not well known. The main problem for this understanding is caused by "quark confinement," which states that a single free quark cannot be detected because it is physically more favorable to produce a couple of quarks bound together than a single free-flying quark. The further complication is that, unlike a photon (the mediator of the electromagnetic force that holds electrons around a nucleus), a gluon (the mediator of the strong force) cannot be detected in isolation. However, these problems did not reduce our curiosity but rather aroused

greater fascination.

One loophole of this quark confinement is that although quarks interact very strongly at a large distance, they interact weakly when they are close to each other, a phenomena known as "asymptotic freedom" [21]. In 1975, J. C. Collins and M. J. Perry suggested that although there are no free quarks under normal conditions, it is possible that the condition for deconfinement could exist in neutron star cores, in exploding black holes, or may have been present in the early Big Bang Universe [22]. Any hadrons under these conditions of extremely high density and/or temperature would be forced to overlap one another. Under such conditions, quarks that make up the hadrons would be very close to each other and would interact weakly because of asymptotic freedom. This matter can be treated as free quarks and gluons, a so-called "quark soup".

Obviously, the experimental study of such extreme conditions appears to be very difficult. The closest, known neutron star and black hole to the earth are located at 200 and 1600 light years away, respectively. Because of their tremendous distances as well as their complexities, the experimental study of quarks and gluons within these objects is currently quite limited. The use of the Big Bang would be even more complex due in part to the fact that the current estimated age of our universe is 15 billion years old and the epoc when free quarks and gluons were presented is believed to have ended about 1 ns after the Big Bang. As a result, it is necessary to explore other methods to exploit this loophole to study this state of matter.

1.3 Man-Made Quark Gluon Plasma

The suggestion of how to make a quark gluon plasma (QGP) that can be studied through experiments came in the mid 70s to early 80s. It was suggested that a QGP could be formed by the use of relativistic heavy-ion collisions in an accelerator [23, 24, 25, 26]. Such collisions can produce a large number of particles in a single collision, and it is believed that this large particle production is the key for creating a QGP.

As early as the late 1940s, it was predicted that many particles could be produced in a single nucleon-nucleon collision if the collision energy were sufficiently high [27, 28]. In 1950, a group from the University of Chicago found evidence of multi-particle production in emulsion experiments with cosmic rays [29]. This phenomena led Enrico Fermi in 1950, and Landau in

1956 to describe a mechanism of particle production in terms of a statistical picture. Although this predates the quark model, the basic idea is still valid.

The basic picture of a relativistic heavy-ion collision is shown in Figure 1.1. When two nuclei are approaching for a collision, in the center-of-mass frame the longitudinal sizes of the nuclei are reduced because of their relativistic Lorentz contraction.

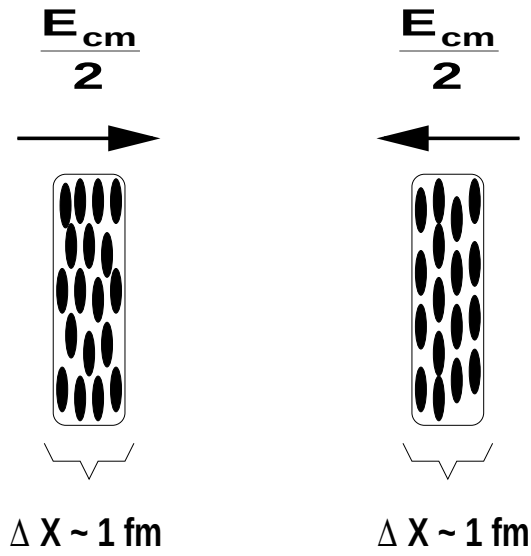

Figure 1.1: Two nuclei are approaching one another in the center-of-mass frame with relativistic speed.

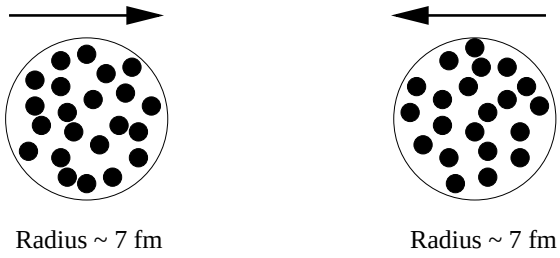

Figure 1.2: Two gold ions are approaching one another with non-relativistic speed.

Therefore, instead of a picture of two spherical balls (shown in Figure 1.2), the colliding nuclei appear as two approaching pancakes.

During the collision of two heavy-ions, constituent nucleons of one nucleus collide with those of other nucleus. Calculations suggest that there could be over 1000 nucleon-nucleon collisions in a single collision of two gold ions. While each nucleon-nucleon collision reduces the momentum

of the participating nucleons, because of the large momentum of the incoming nuclei, most of the nucleons inside the nuclei still have significant momentum by the time the nuclei finish passing through each other, as shown in Figure 1.3. In the central region of the collision, there can be

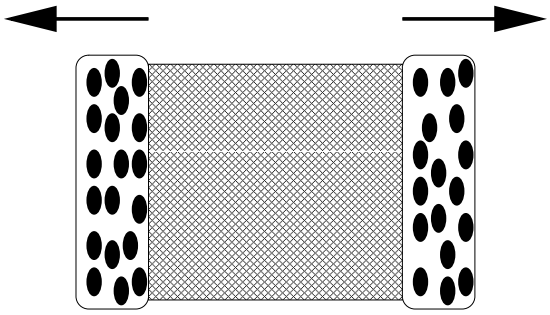

Figure 1.3: Two nuclei after a collision. The shaded region represents the heat produced by a collision.

left behind a very hot space heated by energy losses of the incoming nucleons. In this picture, this central region is relatively free of baryons.

1.4 Can Curiosity Kill Mankind?

In the 1980s, as the interest in this new quark-gluon matter increased, the construction of a relativistic heavy ion collider (RHIC) was proposed (shown in Figure 1.4) at Brookhaven National Laboratory (BNL) on Long Island using some facilities of a previously failed project called ISABELL, which was to produce proton-to-proton collisions. In the early 1990s, the

Figure 1.4: Aerial photo of RHIC

construction of the RHIC facility was approved by the Department of Energy, with the goal of

building the highest energy, heavy-ion collider in existence. It was designed to produce a beam of gold ions with a speed reaching 99.95 % of the speed of light. During the period of design and construction for this one-of-a-kind machine, there were a number of problems that had to be overcome. But, one that is very interesting scientifically and that received the attention of many people outside of the physics community delt with the fear that RHIC could destroy mankind.

This fear first surfaced in the "Letters to the Editor" section of the 1999 July issue of Scientific American magazine. Readers were responding to a previous article "A Little Big Bang" and expressed concern that while physicists were eager to create a QGP, they might create something unpredicted such as a black hole, which could eventually destroy the Earth. Soon, there was a flurry of articles around the world: the Sunday London Times had an article "Big Bang Machine Could Destroy Earth." The initial scientific response to the question did not help to ease the concern since it raised the possibility of "strangelets", which are hypothetical small lumps of strange matter, though it did try to reject the possibility of the creation of a black hole. The question of "unforeseen consequences" seemed to be a reasonable one, and Frank Wilczek, who responded initially to the public concern said, "scientists must take such possibilities very seriously–even if the risks seem remote–because an error might have devastating consequences." Therefore, just as Fermi and others considered whether a nuclear explosion might ignite a nuclear reaction in the atmosphere during the Manhattan Project, it was reasonable to consider the possibility of disaster scenarios at RHIC.

To assure the public safety, John Marburer, Director of BNL at that time, asked a group of physicists to review this issue. In their report, they considered three scenarios and estimated the probability of a dangerous event for each scenario by the extensive use of the worst case analysis with cosmic-ray data [30]. The three conditions they looked at are: gravitational singularities, vacuum instability and strangelets. They showed that with the current knowledge of physics, the possibility of a single disastrous event was so small that RHIC was highly unlikely to lead to the destruction of the Earth. More quantitatively, they stated that a chance of the single disastrous event would be less than one in 10^{21} over the lifetime of RHIC. With this assurance, RHIC became operational in 2000 with two-thirds full energy and it achieved collisions at full energy in 2001.

1.5 Brief View of the RHIC Experimental Setup

In the RHIC projects, there are four experiments working simultaneously around the storage ring of the heavy ion beam. They are designed so that all groups measure some of the same things for consistency, with each group having a more specific focus to explore various aspects of relativistic heavy ion collisions. In discussing the phase-space coverage of each of the four experiment below, it is convenient to use the terminology of "rapidity" and "pseudorapidity". These terms are fully discussed in Section 2.1. For the present discussion, it is sufficient to note that mid-rapidity refers to a particle emission angle of 90 degrees with respect to the beam axis.

1.5.1 BRAHMS

The BRAHMS project is one of two small collaborations at RHIC. A schematic view of the apparatus is shown in Figure 1.5. The experiment is designed to cover extended regions of charged-particle emission angle and transverse momentum with two spectrometer arms that can be rotated about the nominal collision vertex.

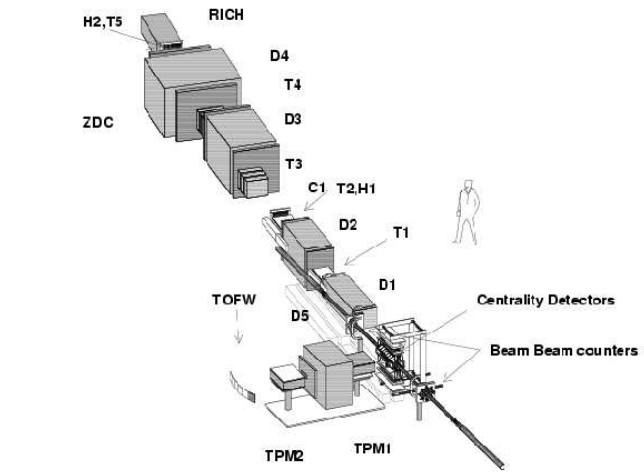

Figure 1.5: Brahms Detectors

1.5.2 PHENIX

The PHENIX project hosts the largest collaboration at RHIC. A schematic view of their detectors are shown in Figure 1.6. The main advantage of their enormous detectors is the ability to measure the productions of dileptons created by a QGP.

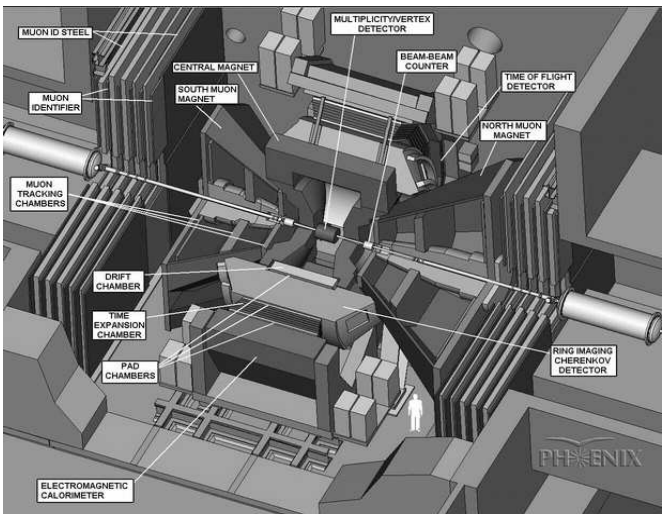

Figure 1.6: PHENIX Detectors

1.5.3 PHOBOS

The PHOBOS project is the other small collaboration. It is a "table-top" size apparatus consisting of a large set of microstrip silicon detectors. The schematic view of the detectors are shown in Figure 1.7. The main advantage of this project is its ability to measure charged-particle multiplicities with a very large pseudorapidity coverage.

1.5.4 STAR

The STAR project is the other "big" experiment at RHIC. The principal detector is a very large Time-Projection Chamber (TPC) that surrounds the beam pipe (shown Figure 1.8). The STAR project is able to measure particle tracks in a complete 2 π azimuthal coverage near mid-rapidity.

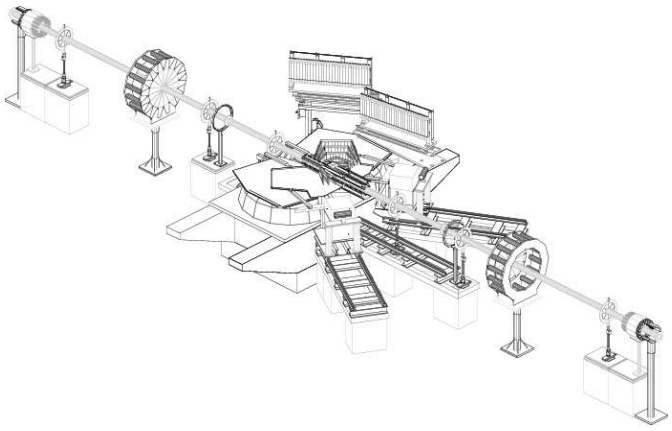

Figure 1.7: Phobos Detectors

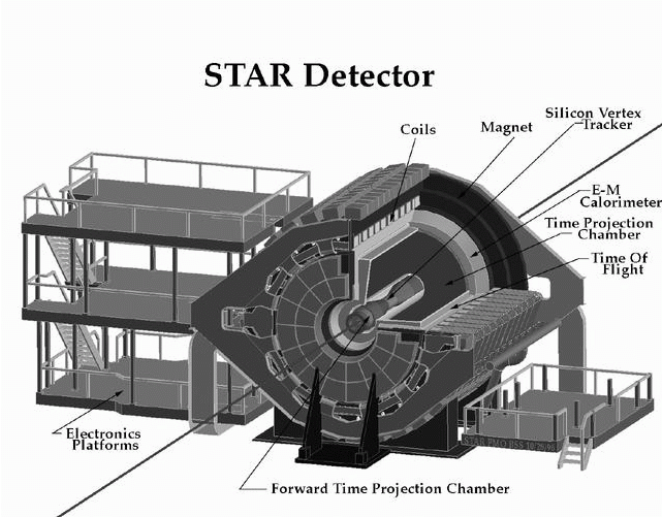

Figure 1.8: Star Detectors

1.6 Charged-Particle Multiplicity Measurement at BRAHMS

With the operation of the relativistic heavy-ion collider, the hope of producing a quark-gluon plasma is becoming ever closer. One of the key elements in producing this elusive matter is the large number of nucleon-nucleon collisions associated with the reaction, which leads to the large number of observed charged particles from a single heavy-ion collision. Hence, the number of charged-particles emitted from the relativistic heavy-ion collision can provide global information about its reaction mechanism. As a result, in this analysis, the level of charged-particle production in Au+Au collision at $\sqrt{s_{NN}} = 130$ GeV and $\sqrt{s_{NN}} = 200$ GeV has been systematically studied using the detector systems of BRAHMS. The experimental results are compared to several theoretical model calculations as well as other experimental results at different energies.

The present analysis is organized in the following manner. Chapter 2 provides the theoretical background for a quark-gluon plasma. Chapter 3 shows the brief overview of the BRAHMS detector subsystems. Chapter 4 provides detailed information about three detector systems primarily used for measuring the number of charged particle at BRAHMS: the Silicon Strip Detector Array (SiMA), the Scintillation Tile Detector Array (TMA) and the Beam-Beam Counter arrays (BBC). Techniques used for determining the collision vertex are discussed in Chapter 5. The chapter includes discussion of the efficiency and the resolutions achieved with the different vertex measurements. Calibration methods used for the SiMA, TMA and BBC detectors are fully discussed in Chapter 6. Chapter 7 shows how event multiplicity and centrality are determined. Chapter 8 provides observed production levels of charged particles, and compares them with theoretical calculations and other experimental results at different energies. A brief summary of the main conclusions is presented in Chapter 9.

Chapter 2

Theory

2.1 Definition of Kinetic Variables

In the realm of high-energy physics, certain kinematic variables are very useful for describing the relativistic dynamics. One of the most commonly encountered variables to describe the motion of a particle is the rapidity y, defined as

$$y = \frac{1}{2} \ln \left(\frac{p_0 + p_z c}{p_0 - p_z c} \right) \tag{2.1}$$

where

$$\begin{aligned} p_0 &\equiv \text{energy of the particle, and} \\ p_z &\equiv \text{longitudinal momentum of the particle.} \end{aligned}$$

Using Equation 2.1, one finds

$$e^{y} = \sqrt{\frac{p_0 + p_z c}{p_0 - p_z c}} \tag{2.2}$$

$$e^{-y} = \sqrt{\frac{p_0 - p_z c}{p_0 + p_z c}} \quad . \tag{2.3}$$

By adding and subtracting these expressions,

$$\frac{e^y + e^{-y}}{2} = \frac{1}{2}\left(\sqrt{\frac{p_0 + p_z c}{p_0 - p_z c}} + \sqrt{\frac{p_0 - p_z c}{p_0 + p_z c}}\right) = \frac{p_0}{\sqrt{p_0^2 - p_z^2 c^2}} \quad , \text{ and} \tag{2.4}$$

$$\frac{e^y - e^{-y}}{2} = \frac{1}{2}\left(\sqrt{\frac{p_0 + p_z c}{p_0 - p_z c}} - \sqrt{\frac{p_0 - p_z c}{p_0 + p_z c}}\right) = \frac{p_z c}{\sqrt{p_0^2 - p_z^2 c^2}} \quad . \tag{2.5}$$

Since the mass, energy and momentum of a particle will follow

$$p_0^2 = \mathbf{p}^2 c^2 + m^2 c^4 = p_T^2 c^2 + p_z^2 c^2 + m^2 c^4 = p_z^2 c^2 + m_T^2 c^4 \tag{2.6}$$

where

$$\begin{aligned} p_T &\equiv \text{transverse momentum of the particle} \\ m_T &\equiv \text{transverse mass of the particle} \end{aligned}$$

the above equations can be written as

$$p_0 = m_T c^2 \cosh y \quad , \text{ and} \tag{2.7}$$

$$p_z c = m_T c^2 \sinh y \quad . \tag{2.8}$$

A related variable is the pseudorapidity η defined as

$$\eta = -\ln\left[\tan\left(\frac{\theta}{2}\right)\right] \tag{2.9}$$

$$= \frac{1}{2}\ln\left(\frac{|\mathbf{p}| + p_z}{|\mathbf{p}| - p_z}\right) \tag{2.10}$$

where θ is angle between the momentum of the particle and the beam axis. The reason for using this variable rather than rapidity is that it only requires knowledge of the particle's emission angle, θ, whereas the rapidity requires knowledge of the particle's mass and momentum. Comparing Equation 2.10 with Equation 2.1, one finds that at very high energy $\eta \approx y$. Following

the rapidity analysis,

$$\frac{e^{\eta}+e^{-\eta}}{2}=\frac{1}{2}\left(\sqrt{\frac{|\mathbf{p}|+p_z}{|\mathbf{p}|-p_z}}+\sqrt{\frac{|\mathbf{p}|-p_z}{|\mathbf{p}|+p_z}}\right)=\frac{|\mathbf{p}|}{\sqrt{|\mathbf{p}|^2-p_z^2}} \tag{2.11}$$

and

$$\frac{e^{\eta}-e^{-\eta}}{2}=\frac{1}{2}\left(\sqrt{\frac{|\mathbf{p}|+p_z}{|\mathbf{p}|-p_z}}-\sqrt{\frac{|\mathbf{p}|-p_z}{|\mathbf{p}|+p_z}}\right)=\frac{p_z}{\sqrt{|\mathbf{p}|^2-p_z^2}} \quad . \tag{2.12}$$

Then, in terms of p_T

$$|\mathbf{p}| = p_T\cosh\eta \quad , \tag{2.13}$$

$$p_z = p_T\sinh\eta \quad . \tag{2.14}$$

Using Equation 2.7, 2.8, 2.13 and 2.14, the rapidity and pseudorapidity can be related to each other as

$$y = \frac{1}{2}\ln\left[\frac{\sqrt{p_T^2\cosh^2\eta+m^2}+p_T\sinh\eta}{\sqrt{p_T^2\cosh^2\eta+m^2}-p_T\sinh\eta}\right] \quad , \text{ and} \tag{2.15}$$

$$\eta = \frac{1}{2}\ln\left[\frac{\sqrt{m_T^2\cosh^2 y-m^2}+m_T\sinh y}{\sqrt{m_T^2\cosh^2 y-m^2}-m_T\sinh y}\right] \quad . \tag{2.16}$$

Differentiating the last equation gives

$$d\eta=\sqrt{\frac{m_T^2\cosh^2 y}{m_T^2\cosh^2 y-m^2}}dy \quad , \tag{2.17}$$

or,

$$\frac{1}{d\eta}=\sqrt{1-\frac{m^2}{m_T^2\cosh^2 y}}\frac{1}{dy} \quad . \tag{2.18}$$

From this last equation, it is clear that pseudorapidity densities, $\frac{dN}{d\eta}$, are close to rapidity densities, $\frac{dN}{dy}$, with the maximum deviation occuring in the region where y is close to zero. It is easy to see that $\frac{dN}{d\eta}$ is a bit smaller than $\frac{dN}{dy}$ for y close to zero. (The difference between $\frac{dN}{d\eta}$ and $\frac{dN}{dy}$ for y equal to zero can be about 20% according to the Hijing model discussed in a later chapter.)

2.2 Estimation of Initial Energy Density by Bjorken

As shown in Figure 1.1, two ions with pancake shapes of about 1 fm in thickness approach each other before a collision at RHIC energies. The longitudinal velocity of a particle emerging from the collision can be written as (now taking $c = 1$)

$$\begin{aligned} v_z &= \frac{p_z}{p_0} && (2.19)\\ &= \frac{m_T \sinh y}{m_T \cosh y} && (2.20)\\ &= \tanh y && (2.21)\\ &= \frac{z}{t} \quad . && (2.22) \end{aligned}$$

Therefore, by defining the proper time τ as

$$\tau = \sqrt{t^2 - z^2} \quad , \tag{2.23}$$

parametric expressions can be developed for the longitudinal displacement of the particle at time t in terms of the rapidity variable, with

$$\begin{aligned} z &= \tau \sinh y \quad , \text{ and} && (2.24)\\ t &= \tau \cosh y \quad . && (2.25) \end{aligned}$$

These results lead to an interesting consequence. For a certain value of τ, a small value in y is associated with small values in z and t. Since a small value in y indicates a slow particle, the consequence of the proper time is that the slower particles along the beam direction are the first ones to emerge, and that the faster particles emerge later after the collision [31] as a consequence of the Lorentz time dilation. This picture of particle production is called "inside-outside cascade" and its space-time picture is shown Figure 2.1

Using this picture, Bjorken estimated the initial energy density of the QGP in the following way [25, 32]: Consider the volume element $\mathcal{A}\Delta z$ around $z = 0$, where $\mathcal{A}$ is the cross sectional area of the QGP about the beam axis. Taking ΔN as the number of particles in this volume,

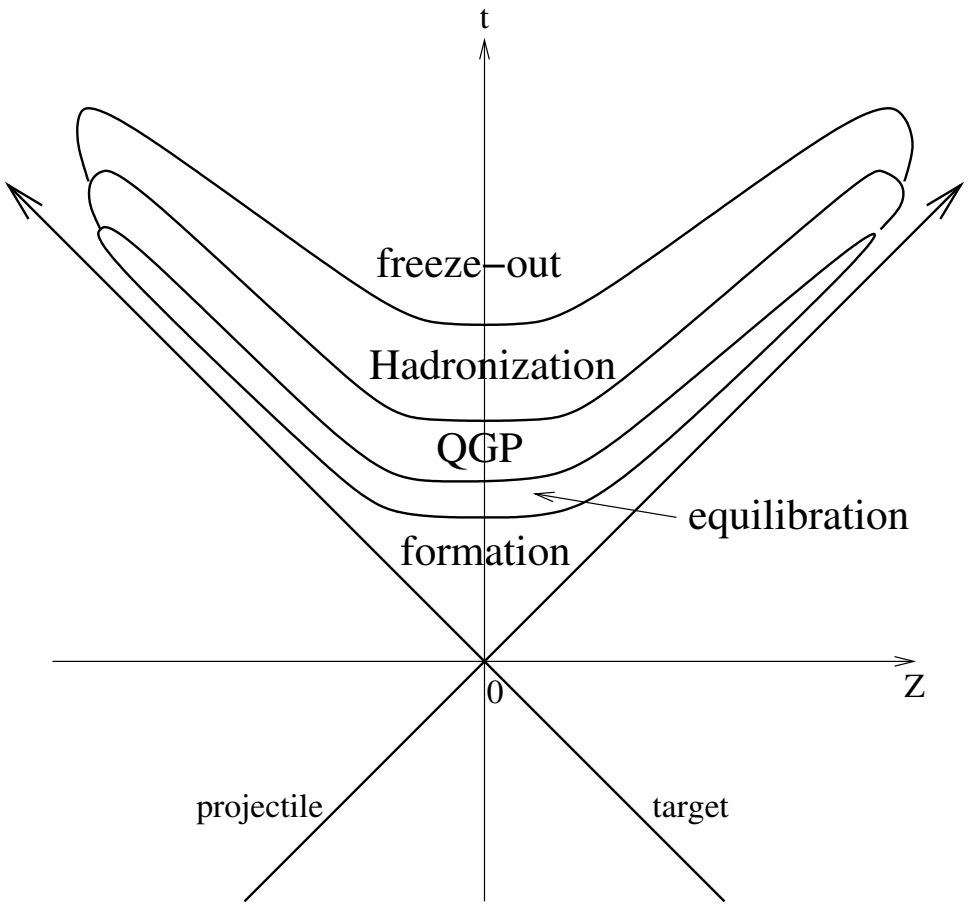

Figure 2.1: Space - time picture of quark gluon plasma formation

the energy density is written as

$$\varepsilon = P_0 \frac{\Delta N}{\mathcal{A}\Delta z} \tag{2.26}$$

$$= m_T \cosh y \left. \frac{1}{\mathcal{A}} \frac{dN}{dy} \frac{dy}{dz} \right|_{y=0} \quad . \tag{2.27}$$

However, from the relationships between z and t with τ , the rapidity can be written as

$$y = \frac{1}{2} \ln \frac{t+z}{t-z} \quad . \tag{2.28}$$

Using this relationship, the energy density is written as

$$\varepsilon = m_T \cosh y \left. \frac{1}{\mathcal{A}} \frac{dN}{dy} \frac{1}{\tau \cosh y} \right|_{y=0} \tag{2.29}$$

$$= \left. \frac{m_T}{\tau \mathcal{A}} \frac{dN}{dy} \right|_{y=0} \quad . \tag{2.30}$$

The estimated value of the proper time is about 1 fm/c and the value of $\mathcal{A}$ can be calculated as $\mathcal{A} = \pi 1.2^2 A^{2/3}$ (fm^2). Therefore, a measurement of $dN/dy|_{y=0}$ can be used to deduce the initial energy density. Also, since there are almost equal numbers of positive, negative and neutral particles that are created in a collision, the energy density can be expressed in terms of the charged particle-densities as

$$\varepsilon \approx \left. \frac{m_T}{\tau \mathcal{A}} \frac{3}{2} \frac{dN_{ch}}{d\eta} \right|_{\eta=0} \quad . \tag{2.31}$$

Here, it is assumed that $dN_{ch}/dy|_{y=0}$ is equal to $dN_{ch}/d\eta|_{\eta=0}$. However, as discussed in Section 2.1, there can be a 20% difference between the two, depending on the momenta and types of particles emitted in a collision.

2.3 MIT Bag Model

2.3.1 Introduction

Since at present it is not possible to solve the general problem of nonperturbative QCD, it is useful to study the nonperturbative quark-gluon system using some phenomenological models.

The MIT Bag Model is one such model and attempts a description of quark confinement. Figure 2.2 illustrates the basic idea of this model.

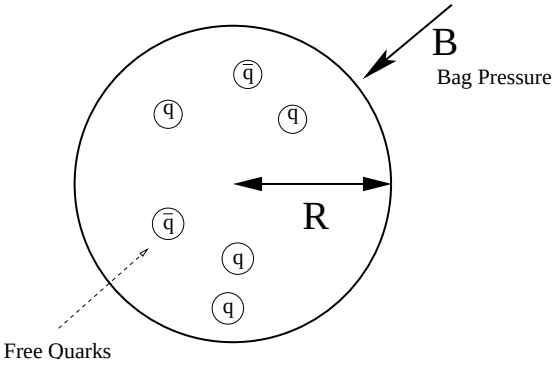

Figure 2.2: Bag Model

In this model, quarks are treated as free massless fermions inside a bag of finite dimension. The bag, which confines quarks inside, is in balance with the outward pressure arising from kinetic energy of quarks and inward directed, phenomenological bag pressure. An estimate of the bag pressure B is developed in the next section.

2.3.2 Determination of Bag Pressure

Since quarks are free fermions inside the bag, we can start with the Dirac Equation.

$$-i\hbar\frac{\partial\Psi}{\partial t} = \left(c\hat{\alpha}\cdot\hat{p} + m_0c^2\hat{\beta}\right)\Psi \quad , \tag{2.32}$$

where

$$\hat{\alpha}_i = \begin{pmatrix} 0 & \hat{\sigma}_i \\ \hat{\sigma}_i & 0 \end{pmatrix}, \tag{2.33}$$

$$\hat{\beta} = \begin{pmatrix} \mathbb{1} & 0 \\ 0 & -\mathbb{1} \end{pmatrix}, \tag{2.34}$$

$$\hat{\sigma}_1 = \begin{pmatrix} 0 & 1 \\ 1 & 0 \end{pmatrix}, \quad \hat{\sigma}_2 = \begin{pmatrix} 0 & -i \\ i & 0 \end{pmatrix}, \quad \hat{\sigma}_3 = \begin{pmatrix} 1 & 0 \\ 0 & -1 \end{pmatrix}, \tag{2.35}$$

and

$$\hat{p} = -i\hbar\nabla \quad . \tag{2.36}$$

Taking quarks inside the bag to be massless , Equation 2.32 is further simplified to

$$-i\hbar\frac{\partial\Psi}{\partial t} = c\hat{\alpha}\cdot\hat{p}\Psi \quad . \tag{2.37}$$

Now, if we look for stationary states using the ansatz

$$\Psi(\mathbf{x},t) = \psi(\mathbf{x})e^{-\frac{i}{\hbar}\varepsilon t} \quad , \tag{2.38}$$

one finds

$$\varepsilon\psi(\mathbf{x}) = c\hat{\alpha}\cdot\hat{p}\psi(\mathbf{x}) = \hat{H}_f\psi(\mathbf{x}) \quad . \tag{2.39}$$

Since Equation 2.39 is spherically symmetric, the angular momentum and parity operator commute with the Hamiltonian, $\hat{H}_f$. The eigenfunctions for this Hamiltonian are well-known spherical spinors:

$$\psi = \begin{pmatrix} \varphi_{jlm} \\ \chi_{jl'm} \end{pmatrix} \tag{2.40}$$

$$= \begin{pmatrix} ig\left(r\right)\Omega_{jlm}\left(\frac{\mathbf{r}}{r}\right) \\ -f\left(r\right)\Omega_{jl'm}\left(\frac{\mathbf{r}}{r}\right) \end{pmatrix} \tag{2.41}$$

where

$$\Omega_{jlm} = \sum_{m',m_s}\left(\left\langle l\frac{1}{2}j\,|m'm_sm\right\rangle Y_{lm'}\Lambda_{\frac{1}{2}m_s}\right) \tag{2.42}$$

and $\Lambda_{\frac{1}{2}m_s}$ are eigenfunctions of the spin operators:

$$\Lambda_{\frac{1}{2}\frac{1}{2}} = \begin{pmatrix} 1 \\ 0 \end{pmatrix}, \ \Lambda_{\frac{1}{2}-\frac{1}{2}} = \begin{pmatrix} 0 \\ 1 \end{pmatrix} \quad . \tag{2.43}$$

Also, because of Equation 2.42, either $j = l + \frac{1}{2}$, or $j = l - \frac{1}{2}$.

$$l' = 2j - l = \begin{cases} 2\left(l+\frac{1}{2}\right) - l = l+1 & for \quad j = l+\frac{1}{2} \\ 2\left(l-\frac{1}{2}\right) - l = l-1 & for \quad j = l-\frac{1}{2} \end{cases} \tag{2.44}$$

Now, using the above spherical spinors, Equation 2.39 becomes

$$\begin{aligned}
\varepsilon\psi &= c\hat{\alpha}\cdot\hat{p}\psi && (2.45)\\
&= c\begin{pmatrix} 0 & \hat{\sigma} \\ \hat{\sigma} & 0 \end{pmatrix}\cdot\hat{p}\begin{pmatrix} ig\left(r\right)\Omega_{jlm}\left(\frac{\mathbf{r}}{r}\right) \\ -f\left(r\right)\Omega_{jl'm}\left(\frac{\mathbf{r}}{r}\right) \end{pmatrix} && (2.46)\\
&= c\begin{pmatrix} \hat{\sigma}\cdot\hat{p}\left(-f\left(r\right)\Omega_{jl'm}\left(\frac{\mathbf{r}}{r}\right)\right) \\ \hat{\sigma}\cdot\hat{p}\left(ig\left(r\right)\Omega_{jlm}\left(\frac{\mathbf{r}}{r}\right)\right) \end{pmatrix} && (2.47)\\
&= c\begin{pmatrix} \left\{\hat{\sigma}\cdot\hat{p}\left(-f\left(r\right)\right)\right\}\Omega_{jl'm}\left(\frac{\mathbf{r}}{r}\right)+\left(-f\left(r\right)\right)\hat{\sigma}\cdot\hat{p}\Omega_{jl'm}\left(\frac{\mathbf{r}}{r}\right) \\ \left\{\hat{\sigma}\cdot\hat{p}\left(ig\left(r\right)\right)\right\}\Omega_{jlm}\left(\frac{\mathbf{r}}{r}\right)+ig\left(r\right)\hat{\sigma}\cdot\hat{p}\Omega_{jlm}\left(\frac{\mathbf{r}}{r}\right) \end{pmatrix} && (2.48)\\
&= c\begin{pmatrix} i\hbar\frac{df(r)}{dr}\left(\hat{\sigma}\cdot\frac{\mathbf{r}}{r}\right)\Omega_{jl'm}\left(\frac{\mathbf{r}}{r}\right)-f\left(r\right)\hat{\sigma}\cdot\hat{p}\Omega_{jl'm}\left(\frac{\mathbf{r}}{r}\right) \\ \hbar\frac{dg(r)}{dr}\left(\hat{\sigma}\cdot\frac{\mathbf{r}}{r}\right)\Omega_{jlm}\left(\frac{\mathbf{r}}{r}\right)+ig\left(r\right)\hat{\sigma}\cdot\hat{p}\Omega_{jlm}\left(\frac{\mathbf{r}}{r}\right) \end{pmatrix} \quad . && (2.49)
\end{aligned}$$

To expand this equation further, one uses the following useful property:

$$-i\hat{\sigma}\cdot\nabla = -i\hat{\sigma}\cdot\hat{r}\frac{\partial}{\partial r}+i\hat{\sigma}\cdot\hat{r}\frac{\hat{\sigma}\cdot\mathbf{L}}{\hbar r} \quad . \tag{2.50}$$

The proof of this property is shown in Appendix A. Then, Equation 2.49 becomes

$$\begin{aligned}
\varepsilon\psi &= c\begin{pmatrix} i\hbar\frac{df(r)}{dr}\left(\hat{\sigma}\cdot\frac{\mathbf{r}}{r}\right)\Omega_{jl'm}\left(\frac{\mathbf{r}}{r}\right)-f\left(r\right)\hat{\sigma}\cdot\left(-i\hbar\nabla\right)\Omega_{jl'm}\left(\frac{\mathbf{r}}{r}\right) \\ \hbar\frac{dg(r)}{dr}\left(\hat{\sigma}\cdot\frac{\mathbf{r}}{r}\right)\Omega_{jlm}\left(\frac{\mathbf{r}}{r}\right)+ig\left(r\right)\hat{\sigma}\cdot\left(-i\hbar\nabla\right)\Omega_{jlm}\left(\frac{\mathbf{r}}{r}\right) \end{pmatrix} && (2.51)\\
&= c\begin{pmatrix} i\hbar\frac{df(r)}{dr}\left(\hat{\sigma}\cdot\frac{\mathbf{r}}{r}\right)\Omega_{jl'm}\left(\frac{\mathbf{r}}{r}\right)-\hbar f\left(r\right)\left(-i\hat{\sigma}\cdot\hat{r}\frac{\partial}{\partial r}+i\hat{\sigma}\cdot\hat{r}\frac{\hat{\sigma}\cdot\mathbf{L}}{\hbar r}\right)\Omega_{jl'm}\left(\frac{\mathbf{r}}{r}\right) \\ \hbar\frac{dg(r)}{dr}\left(\hat{\sigma}\cdot\frac{\mathbf{r}}{r}\right)\Omega_{jlm}\left(\frac{\mathbf{r}}{r}\right)+i\hbar g\left(r\right)\left(-i\hat{\sigma}\cdot\hat{r}\frac{\partial}{\partial r}+i\hat{\sigma}\cdot\hat{r}\frac{\hat{\sigma}\cdot\mathbf{L}}{\hbar r}\right)\Omega_{jlm}\left(\frac{\mathbf{r}}{r}\right) \end{pmatrix} . && (2.52)
\end{aligned}$$

At this point, it is very convenient to introduce a new quantum number κ:

$$\kappa = \mp\left(j+\frac{1}{2}\right) = \begin{cases} -\left(l+1\right) & for \quad j=l+\frac{1}{2} \\ l & for \quad j=l-\frac{1}{2} \end{cases} \quad . \tag{2.53}$$

Using κ, redefine the angular function

$$\Upsilon_{\kappa m}\equiv\Omega_{jlm} \quad and \quad \Upsilon_{-\kappa m}\equiv\Omega_{jl'm} \quad . \tag{2.54}$$

Therefore,

$$\varepsilon\psi = c\begin{pmatrix} i\hbar\frac{df(r)}{dr}\left(\hat{\sigma}\cdot\frac{\mathbf{r}}{r}\right)\Upsilon_{-\kappa m} - \hbar f(r)\left(-i\hat{\sigma}\cdot\hat{r}\frac{\partial}{\partial r} + i\hat{\sigma}\cdot\hat{r}\frac{\hat{\sigma}\cdot\mathbf{L}}{\hbar r}\right)\Upsilon_{-\kappa m} \\ \hbar\frac{dg(r)}{dr}\left(\hat{\sigma}\cdot\frac{\mathbf{r}}{r}\right)\Upsilon_{\kappa m} + i\hbar g(r)\left(-i\hat{\sigma}\cdot\hat{r}\frac{\partial}{\partial r} + i\hat{\sigma}\cdot\hat{r}\frac{\hat{\sigma}\cdot\mathbf{L}}{\hbar r}\right)\Upsilon_{\kappa m} \end{pmatrix} \quad . \tag{2.55}$$

Now, using the following properties of Υ_{km} (see Appendix A),

$$\hbar\mathbf{L}\cdot\hat{\sigma}\Upsilon_{\kappa m} = (-\kappa-1)\hbar\Upsilon_{\kappa m} \tag{2.56}$$

$$\hbar\mathbf{L}\cdot\hat{\sigma}\Upsilon_{-\kappa m} = (\kappa-1)\hbar\Upsilon_{-\kappa m} \tag{2.57}$$

together with

$$\hat{\sigma}\cdot\hat{r}\Upsilon_{\kappa m} = -\Upsilon_{-\kappa m} \tag{2.58}$$

one finds

$$\varepsilon\psi = c\begin{pmatrix} i\hbar\frac{df(r)}{dr}(-1)\Upsilon_{\kappa m} - \hbar f(r)\left\{i\hat{\sigma}\cdot\hat{r}\left(\frac{\kappa-1}{r}\right)\Upsilon_{-\kappa m}\right\} \\ \hbar\frac{dg(r)}{dr}(-1)\Upsilon_{-\kappa m} + i\hbar g(r)\left\{i\hat{\sigma}\cdot\hat{r}\left(\frac{-\kappa-1}{r}\right)\Upsilon_{\kappa m}\right\} \end{pmatrix} \tag{2.59}$$

$$= c\begin{pmatrix} i\hbar\frac{df(r)}{dr}(-1)\Upsilon_{\kappa m} + i\hbar f(r)\left(\frac{\kappa-1}{r}\right)\Upsilon_{\kappa m} \\ \hbar\frac{dg(r)}{dr}(-1)\Upsilon_{-\kappa m} - \hbar g(r)\left(\frac{\kappa+1}{r}\right)\Upsilon_{-\kappa m} \end{pmatrix} \quad . \tag{2.60}$$

Therefore, the angular functions can be eliminated to give two coupled differential equations:

$$\varepsilon g(r) = -\hbar c\frac{df(r)}{dr} + (\kappa-1)\hbar c\frac{f(r)}{r} \tag{2.61}$$

$$-\varepsilon f(r) = -\hbar c\frac{dg(r)}{dr} - (\kappa+1)\hbar c\frac{g(r)}{r} \quad . \tag{2.62}$$

Substituting in $z = \frac{\varepsilon r}{\hbar c}$ gives

$$g = -\frac{df}{dz} + (\kappa-1)\frac{f}{z} \tag{2.63}$$

$$f = \frac{dg}{dz} + (\kappa+1)\frac{g}{z} \quad . \tag{2.64}$$

Solving for the function $g(z)$ gives

$$z^2\frac{d^2g}{dz^2} + 2z\frac{dg}{dz} + \left[z^2 - \kappa(\kappa+1)\right]g = 0 \quad . \tag{2.65}$$

The solution to this differential equation is known to be a spherical Bessel function [33, 34], and since the function must be regular at z=0, the solution must be the spherical Bessel function of the first kind:

$$j_n(z) = \frac{z^n}{1 \cdot 3 \cdot 5 \ldots (2n+1)} \left\{ 1 - \frac{\frac{1}{2}z^2}{1!\,(2n+3)} + \frac{\left(\frac{1}{2}z^2\right)}{2!\,(2n+3)\,(2n+5)} - \ldots \right\} \quad . \tag{2.66}$$

Therefore, for $\kappa > 0$, $n = \kappa$, and then

$$g(r) = j_\kappa \left(\frac{\varepsilon r}{\hbar c} \right) \quad . \tag{2.67}$$

For f, using the recursion relation of j_n,

$$\frac{n+1}{z} j_n + j_n' = j_{n-1} \tag{2.68}$$

and Equation 2.64, one finds

$$\begin{aligned} f &= j_\kappa' + (\kappa+1)\frac{j_\kappa}{z} && (2.69)\\ &= \left\{ j_{\kappa-1} - \frac{\kappa+1}{z} j_\kappa \right\} + (\kappa+1)\frac{j_\kappa}{z} && (2.70)\\ &= j_{\kappa-1} \quad . && (2.71) \end{aligned}$$

For $\kappa < 0$, $n = -(\kappa+1)$, and then

$$g(r) = j_{-(\kappa+1)} \left(\frac{\varepsilon r}{\hbar c} \right) \quad . \tag{2.72}$$

For f, using recurrence relation of j_n,

$$\frac{n}{z} j_n - j_n' = j_{n+1} \tag{2.73}$$

and Equation 2.64, it follows that

$$f = j'_{-(\kappa+1)} + (\kappa+1)\frac{j_{-(\kappa+1)}}{z} \tag{2.74}$$

$$= \left\{\frac{-(\kappa+1)}{z} j_{-(\kappa+1)} - j_{-\kappa}\right\} + (\kappa+1)\frac{j_{-(\kappa+1)}}{z} \tag{2.75}$$

$$= -j_{-\kappa} \quad . \tag{2.76}$$

Therefore, the stationary-state wave function can be written as

$$\psi = \begin{cases} N \begin{pmatrix} i j_\kappa(z) \\ \hat{\sigma}\cdot\hat{r} j_{\kappa-1}(z) \end{pmatrix} \Upsilon_{\kappa m} & for \quad \kappa > 0 \\ N \begin{pmatrix} i j_{-(\kappa+1)}(z) \\ -\hat{\sigma}\cdot\hat{r} j_{-\kappa}(z) \end{pmatrix} \Upsilon_{\kappa m} & for \quad \kappa < 0 \end{cases} \quad . \tag{2.77}$$

The boundary condition for the bag model is that no current flows across the surface of the bag. The current density using the Dirac equation is (see Appendix B)

$$j_i = c\bar{\psi}\gamma_i\psi \quad . \tag{2.78}$$

Here, $\gamma_i = \hat{\beta}\hat{\alpha}_i$. If n_μ is the outward normal vector to the surface of the bag, this boundary condition implies that at the surface of the boundary

$$n^\mu \bar{\psi}\gamma_\mu\psi = 0 \quad . \tag{2.79}$$

This condition would be satisfied if

$$-i\gamma_\mu n^\mu \psi = \psi \tag{2.80}$$

since then,

$$i\bar{\psi}\gamma_\mu n^\mu = \bar{\psi} \tag{2.81}$$

and

$$\bar{\psi}\psi = \left(i\bar{\psi}\gamma_\mu n^\mu\right)\psi = \bar{\psi}\left(i\gamma_\mu n^\mu \psi\right) = -\bar{\psi}\psi \tag{2.82}$$

thus requiring that $\bar{\psi}\psi = 0$. Hence, Equation 2.79 is satisfied.

Considering the bag as a simple sphere with radius R_0 in its lowest energy state ($\kappa = -1$ from Equation 2.77), this boundary conditions can be satisfied if

$$\left\{ j_0 \left(\frac{\varepsilon R_0}{\hbar c} \right) \right\}^2 = \left\{ j_1 \left(\frac{\varepsilon R_0}{\hbar c} \right) \right\}^2 \quad . \tag{2.83}$$

For the lowest mode, the solution is

$$\frac{\varepsilon R_0}{\hbar c} \cong 2.04 \quad . \tag{2.84}$$

Therefore, for the system of N quarks inside the bag with the bag pressure B, the total energy E is written as

$$E = \frac{2.04 \hbar c N}{R_0} + \frac{4\pi R_0^3}{3} B \quad . \tag{2.85}$$

For this bag to be at equilibrium, $\partial E / \partial R_0 = 0$. Hence,

$$\frac{\partial E}{\partial R_0} = -\frac{2.04 \hbar c N}{R_0^2} + 4\pi B R_0^2 = 0 \quad , \tag{2.86}$$

$$B = \frac{2.04 \hbar c N}{4\pi R_0^4} \quad , \text{ and} \tag{2.87}$$

$$B^{\frac{1}{4}} = \left(\frac{2.04 \hbar c N}{4\pi} \right) \frac{1}{R_0} \quad . \tag{2.88}$$

If the bag contains 3 quarks and has a radius of 0.8 fm, the bag pressure in natural units is

$$B^{1/4} = 206 \, MeV / \left(\hbar c \right)^{3/4} \tag{2.89}$$

This value is consistent with the suggested range of the bag pressure of between 145 MeV and 235 MeV.

2.3.3 Temperature and Density of Quark Gluon Plasma

Using a simple statistical technique shown in Appendix C, the pressure of the quark gluon plasma can be written as

$$p_{QGP} = p_{quark} + p_{gluon} \tag{2.90}$$

$$= \frac{g_{quark}}{\hbar^3 c^3} \frac{(kT)^4}{3} \left[\frac{7\pi^2}{120} + \left(\frac{\mu}{kT}\right) \frac{1}{4} + \frac{1}{8\pi^2} \left(\frac{\mu}{kT}\right)^4 \right] + \frac{g_{gluon}}{\hbar^3 c^3} (kT)^4 \frac{\pi^2}{90} \quad , \tag{2.91}$$

where

$$\begin{aligned} p_{quark} &\equiv \text{pressure from quarks} \quad , \\ p_{gluon} &\equiv \text{pressure from gluons} \quad , \\ \mu &\equiv \text{chemical potential of QGP} \quad , \\ T &\equiv \text{temparature of QGP} \quad , \text{ and} \\ k &\equiv \text{Boltzman constant} \quad . \end{aligned}$$

Here, g_{quark} and g_{gluon} are the degeneracy factors for quarks and gluons, respectively. For quarks, we have 2 spin orientations, 3 colors and 2 flavors (up and down, primarily). For gluons, we have 8 colors and 2 spin orientations. Therefore,

$$g_{quark} = 2 * 3 * 2 = 12 \quad , \text{ and} \tag{2.92}$$

$$g_{gluon} = 8 * 2 = 16 \quad . \tag{2.93}$$

Then, the pressure of the QGP is given as

$$p_{QGP} = \frac{1}{\hbar^3 c^3} \left[\frac{37\pi^2}{90} (kT)^4 + \mu (kT)^3 + \frac{\mu^4}{2\pi^2} \right] \quad . \tag{2.94}$$

Using the Bag Model pressure, $B^{1/4} = 206\, Mev/(\hbar c)^{3/4}$ from the previous section, Equation 2.94 can be solved for μ and T . Figure 2.3 shows the resulting dependence of the temperature on the chemical potential. In the extreme case of $\mu = 0$, which is of principal interest for RHIC, a temperature of about 145 MeV is reached for the generated quark-gluon plasma. At the other extreme, where $T = 0$, a chemical potential of about 434 MeV is reached by forming

the QGP. This can be compared with normal nuclear matter where the chemical potential and temperature are about 250 MeV and 0 MeV, respectively.

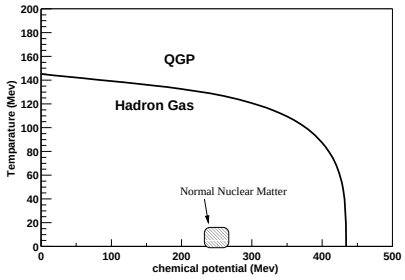

Figure 2.3: Phase Diagram of QGP

From the same technique used to obtain Equation 2.94, it is also possible to estimate the net baryon density of the QGP using the statistical model. From Appendix C, the net baryon density is given by

$$n_{net-baryon} = \frac{1}{3}\frac{N_{net-fermion}}{V} \tag{2.95}$$

$$= \frac{1}{3} g_{quark} \frac{1}{\hbar^3 c^3} \left[\frac{1}{6} \mu \left(kT \right)^2 + \frac{1}{6\pi^2} \mu^3 \right] \tag{2.96}$$

Here, $N_{net-fermion}$ is the number of fermions in the QGP, and V is the volume of the QGP. For $\mu = 434\, MeV$ and $T = 0\, MeV$, Equation 2.96 gives $n_{net-baryon} = 0.72\, /fm^3$. Normal nuclear matter has a baryon density of about $0.14\, /fm^3$, so at low temperature, the QGP is created at about 5 times normal nuclear matter density.

2.4 Wounded Nucleon Model

The key for producing quark-gluon matter is to have a large number of collisions involved in the nucleus-nucleus events. As one nucleon of a nucleus passes through the other nucleus, it suffers several inelastic collisions, with each collision associated with a large energy loss. With the involvement of many nucleons, a sufficient energy density at midrapidity may be created to produce a QGP after the remnants of the two colliding nuclei leave the interaction region. At present, the QCD theory is unable to describe the scenario with sufficient precision to give experimentally verifiable results. Consequently, only phenomenological theories have

been developed. The "Wounded Nucleon" model [35, 32] is one of the more simple models and describes a nucleus-nucleus collision as a collection of many nucleon-nucleon collisions, ignoring collective effects. The basic assumption is that the inelastic collision of two nuclei can be described as a sum of many incoherent collisions of the constituent nucleons. The cross section of nucleon-nucleon collisions is assumed to remain constant though the entire process of the nucleus-nucleus collision.

Figure 2.4 illustrates a nucleus-nucleus collision with an impact parameter **b**. Define

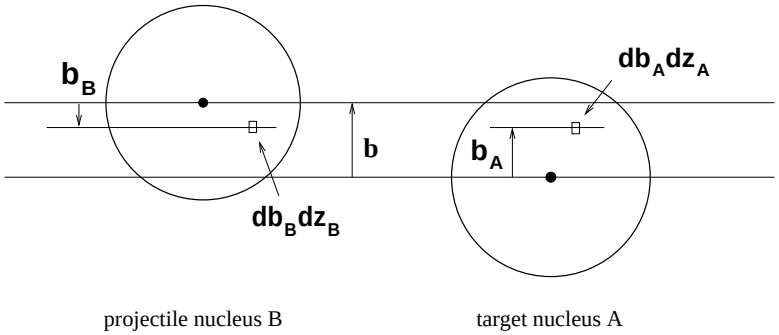

Figure 2.4: A projectile nucleus B is colliding with the target nucleus B with an impact parameter **b**.

$t\left(\mathbf{b}_{nucleon}\right) d\mathbf{b}_{nucleon}$ as the probability for having a nucleon-nucleon collision within the transverse area element $d\mathbf{b}_{nucleon}$ when one nucleon is located at the impact parameter of $\mathbf{b}_{nucleon}$ relative to other nucleon. (Note, $\mathbf{b}_{nucleon}$ is a two-dimensional vector.) Here, $t\left(\mathbf{b}_{nucleon}\right)$ is known as the nucleon-nucleon thickness function. It is normalized as

$$\int t\left(\mathbf{b}_{nucleon}\right) d\mathbf{b}_{nucleon} = 1 \quad . \tag{2.97}$$

Since we assume the nucleon-nucleon cross section σ_{in} to be constant, $t\left(\mathbf{b}_{nucleon}\right)\sigma_{in}$ is the probability of a nucleon-nucleon inelastic collision at the impact parameter $\mathbf{b}_{nucleon}$. The probability of finding a nucleon in a volume element $d\mathbf{b}dz$ of a nucleus is defined as $\rho(\mathbf{b}, z)d\mathbf{b}dz$. Therefore, the probability of having a nucleon-nucleon collision when nucleus B collides with nucleus A with the impact parameter **b** can be written as

$$P\left(\mathbf{b}\right) = \int \rho_A\left(\mathbf{b}_A, z_A\right) d\mathbf{b}_A dz_A \; \rho_b\left(\mathbf{b}_B, z_B\right) d\mathbf{b}_B dz_B \; t\left(\mathbf{b} - \mathbf{b}_A - \mathbf{b}_B\right)\sigma_{in} \tag{2.98}$$

$$\equiv T\left(\mathbf{b}\right)\sigma_{in} \quad , \tag{2.99}$$

where $T(\mathbf{b})$ is the nucleus-nucleus thickness function, and defined as

$$T(\mathbf{b}) = \int \rho_A(\mathbf{b}_A, z_A)\, d\mathbf{b}_A dz_A\, \rho_b(\mathbf{b}_B, z_B)\, d\mathbf{b}_B dz_B\, t(\mathbf{b} - \mathbf{b}_A - \mathbf{b}_B) \quad . \tag{2.100}$$

Therefore, the probability for having exactly n nucleon-nucleon collisions at the impact parameter $\mathbf{b}$ can be written as

$$P(n, \mathbf{b}) = \left(\begin{array}{c} AB \\ n \end{array} \right) [T(\mathbf{b})\, \sigma_{in}]^n [1 - T(\mathbf{b})\, \sigma_{in}]^{AB-n} \quad . \tag{2.101}$$

Here, A and B are the number of nucleons in nucleus A and B. With this, it is a simple matter to find the total probability of inelastic collisions with impact parameter $\mathbf{b}$:

$$\frac{d\sigma_{in}^{AB}}{d\mathbf{b}} = \sum_{n=1}^{AB} P(n, \mathbf{b}) = 1 - [1 - T(\mathbf{b})\, \sigma_{in}]^{AB} \quad . \tag{2.102}$$

The total inelastic cross section σ_{in}^{AB} is then given by

$$\sigma_{in}^{AB} = \int d\mathbf{b} \left\{ 1 - [1 - T(b)\, \sigma_{in}]^{AB} \right\} \quad . \tag{2.103}$$

The average number of nucleon-nucleon collisions at the impact parameter $\mathbf{b}$ can be found as

$$\begin{aligned}
\langle n(\mathbf{b}) \rangle &= \sum_{n=1}^{AB} nP(n, \mathbf{b}) && (2.104)\\
&= \sum_{n=0}^{AB} n \left(\begin{array}{c} AB \\ n \end{array} \right) [T(\mathbf{b})\, \sigma_{in}]^n [1 - T(\mathbf{b})\, \sigma_{in}]^{AB-n} && (2.105)\\
&= \left[x \frac{\partial}{\partial x} \sum_{n=0}^{AB} \left(\begin{array}{c} AB \\ n \end{array} \right) [x\sigma_{in}]^n [1 - T(\mathbf{b})\, \sigma_{in}]^{AB-n} \right]_{x=T(\mathbf{b})} && (2.106)\\
&= \left[x \frac{\partial}{\partial x} \{1 - T(\mathbf{b})\, \sigma_{in} + x\sigma_{in}\}^{AB} \right]_{x=T(\mathbf{b})} && (2.107)\\
&= \left[xAB\sigma_{in} \{1 - T(\mathbf{b})\, \sigma_{in} + x\sigma_{in}\}^{AB-1} \right]_{x=T(\mathbf{b})} && (2.108)\\
&= ABT(\mathbf{b})\, \sigma_{in} \quad . && (2.109)
\end{aligned}$$

This result needs to be modified to include the probability of having an inelastic collision. Then,

the average number is

$$\langle n'(\mathbf{b})\rangle = \frac{\langle n(\mathbf{b})\rangle}{1-[1-T(b)\,\sigma_{in}]^{AB}} \quad . \tag{2.110}$$

Averaging over the impact parameter $\mathbf{b}$ in this equation produces

$$\langle n'\rangle = \frac{\int \langle n'(\mathbf{b})\rangle \left\{d\sigma_{in}^{AB}/d\mathbf{b}\right\} d\mathbf{b}}{\int \left\{d\sigma_{in}^{AB}/d\mathbf{b}\right\} d\mathbf{b}} \tag{2.111}$$

$$= \frac{\int d\mathbf{b}\,\langle n'(\mathbf{b})\rangle \left\{1-[1-T(b)\,\sigma_{in}]^{AB}\right\}}{\int d\mathbf{b}\left\{1-[1-T(b)\,\sigma_{in}]^{AB}\right\}} \quad . \tag{2.112}$$

Equation 2.112 provides an average number of collisions in relativistic heavy-ion collisions. It has been suggested [35] that for these collisions, the average multiplicities M_{AB} can be expressed as

$$\langle M_{AB}\rangle = \frac{1}{2}\langle W\rangle \cdot \langle n'\rangle|_{A=1,B=1} \tag{2.113}$$

where $\langle W\rangle$ is average number of nucleons that undergo the inelastic collisions, or number of participants. Therefore, significant deviation from Equation 2.113 indicates a change in the dynamics of the particle production process.

2.5 Signals for Quark-Gluon Plasma

The previous discussion has shown that when two heavy-ions collide with sufficient energy, a QGP may be formed for a short period of time. Finding this elusive state of matter has been a very popular topic of research for the past two decades. Despite many experimental studies, definitive evidence for a QGP has yet to be developed. The difficulty arises from the fact that there is no known, clear and measurable signature for the creation of a QGP. It is generally felt that many aspects of relativistic heavy-ion collisions will have to be investigated to prove the existence of this state of matter. There are currently several theoretical hypotheses for possible signals indicating the formation of a QGP in relativistic heavy-ion collisions.

2.5.1 Enhancement of Strangeness

The third lightest quark, the strange quark s, and its anti-matter partner, $\bar{s}$, are absent in all stable forms of matter. In collisions of a proton with another proton or a proton with a heavy-

ion, only a small number of strange quarks are produced, and they subsequently form strange particles such as K^+ and K^- [36, 37, 38]. However, by scattering a heavy-ion with another heavy-ion, it has been observed that a large number of strange particles can be produced [37]. It is believed that an enhanced production of strange particles might result with the achievement of chemical and thermal equilibrium during the formation of a QGP. This enhancement of strange particles results from the greater phase space available for the formation of $s\bar{s}$ quarks as compared to that for $u\bar{u}$ or $d\bar{d}$ pairs. As $u\bar{u}$ and $d\bar{d}$ pairs are created, they start to fill energy states starting from the lowest energy, according to the Pauli exclusion principle. As they fill those states, they must have the Fermi energies associated with the energy of the states being filled. At some point, the required value of Fermi energy exceeds the threshold energy for creating two strange quarks. At this point, the production of $s\bar{s}$ becomes energetically favored.

The ratio of number of strange quarks to that of up and down quarks can be written as

$$\frac{s+\bar{s}}{u+\bar{u}+d+\bar{d}} = \frac{K^+/\pi^+}{1.5+K^+/\pi^+} \quad , \tag{2.114}$$

where the expression on the right-hand side is found in Reference [32]. In p-Be data at 14.6 GeV/c, the ratios of K^+/π^+ is reported as 0.078 [39]. This produces the strangeness ratio of about 5% by Equation 2.114. On the other hand, in the evolution of a QGP, it is believed that there exists a hadron-gas phase that is in chemical and thermodynamic equilibrium (shown in Figure 2.1). If the hadron gas is formed in a collision of heavy-ions, the ratio of K^+/π^+ can be written [32] as

$$\frac{K^+}{\pi^+} = \left(\frac{m_{K^+}}{m_{\pi^+}}\right)^2 \frac{K_2\left(m_{K^+}/T\right) + K_2\left(2m_{K^+}/T\right)/2 + K_2\left(3m_{K^+}/T\right)/3 + \cdots}{K_2\left(m_{\pi^+}/T\right) + K_2\left(2m_{\pi^+}/T\right)/2 + K_2\left(3m_{\pi^+}/T\right)/3 + \cdots} \tag{2.115}$$

where K_2 is the modified Bessel function of order 2. Using the estimated value for the temperature of 200MeV, Equation 2.115 gives a K^+/π^+ ratio of about 0.38, which yields 20% for the strangeness content. Therefore, the formation of a QGP should lead to a significant enhancement in strange-particle production.

Equation 2.115 was obtained with the assumption of having a chemically-equilibrated hadron gas. It is very questionable to assume that complete chemical and thermodynamic equilibrium will be achieved within the short expansion of a QGP. As a result, the ratio of K^+/π^+ alone

does not provide a definitive signature of QGP. In the end, it is also necessary to study the other strange particles like K^-, as well as non-strange particles such as π^-.

2.5.2 Suppression of Production of J/Ψ

The very simple Hamiltonian for a J/Ψ particle can be written [40, 32] as

$$H = \frac{\mathbf{p}^2}{2\mu} - \frac{\alpha}{r} + kr \quad , \tag{2.116}$$

where μ is the reduced mass of the charm-anti-charm quark system ($c\bar{c}$), and α is the coupling constant for a Coulomb-like force. In a quark-gluon plasma, the string tension, k, between c and $\bar{c}$ vanishes because of quark deconfinement. Therefore, the Coulomb-like force is the only force to bind the charm and anti-charm quarks together. However, in the deconfined plasma, the charm quark would be screened from the anti-charm quark by the abundant amount of light quarks, analogous to the Debye screening of electric charges. This results in an effective modification to the Coulomb-like potential of Equation 2.116 so as to behave as a Yukawa-type potential.

$$\begin{array}{ccc} \text{Coulomb type} & & \text{Yukawa type} \\ V(r) = \dfrac{q}{4\pi r} & \rightarrow & V(r) = \dfrac{q}{4\pi}\dfrac{\exp^{-r/\lambda}}{r} \end{array}$$

where λ is the Debye screening length. According to perturbative QCD (pQCD), the Debye screening length is inversely proportional to the the temperature of the plasma [41, 32]. In the lowest-order pQCD, it is written as

$$\lambda = \sqrt{\frac{2}{3g^2}}\frac{1}{T} \quad . \tag{2.117}$$

Therefore, the Hamiltonian for a J/Ψ particle in a QGP has the form

$$H = \frac{\mathbf{p}^2}{2\mu} - \frac{\alpha \exp^{-r/\lambda}}{r} \quad . \tag{2.118}$$

For the charm and anti-charm quarks to be bound together, it is necessary for the energy of the system described by Equation 2.118 to have a local minimum as a function of the radial separation. Using the uncertainty relation $r \cdot \langle \mathbf{p} \rangle \sim \hbar$, the energy of the system described by

Equation 2.118 can be expressed as

$$E = \frac{\hbar^2}{2\mu r^2} - \frac{\alpha \exp^{-r/\lambda}}{r} \quad . \tag{2.119}$$

This equation needs to have a local minimum at some finite value of r. By differentiating this equation,

$$\frac{dE}{dr} = -\frac{\hbar^2}{\mu r^3} + \frac{\alpha\,(1 + r/\lambda) \exp^{-r/\lambda}}{r^2} \tag{2.120}$$

and setting the result equal to zero, we obtain

$$\frac{r}{\lambda}\left(1 + \frac{r}{\lambda}\right) \exp^{-r/\lambda} = \frac{\hbar^2}{\alpha\mu\lambda} \quad . \tag{2.121}$$

Since the left hand side of Equation 2.121 is always larger than zero for a non-zero value of r, and since it has the maximum value of about 0.84 at $r/\lambda \approx 1.618$, the right hand side of this equation needs to be less than 0.84 to have a solution. In other words, the condition for forming a J/Ψ particle is

$$\frac{\hbar^2}{0.84\alpha\mu} < \lambda \quad . \tag{2.122}$$

If the Debye screening length is smaller than $\hbar^2/0.84\alpha\mu$, the $c\bar{c}$ system will not be bound. Using some reasonable values for α and μ, $\hbar^2/0.84\alpha\mu \approx 0.41$ fm. Since Equation 2.117 shows that λ is a decreasing function for increasing temperature, one finds that the $c\bar{c}$ will become unbound at some temperature. This leads to the prediction that the production of J/Ψ particles will be suppressed in the quark-gluon plasma [42].

Unfortunately, J/Ψ production can be also suppressed by other means. For example, while traveling from the inner core of the QGP, the J/Ψ particle might interact with other hadrons and produce a pair of charmed mesons by the reaction

$$J/\Psi + h \rightarrow D + \bar{D} + X \quad .$$

This reaction clearly reduces the observed yields of J/Ψ particles without the formation of the QGP. It is predicted that at low transverse momentum, J/Ψ particles will not survive passage through the surrounding medium. Furthermore, since J/Ψ particles can be created by the scattering of hadrons, it is not easy to directly relate an observed production of J/Ψ particles

to the formation of a QGP. However, at a high transverse momentum, it should be possible to more clearly translate any observed deficits of J/Ψ particles to the screening effect in the QGP.

2.5.3 Dileptons

In the QGP formed by a heavy-ion collision, quarks are not bound to their original nucleons. Hence, quarks are free to interact with each other. In particular, a quark can interact with an antiquark to form a virtual photon that subsequently decays to a lepton and an antilepton. Figure 2.5 shows the diagram for this process. Since leptons only interact with other particles

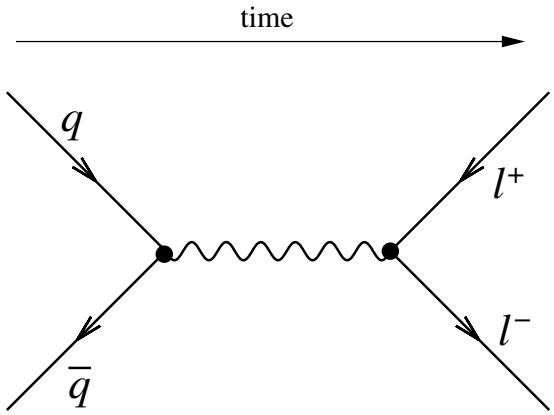

Figure 2.5: Diagram for $q + \bar{q} \rightarrow l^+ + l^-$

through the electromagnetic and weak forces, their mean free paths are believed to be fairly large. Therefore, after the formation of a lepton pair, the leptons are not likely to suffer subsequent collisions traveling through the QGP on their way to the detector. As a result, the production of lepton pairs can be used as a direct measure of the QGP.

With the assumption that quark and antiquark distribution functions are given by an $e^{-E/T}$ dependence, the production of a dilepton in the QGP [32] is given by

$$\frac{dN_{l^+l^-}}{dM^2dy} \sim \pi R_A^2 N_c N_s^2 \sum_{f=1}^{N_f} \left(\frac{e_f}{e}\right)^2 \frac{\sigma(M)}{2(2\pi)^4} \left(1 - \frac{4m_q^2}{M^2}\right)^{\frac{1}{2}} \frac{3\tau_0^2 T_0^6}{M^2} \left[H\left(\frac{M}{T_0}\right) - H\left(\frac{M}{T_c}\right)\right] \quad (2.123)$$

where

$$
\begin{aligned}
R_A &= \text{radius of nuclei} \\
N_c &= \text{number of colors} \\
N_s &= \text{number of flavors} \\
e_f &= \text{electric charge of a quark with flavor f} \\
M &= \text{invariant mass of the dilepton pair} \\
\sigma(M) &= \text{cross section of } q\bar{q} \rightarrow l^+l^- \\
&= \frac{4\pi}{3}\frac{\alpha^2}{M^2}\left(1-\frac{4m_q^2}{M^2}\right)^{-\frac{1}{2}}\sqrt{1-\frac{4m_l^2}{M^2}}\left(1+2\frac{m_q^2+m_l^2}{M^2}+4\frac{m_q^2 m_l^2}{M^4}\right) \quad (2.124) \\
H(z) &= z^2\left(8+z^2\right)K_0(z)+4z\left(4+z^2\right)K_1(z) \quad (2.125) \\
K_0 \text{ and } K_1 &= \text{modified Bessel Functions of order 0 and 1} \quad (2.126) \\
\tau_0 &= \text{proper time} \\
T_0 &= \text{initial temperature of QGP at proper time} \\
T_c &= \text{critical temperature from QGP to hadronization} \quad .
\end{aligned}
$$

By Equation 2.123, the measurement of dilepton productions can yield the thermodynamic properties of the QGP.

However, the dilepton signature is diluted since the above mechanism is not the only process to produce dileptons. Dilepton pairs can also be produced in the Drell Yan process. Figure 2.6 illustrates this process. A valence quark of one nucleon interacts with a sea antiquark of the other nucleon to produce a virtual photon which then decays to a lepton pair. The production of dileptons in nucleus-nucleus collisions [32] can be written as

$$
\left.\frac{dN_{l^+l^-}}{dMdy}\right| = \frac{3}{2\pi r_0}\frac{AB}{A^{2/3}+B^{2/3}}\exp^{-\frac{k^2}{2\beta^2}}\frac{d\sigma_{DY}^{NN}}{dMdy} \quad (2.127)
$$

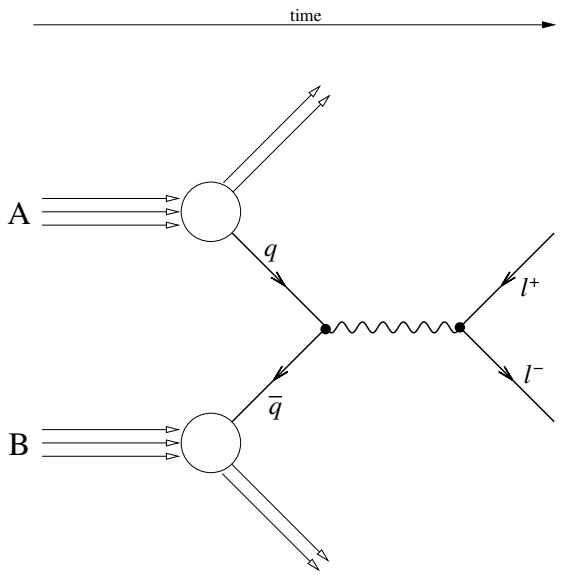

Figure 2.6: Diagram for Drell Yan

where

$$
\begin{aligned}
b &= \text{impact parameter} \quad , \\
A \text{ and } B &= \text{number of nucleons in nucleus A and B} \quad , \\
r_0 &= \text{radius of the nucleon} \quad , \\
\beta^2 &= \frac{r_0}{3}\left(A^{\frac{2}{3}} + B^{\frac{2}{3}}\right) + 0.68^2 \quad , \text{ and} \\
\frac{d\sigma_{DY}^{NN}}{dMdy} &= \text{cross section of the nucleon} - \text{nucleon Drell Yan process} \quad .
\end{aligned}
$$

The Drell Yan cross section of hadron-hadron collisions is well established through experiments. This Drell Yan contribution is a significant background process to thermal lepton production in the QGP. The precision with which thermal dilepton production can be deduced depends on how much of the lepton pair production is dominated by either one of the above processes.

There are other processes that can produce dileptons, such as pion annihilation ($\pi^+ + \pi^- \rightarrow l^+ + l^-$) shown in Figure 2.7 and decays of J/Ψ and other resonances. The lepton pair resulting from these processes also need to be separated from the thermal production of dileptons in the analysis of the QGP.

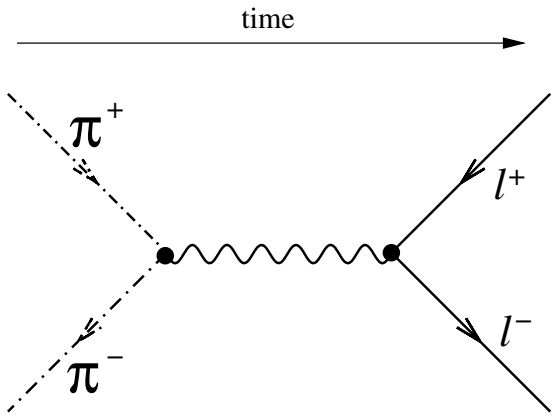

Figure 2.7: Diagram for $\pi^+ + \pi^- \rightarrow l^+ + l^-$

2.5.4 Direct Photon

A photon can only interact with other particles in the QGP through the electromagnetic force. With a fairly large value of its mean free path, it is expected that produced photons escape from the QGP without subsequent collisions after their creation. Therefore, it is believed that the production of photons provides another direct means to measure the properties of the QGP.

In the QGP, a quark and an anti-quark can annihilate to produce a photon and a gluon. Alternatively, either a quark or an anti-quark can interact with a gluon to produce a photon and a quark (or an anti-quark) through the Compton process. Figure 2.8 shows the diagrams for these processes. The production of photons through the annihilation and Compton processes can be written [32] as

$$E_\gamma \frac{dN_\gamma}{d^3\mathbf{p}_\gamma d^4x} = \frac{5}{9}\frac{\alpha_e \alpha_s}{2\pi^2} f_q\left(\mathbf{p}_\gamma\right) T^2 \ln\left\{\frac{3.7388 E_\gamma}{g^2 T}\right\} \tag{2.128}$$

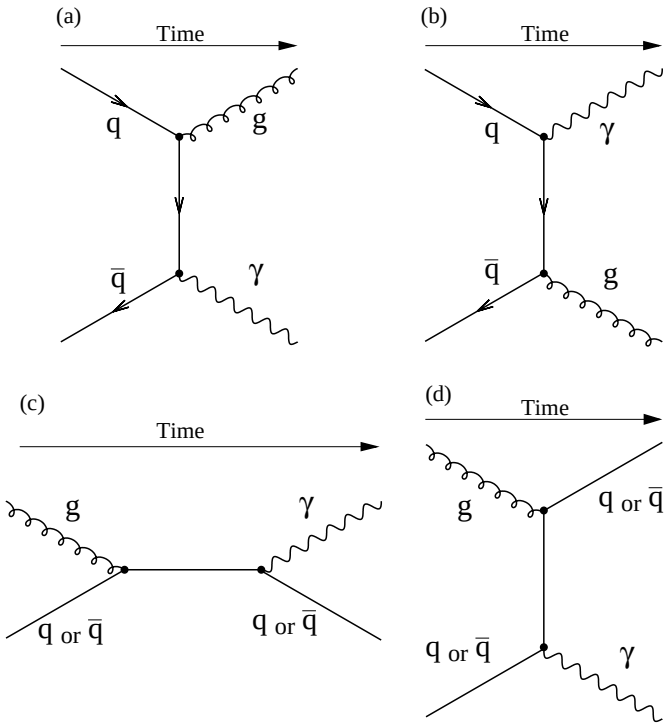

Figure 2.8: Diagram for Direct Photon Production
(a) and (b) show the annihilation process; (c) and (d) represent the Compton process.

where

$$
\begin{aligned}
\alpha_e &= \frac{e^2}{4\pi} \quad , \\
\alpha_s &= \frac{g^2}{4\pi} \quad , \\
f_q &\equiv \text{quark distribution function} \quad , \\
E_\gamma &\equiv \text{energy of the photon,} \\
N_\gamma &\equiv \text{number of the photon,} \\
\mathbf{p}_\gamma &\equiv \text{momentum of the photon} \quad , \text{ and} \\
x &\equiv \text{world vector} \quad .
\end{aligned}
$$

If the quark is thermalized in the plasma, the quark distribution function has the form of $\exp(-E/kT)$. Thus, the photon production can carry information on the thermal properties of the plasma.

The annihilation and Compton processes are not the only source of photons in the heavy-ion collision. A photon can be produced by the annihilation of pions

$$\pi^+ + \pi^- \rightarrow \gamma + \rho^0 \quad .$$

Also, a charged pion can interact with a π^0 to produce a photon and a charged ρ meson

$$\pi^\pm + \pi^0 \rightarrow \gamma + \rho^\pm \quad .$$

These are just some of the processes to produce photons in hadron collisions. The photon can be produced by parton collisions when a nucleon of a beam nucleus collides with a nucleon of a target nucleus. In an experiment, since the measured photon distribution includes contributions from these processes, the relative contribution of the different production mechanism must be identified in order to obtain the properties of the QGP.

2.5.5 HBT

HBT stands for Hanbury-Brown and Twiss. These scientists measured the angular diameter of a star using the correlation between photon pairs in 1956 [43]. In their experiment, it was

found that the intensity of a photon measured at one space-time point is related to an another photon measured at another space-time point. Furthermore, this relationship was correlated to the radial size of the star which was the source of the photons. Therefore, it was realized that the intensity measurement of two identical bosons could provide the radial size of the source of the emitted particles. In relativistic heavy-ion physics, this technique is being used to try and test for the existence of a QGP and to estimate the size of the hot-dense matter created by the heavy-ion collision. The choice for the type of particles to be measured depends on the production of those particles, but typically pions and/or other mesons are used because of their abundance.

In HBT analysis of heavy-ion collisions, the correlation function, C, to be studied is defined as [32]

$$C\left(k_1, k_2\right) = \frac{P\left(k_1, k_2\right)}{P\left(k_1\right) P\left(k_2\right)} \tag{2.129}$$

where $P\left(k_1, k_2\right)$ is defined as the probability of detecting a particle of momentum k_1 in coincidence with a second particle of momentum k_2, $P\left(k_1\right)$ and $P\left(k_2\right)$ are the probabilities of detecting particles of momentum k_1 and k_2, respectively. If the source is coherent such as the QGP, this function is equal to one. Whereas, if the source of the particles is chaotic, the correlation is related to the Fourier transform of the density of the source [32]. Therefore, the HBT measurement can provide the information of the source of the particles.

Typically, since the type of the source isn't known, the correlation function is parametrized as

$$C = 1 + \lambda \exp^{-R_x^2 q_x^2/2 - R_y^2 q_y^2/2 - R_z^2 q_z^2/2 - \sigma_t^2 q_t^2/2} \tag{2.130}$$

where λ and q_i are the chaoticity parameter and the four-momentum separation. As a result, the value of λ provides the level of cohesiveness of the particles source, and the values of R_x, R_y , R_z and σ_t provide the size of that source.

2.5.6 Other Signatures of QGP

There are a few more proposed signatures of QGP formation such as collective flow signals and particle fluctuations. The flow signal stems from the assumption that the QGP should behave as a fluid. Then, if the QGP achieves thermal and/or chemical equilibrium, the dynamics of the quark-gluon matter should be described by hydrodynamic equations. This results in

particle production greatest in the direction of the largest pressure gradient. As a result, there should be an asymmetric distribution of emitted particles. These asymmetries are known as flow signals. A fluctuation analysis comes from the fact that the dynamical fluctuation of some observables above the level of statistical fluctuations could provide characteristics of the quark-hadron phase transition [44, 45]. Because of the large production of particles from a single collision in relativistic heavy-ion collisions, the statistical analysis of the critical phenomena such as self-similarity and intermittency could be directly tested[46]. For example, fluctuations in the ratio of different types of particles are suggested to be a signature of the QGP [47]. To confirm the existence of this elusive matter, all of these suggested signatures need to be examined theoretically and tested experimentally.

Chapter 3

BRAHMS Experimental Setup

The BRAHMS experiment consists of three major sets of detectors: the global detectors, the midrapidity spectrometer, and the forward spectrometer. The overall layout of the experiment is shown in Figure 3.1. The global detectors provide the overall properties of a collision such as charged-particle multiplicity, reaction centrality and location of the vertex, etc. The midrapidity and forward spectrometers identify particles and determine their momentum in the angular ranges of 35°-90° and 2.5°-30°, respectively. Figure 3.2 shows the combined acceptance of the two spectrometers for identified pions, kaons and protons.

3.1 Global Detectors

The global detectors for the BRAHMS experiment consist of: the Multiplicity Array, the Beam-Beam Counter Arrays, and the Zero Degree Calorimeter.

3.1.1 Multiplicity Array

This detector, which is shown in Figure 3.3, provides a measure of the centrality of a collision by measuring the particle production in the pseudorapidity range of $|\eta| \leq 2.2$ for a collision at the center of the array. It is made of two different detector types with twenty-five silicon strip detectors and thirty-eight plastic scintillator "tile" detectors. As particles traverse the individual detector elements, they deposit an amount of energy according to the stopping power of the particle. By measuring the total amount of energy deposited, it is then possible to estimate the

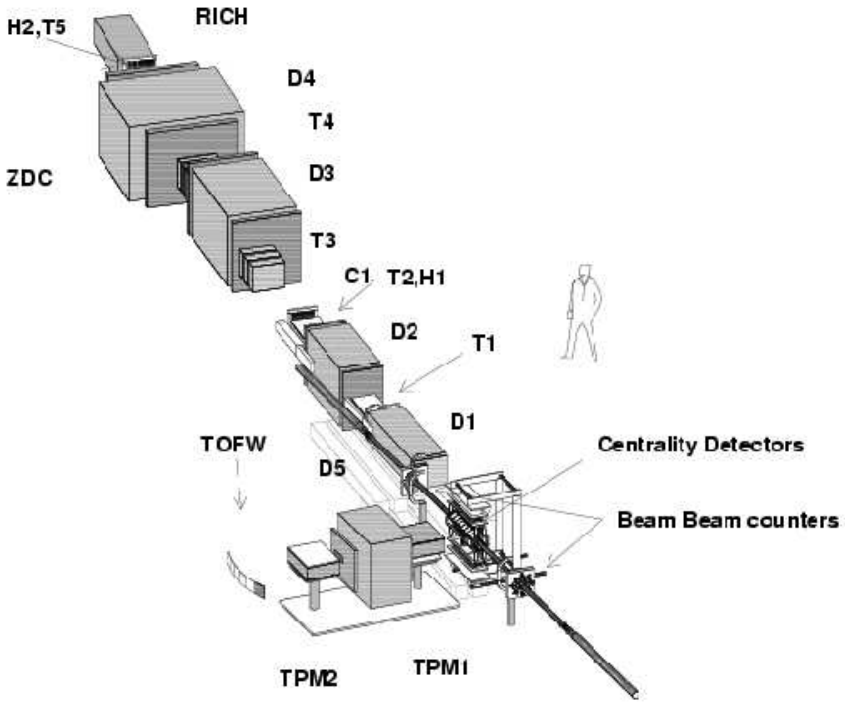

ZDC --- Zero Degree Calorimeter
RICH --- Ring Imaging Cherenkov Detector
D3, D4, D5 --- Drift Chamber
C1 --- Cherenkov Detector
D1, D2, D3, D4, D5 --- Dipole Magnets
T1, T2, TPM1 TPM2 --- Time Projection Chamber
H1, H2, TOFW --- Time-of-flight Detectors

Figure 3.1: BRAHMS Detectors

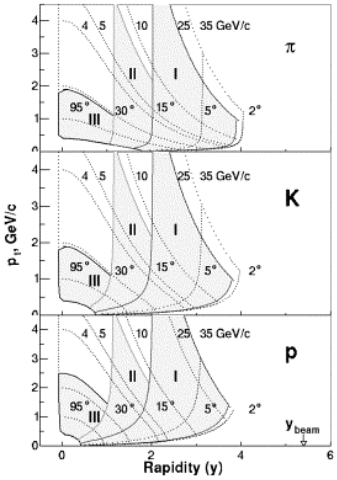

Figure 3.2: Combined Acceptance of Spectrometers
The region I, II and III represents the acceptances of the Back-Forward Spectrometer, Front-Forward Spectrometer and Midrapidity spectrometer, respectively. 2°, 5°, 15°, 30° and 90° stands for angles of the spectrometers.

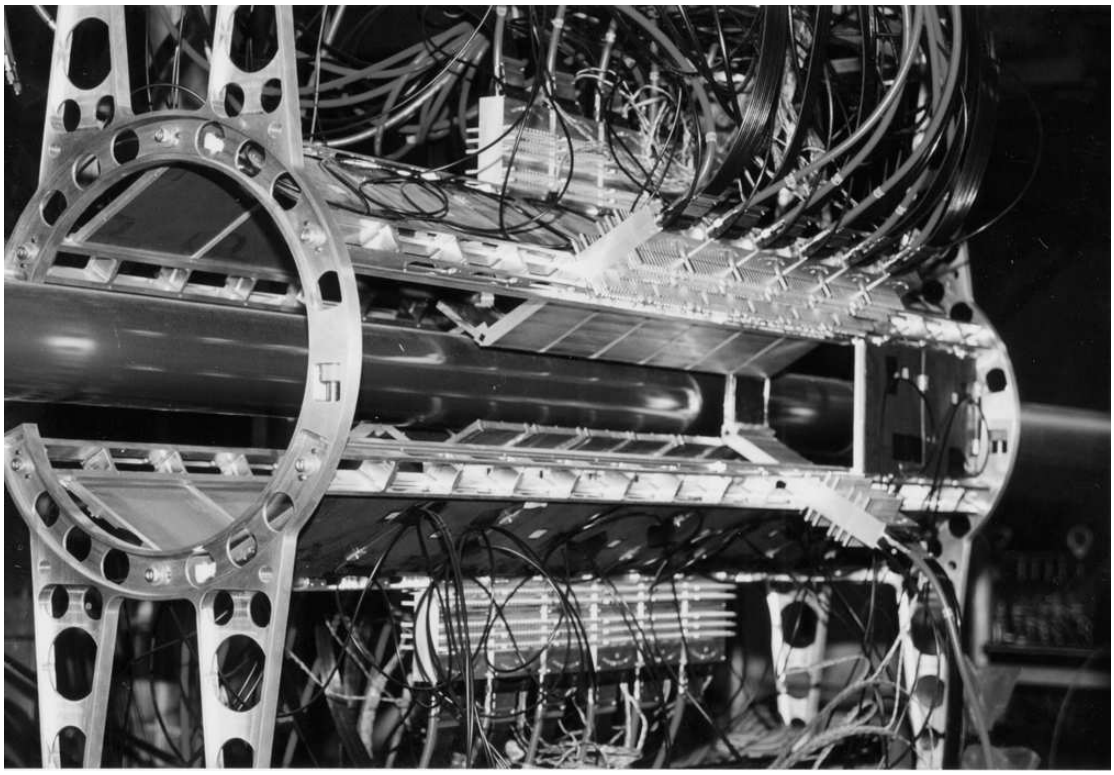

Figure 3.3: Centrality Array
Centrality detector viewed from the Midrapidity Spectrometer. To reduce the number of the secondary particles striking the Midrapidity Spectrometer, the centrality detector is not completely filled, which is easily seen in this picture.

number of particles produced in a collision. This particle multiplicity is then proportional to the event centrality. The multiplicity array is described in considerably greater detail in Chapter 4.

3.1.2 Beam-Beam Counter Arrays

The Beam-Beam Counters Arrays (BBC), which are shown in figure 3.4, consist of sets of Cherenkov radiators coupled with photomultiplier tubes (PMT) located at about 2.1 m from the nominal collision vertex along the beam axis on either side of the collision vertex. The left counter is made of forty-four radiators in a symmetric configuration around the beam pipe. The right counter is made of thirty-five radiators in an antisymmetric configuration to allow for the presence of the forward spectrometer detectors. As charged particles with velocity above the Cherenkov threshold hit the radiators, they create photons. The total number of photons produced can be related to the number of particles hitting a given radiator. With their good intrinsic timing, the counters provide vertex and timing information for the reaction. They are also used to measure the charged-particle multiplicity at large pseudorapidity.

3.1.3 Zero Degree Calorimeter

The Zero Degree Calorimeters, one of which is shown in figure 3.5, are located 12 m away from the nominal collision vertex along the beam axis on either side of the vertex location. They are made of three layers of absorber tungsten to produce shower particles from spectator neutrons that travel along the beam axis. Between the layers of tungsten, optical fibers are sandwiched as Cherenkov radiators. Cherenkov light produced by the shower particles is then guided to photomultiplier tubes by the same fibers. The measured time difference for particles hitting the ZDC on in either side of the vertex location can be used to determine the vertex position with very high efficiency.

3.2 Midrapidity Spectrometer

The Midrapidity Spectrometer, which is shown in figure 3.6, consists of two time projection chambers (TPM1 and TPM2) separated by a dipole magnet (D5), and a time-of-flight detector (TOFW). The spectrometer is located on a rotating platform that covers an angular range of 35° to 90°. Matching tracks in TPM1 and TPM2 through D5 magnet allows for the momentum of a

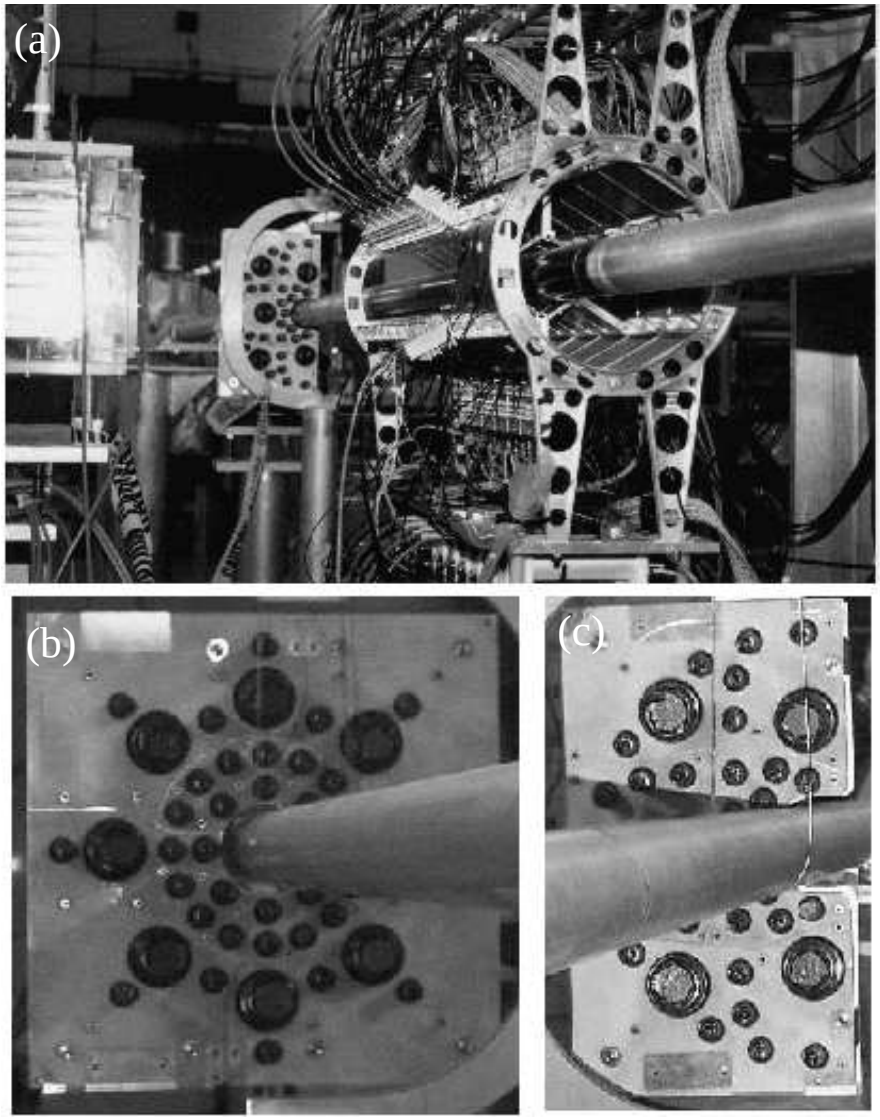

Figure 3.4: Beam-Beam Counters
(a) Right Beam-Beam counter is shown with Multiplicity Detectors and TPM1 (one of two TPCs from the Midrapidity Spectrometer). (b) Left Counter. (c) Right Counter.

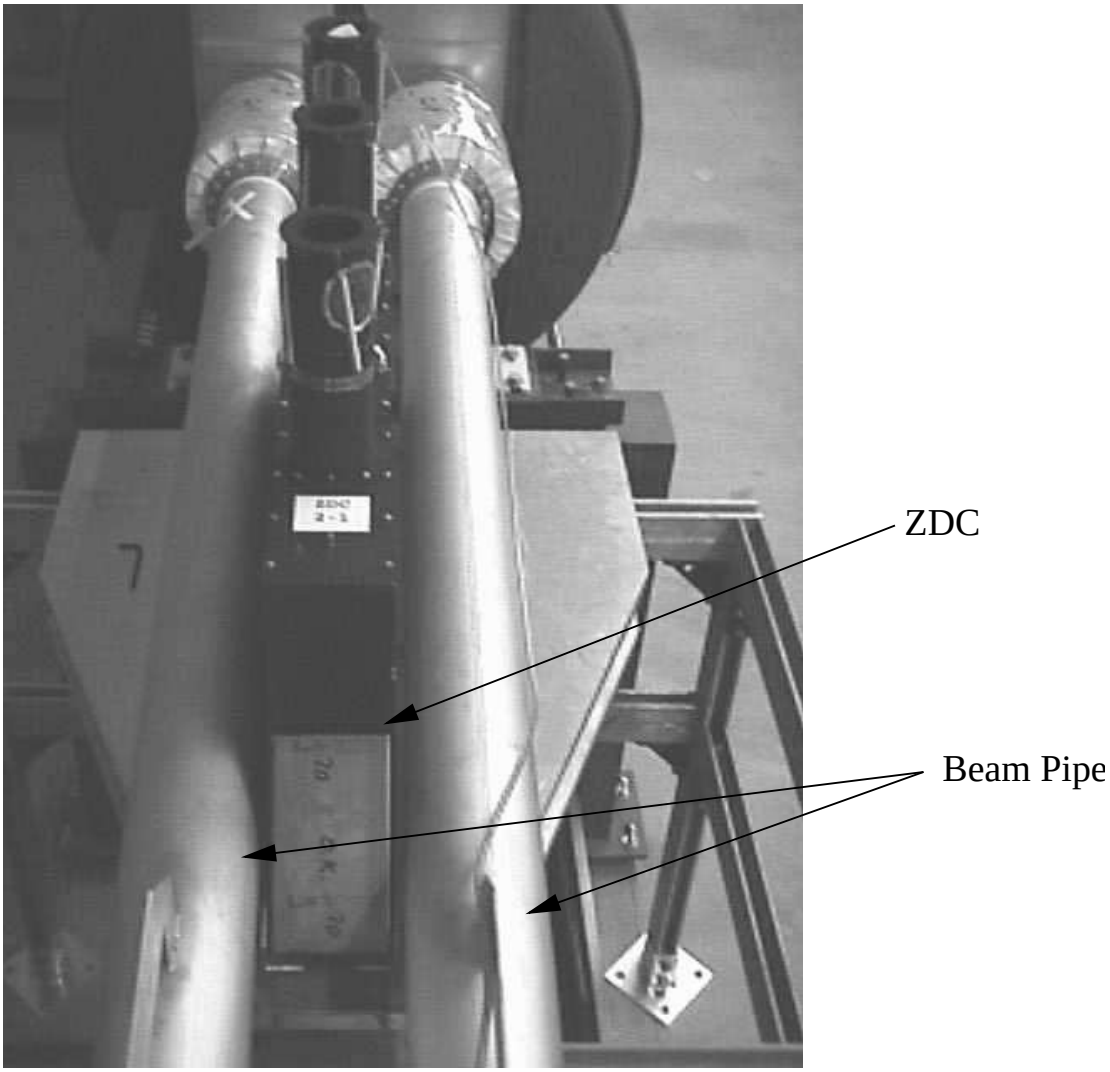

Figure 3.5: Zero Degree Calorimeter

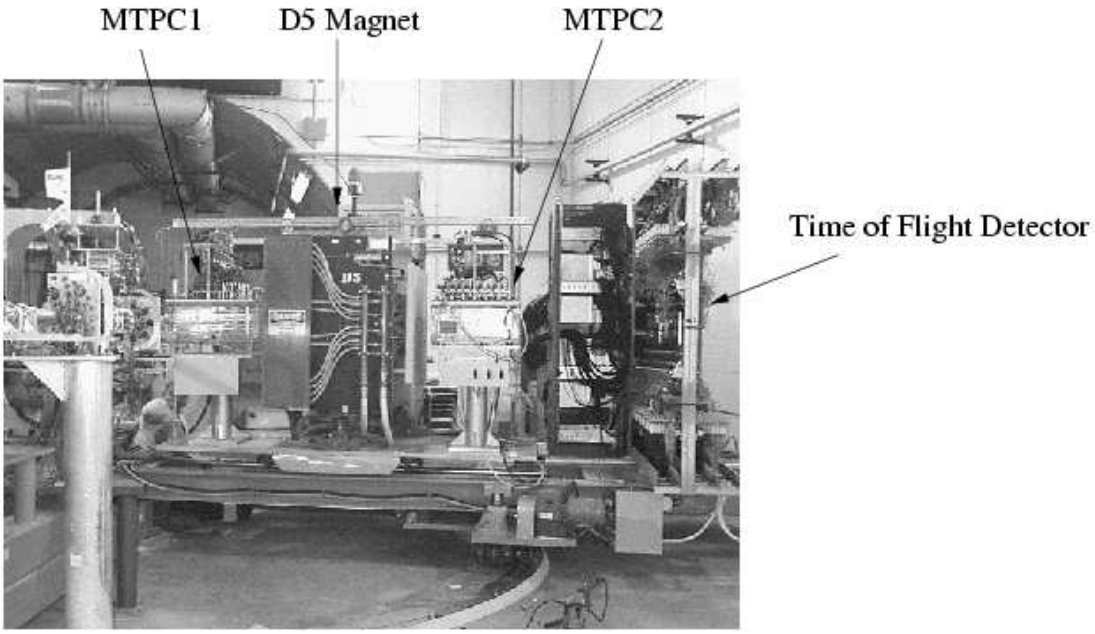

Figure 3.6: Midrapidity Spectrometer

particle to be determined. The relative time between the leading BBC counter tube being struck and the TOFW provides a measure of the flight time of a particle from the primary collision to the TOFW. With the momentum and the time-of-flight measurement, particle identification is possible. In addition, TPM1 can measure the vertex location by the projection of tracks inside the chamber to the vertical plane containing the beam pipe. More information about the use of TPM1 for vertex determination is found in Ref. [48]. The midrapidity spectrometer is described in more detail in Ref. [49].

3.3 Forward Spectrometer

The forward spectrometer consists of two independent spectrometers on separate swivel platforms: the front-forward spectrometer and the back-forward spectrometer.

3.3.1 Front-Forward Spectrometer

The Front-Forward Spectrometer, shown in Figure 3.7, consists of two magnets (D1 and D2), two time projection chambers (T1 and T2), a time-of-flight detector (H1) and a threshold Cherenkov detector (C1). It is located on the swivel platform that covers an angular range of 2.5° to 30°.

T1 and T2 with the D2 magnet provide sufficient information to determine the momentum

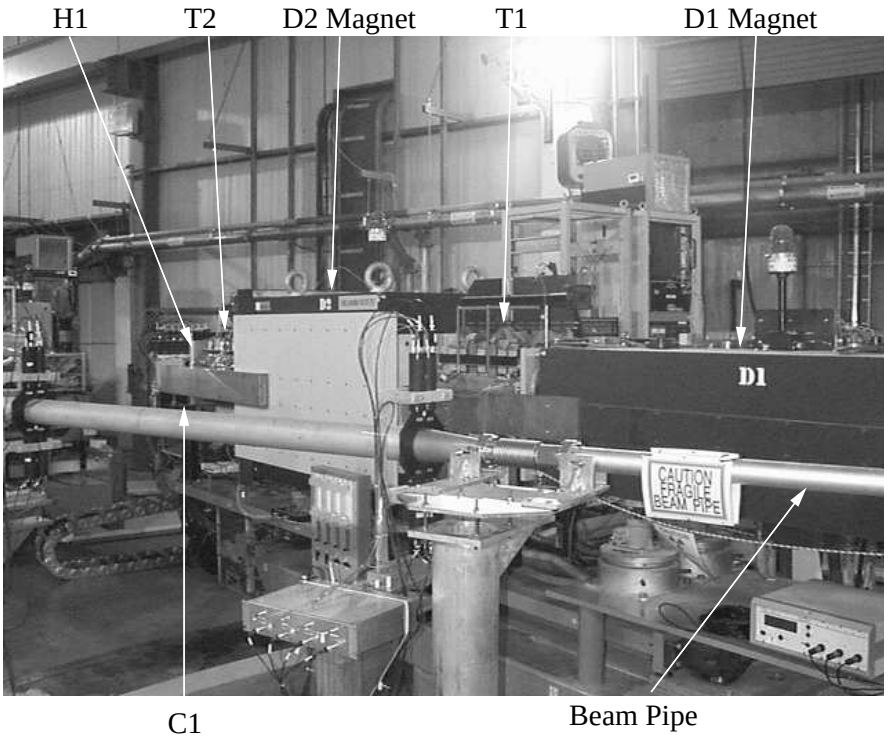

Figure 3.7: Front-Forward Spectrometer

of a particle. Together with the time of flight measurement provided by H1, it is possible to deduce the particle type. C1 provides additional information for particle identification. This spectrometer is described in greater detail in Ref. [49].

3.3.2 Back-Forward Spectrometer

The Back-Forward Spectrometer, shown in Figure 3.8, consists of two magnets (D3 and D4), three drift chambers (T3, T4 and T5), a time-of-flight detector (H2) and a ring imaging Cherenkov detector (RICH). It is located on a rotating platform that covers an angular range of 2.5° to 12°. By matching tracks in T3, T4 and T5 through two magnets, it is possible to determine the momentum of a particle. The additional time-of-flight information provided by H2 allows for particle identification. The RICH detector provides additional momentum and particle identification information for high-energy particles. This spectrometer system is described in greater detail in Ref. [49].

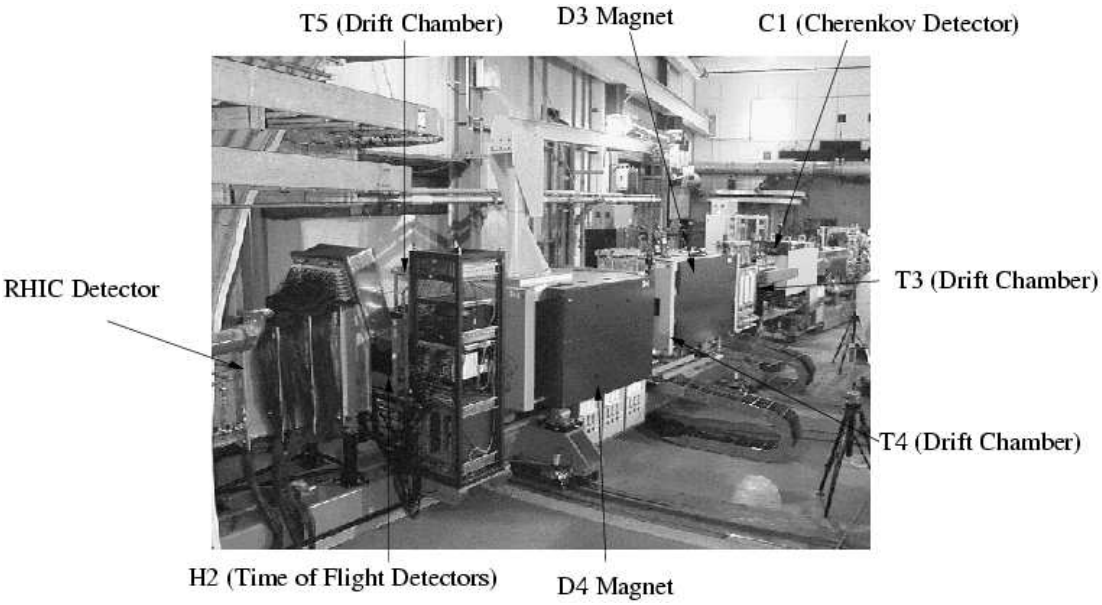

Figure 3.8: Back-Forward Spectrometer

Chapter 4

Detector Details for Multiplicity Measurement

In the BRAHMS experiment, charged-particle multiplicity is measured by three sets of detectors: the Silicon Strip Detector Multiplicity Array (SiMA), the Scintillation Tile Detector Multiplicity Array (TMA) and the Beam-Beam Counter arrays (BBC). The SiMA and the TMA measure the charged particle multiplicity at midrapidity ($|\eta| < 2.8$), whereas, the BBC arrays measures the charged particle multiplicity at large pseudorapidity ($2.6 < |\eta| < 4.7$).

4.1 Silicon Strip Detector Multiplicity Array (SiMA)

The SiMA, which is shown in Figure 4.1, is the BRAHMS system located closest to the interaction vertex. It is mounted in a hexagonal arrangement about the beryllium beam pipe. The distance to the beam axis is 5.3 cm. There are 25 wafers, each dimensioned $4cm \times 6cm \times 300\mu m$, with each wafer subdivided into 7 strips. The arrangement of detectors used in the year 2000 and 2001 runs are shown in Figure 4.2a and b, respectively. There are a maximum of 42 strips along the beam axis and 6 strips around the beam axis. The silicon detector configuration was designed to maximize the pseudorapidity at midrapidity while minimizing the background yields in the two spectrometers. As shown in Figure 4.2, there are no silicon detectors located between the interaction vertex and the front elements of the two spectrometers.

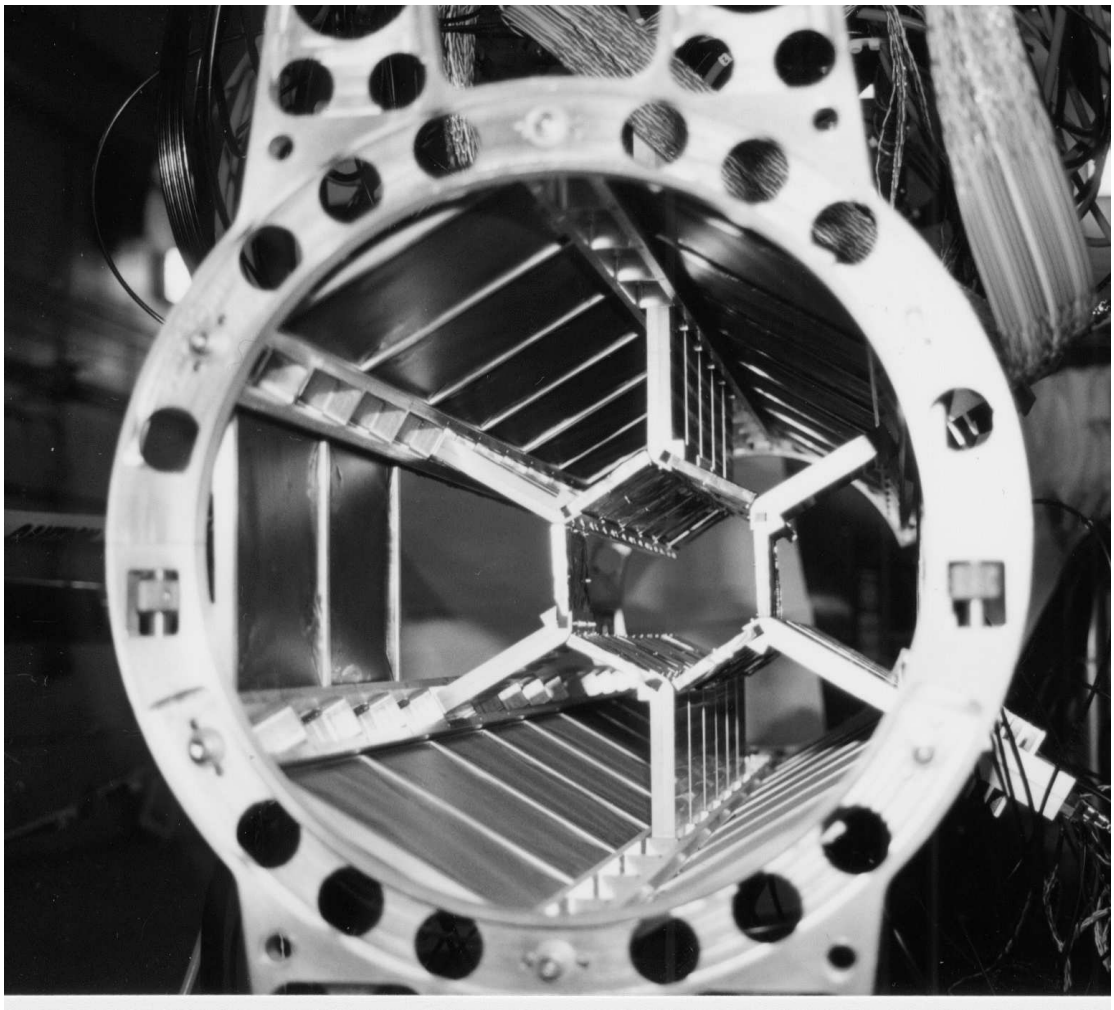

Figure 4.1: Multiplicity Array detector viewed along beam pipe
An outer hexagonal arrangement of Scintillation Tile detectors surrounds an inner hexagonal barrel of Silicon Strip detectors. The beam pipe, which is not shown here, travels through the middle of the inner hexagon.

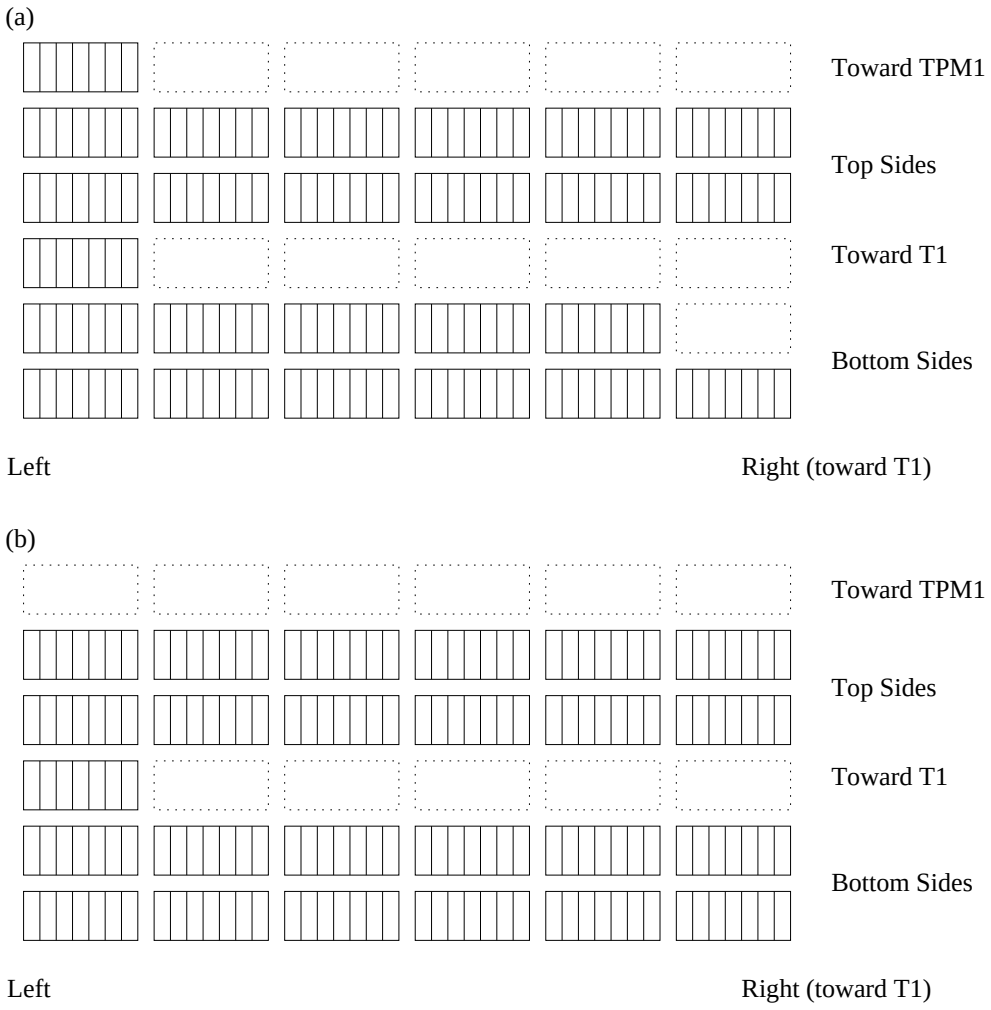

Figure 4.2: Arrangement of Silicon Strip Detectors
(a) during $\sqrt{s_{NN}}$ = 130 GeV run and (b) during $\sqrt{s_{NN}}$ = 200 GeV run. The change of configuration was made to reduce the background for TPM1.

The purpose of the silicon detectors is to estimate the centrality of an event by measuring the particle multiplicity of the event. As a charged particle traverses a silicon strip, it loses energy by producing electron-hole pairs. This leads to a current, which is detected and amplified to produce signals. The average energy loss of a particle is well known and described by the Bethe-Block equation. The formula is written as

$$-\frac{dE}{dx} = 2\pi N_a r_e^2 m_e c^2 \rho \frac{Z}{A}\frac{z^2}{\beta^2}\left[\ln\left(\frac{2m_e\gamma^2 v^2 W_{max}}{I^2}\right) - 2\beta^2 - \delta - 2\frac{C}{Z}\right] \tag{4.1}$$

where

$$\begin{aligned}
r_e &= \text{classical electron radius,} \\
v &= \text{velocity of the particle,} \\
m_e &= \text{electron mass,} \\
N_a &= \text{Avogadro's number,} \\
I &= \text{mean excitation potential,} \\
Z &= \text{atomic number of absorbing material,} \\
A &= \text{atomic weight of absorbing material,} \\
\rho &= \text{density of absorbing material,} \\
z &= \text{charge of incident particle in units of e,} \\
M &= \text{mass of incident particle,} \\
\beta &= v/c \quad , \\
\gamma &= 1/\sqrt{1-\beta^2} \quad , \\
\delta &= \text{density correction factor,} \\
C &= \text{shell correction factor,} \\
W_{max} &= \text{maximum energy transfer in a single collsion, and} \\
&= \frac{2m_e c^2 \beta^2 \gamma^2}{1 + 2\frac{m_e}{M}\sqrt{1+\beta^2\gamma^2} + \left(\frac{m_e}{M}\right)^2} \quad .
\end{aligned}$$

Using Equation 4.1, the stopping power dE/dx can be easily plotted for different particle species.

Figure 4.3 shows the stopping power of pions, kaons and protons in silicon. It is interesting to

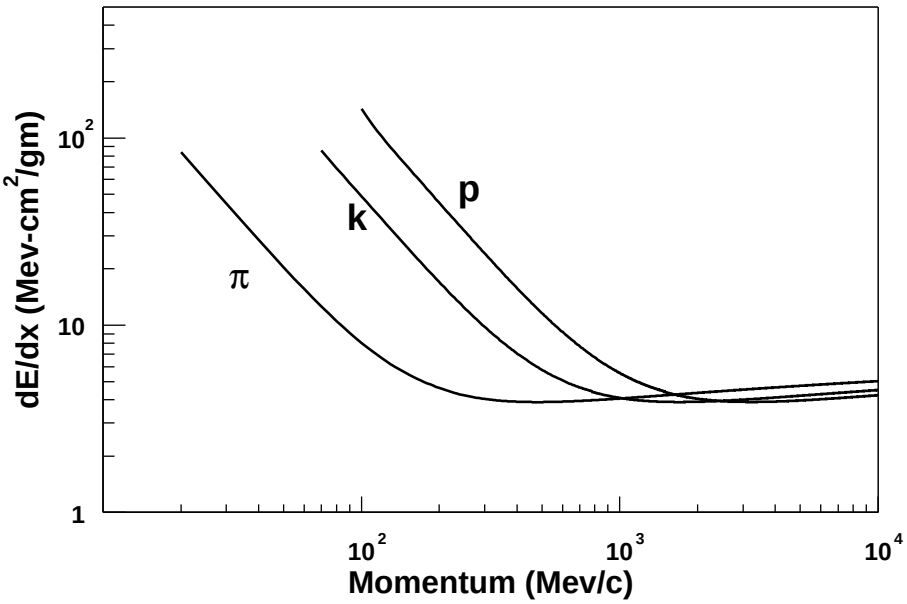

Figure 4.3: Stopping Power for Silicon

note that for all three particle types the stopping power decreases rapidly until their momenta reach about 2.5 times their rest mass. After that, it starts to increase slowly. (The measured relativistic rise in stopping power is even lower than what Figure 4.3 indicates as a result of production of δ-rays which may escape from the the detector. Therefore, the stopping power remains relatively flat after it passes the minimum value.) A particle whose stopping power is near the minimum of the energy loss curve is said to be "minimum ionizing". Since most of the particles produced in relativistic collisions are minimum ionizing, the detected energy can be used to estimate the number of produced particles in a collision.

Since the energy loss of a particle is statistical in nature, any given particle will most likely not lose the exact amount of energy given by Equation 4.1. Instead, there will be a distribution of energy loss with a mean value described by Equation 4.1. If the incident particle is slow, or the thickness of the detector is large, the distribution is Gaussian. This is the typical situation for surface-barrier type detectors used in the low energy nuclear physics, where the incident particles lose considerable energy or are even stopped within the detectors. However, in relativistic heavy-ion physics, the detected particles are typically minimum ionizing and lose only a small amount

of energy passing through a detector. In this case, which was first calculated by Landau [50], the distribution is skewed because there exists the probability of large energy loss in a single collision within the relatively small number of collisions the incident particle suffers. Figure 4.4 compares typical Gaussian and Landau distributions. Unlike the Gaussian distribution, the

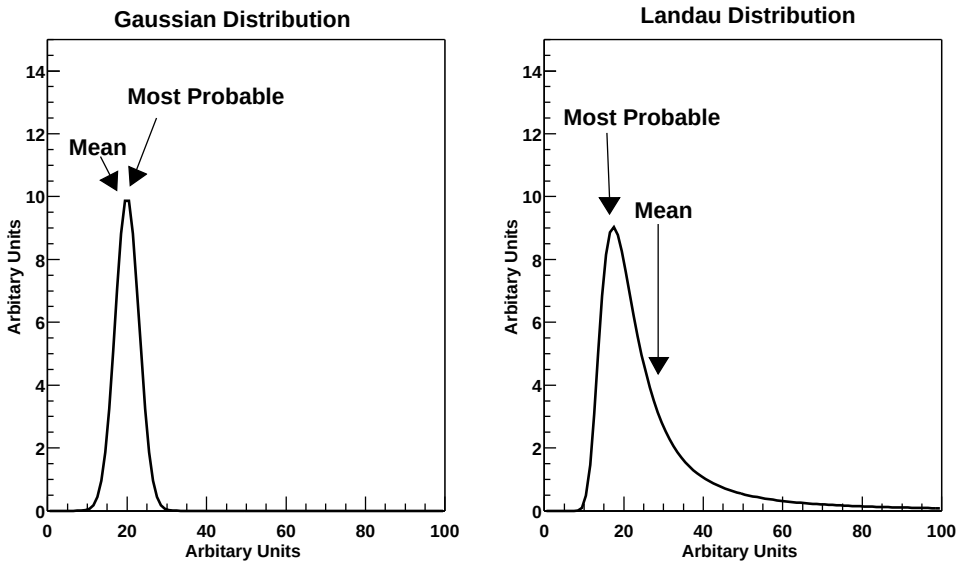

Figure 4.4: Gaussian and Landau Distribution

Landau distribution has a characteristically long tail, reflecting the large fluctuation in energy loss of a particle traversing a thin material.

4.1.1 General Properties of Semiconductor Detector

Silicon strip detectors are a type of semiconductor detector. They consist of crystalline materials and have a characteristic energy band structure in their outer atomic electrons. Typically, the energy band structures of insulators, semiconductors and conductors, which are schematically represented in Figure 4.5, are used to distinguish among these three types of materials. Energy bands are regions where there are many closely spaced discrete levels of atomic electrons. As a consequence of the periodic arrangement of atoms in the crystal, wave-functions of atomic electrons overlap each other. Since electrons are fermions, they follow the Pauli exclusion principle, which prohibits more than one pair of electrons (with their two different spins) in the same energy state. This leads to a large number of discrete electron energy levels. In these

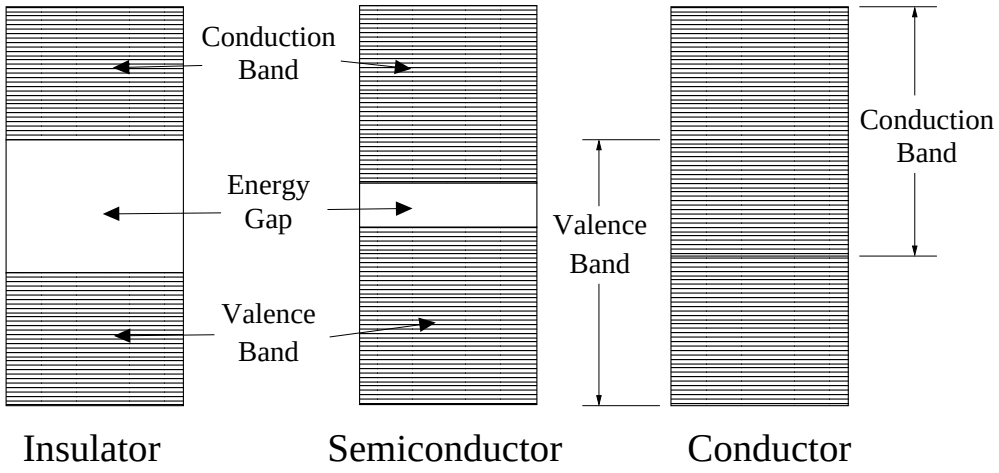

Figure 4.5: Energy Band

discrete energy levels, there exist two distinct regions: a conduction band and a valence band. The highest energy band is the conduction band where electrons are free to move. The lowest energy band is called the valance band where electrons are tightly bound to their parents' atoms. Hence, these electrons do not conduct electricity. Between these two bands, there is a region called the energy gap, in which no atomic electron can occupy. This energy gap can be viewed as threshold energy, which electrons must overcome to conduct electricity. The characteristics of the energy gap distinguish the three types of materials.

For insulators and semiconductors, there is an energy gap. Without thermal energy, none of the electrons in insulators and semiconductors have sufficient energy to overcome this gap. Therefore, insulators and semiconductors do not conduct electronic current at 0° K. The difference between insulators and semiconductors is the size of their respective energy gaps. The energy gap is relatively small (about 1 eV) for semiconductors whereas it is large for conductors (approximately several eV). Therefore, in semiconductors, electrons with small but sufficient thermal energy can jump from the valence band to the conduction band by leaving holes in the valence band. At this point, the semiconductor conducts electricity. Hence the name semiconductor. However, in insulators, the size of the gap is too large for electrons to overcome. As a result, these materials do not conduct electricity. In comparison, conductors do not have energy gaps and will conduct electricity at any temperature.

The ground state atomic structure of silicon is $1s^2 2s^2 2p^6 3s^2 3p^2$. To form the material, the outer 4 electrons from $3s$ and $3p$ states of one atom bond with 4 electrons from surrounding

atoms. This is shown in Figure 4.6a. At normal temperature, thermal energy can excite these electrons into the conduction band leaving holes (seen in Figure 4.6b). To create radiation

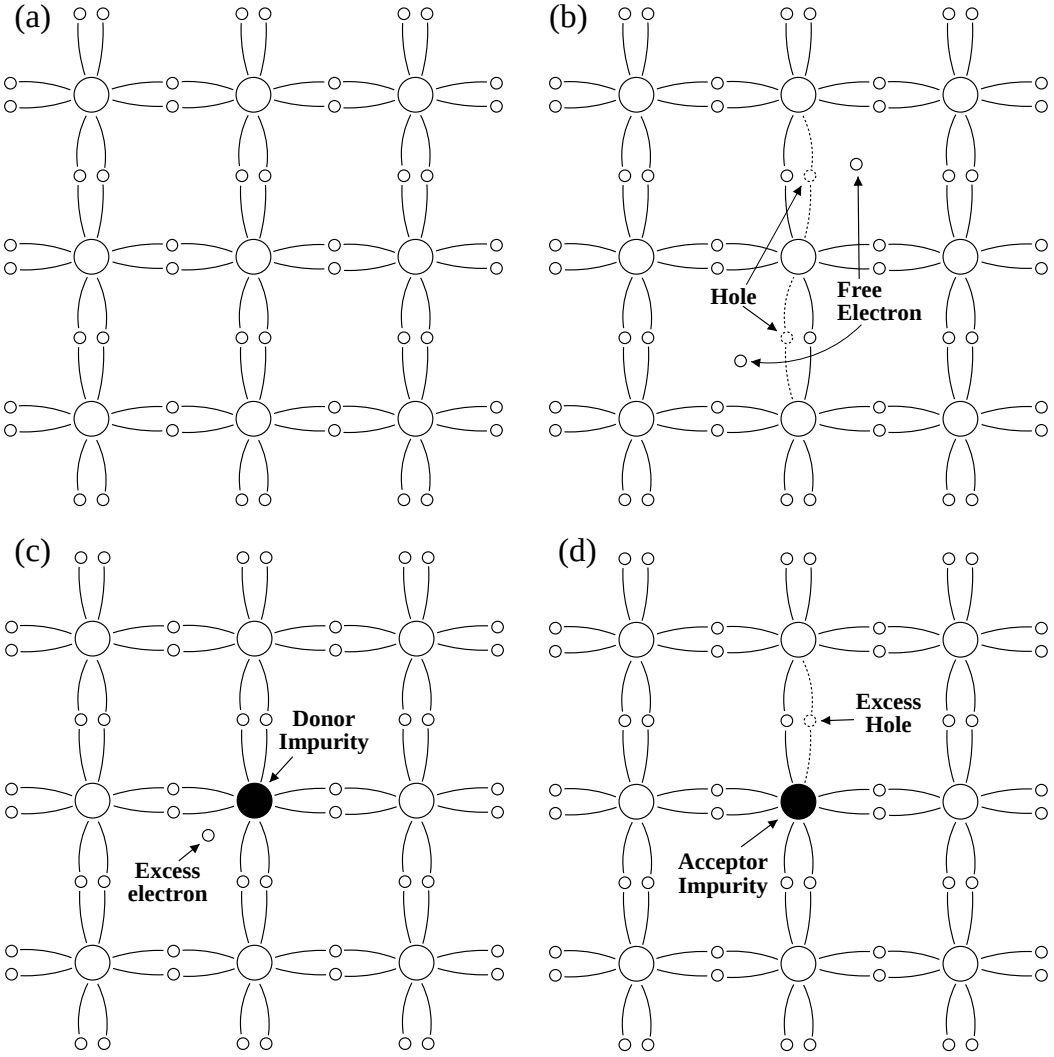

Figure 4.6: Lattice of Silicon
(a) at 0° (b) at sufficiently high temperature to creates electron-hole pairs (c) addition of donor impurities to create n-type semiconductors (d) additions of acceptors to create p-type semiconductors

detectors using silicon, it is necessary to add an impurity to the pure silicon material. When the impurity is pentavalent, that is, with 5 electrons in the outer atomic shells, as found in phosphorus and arsenic, only 4 electrons of the impurity donor are used to bond with the surrounding silicon, leaving one free electron. This case is shown in Figure 4.6c, and is referred to as n-type material. If the impurity is trivalent, that is, with 3 electrons in the outer atomic

shells, as found in boron and gallium, 3 electrons are used to bond to the surrounding silicon with one hole remaining. This case is shown in Figure 4.6d, and results in p-type material. It is important to note that n-type and p-type materials are electrically neutral despite the perceived extra electrons or holes since the original silicon and added impurities are electrically neutral.

When n-type and p-type materials are formed together, they create a semiconductor junction. Since the two types of material have different concentrations of electrons and holes, a diffusion layer will form after the junction is made. Electrons from the n-type material will go to the side of the p-type material and fill holes or vice versa. This leads to the sides of the n-type and p-type materials close to the junction to become either positively or negatively charged, as shown in Figure 4.7a. This charge build-up creates an electric field between the two sides of the junctions.

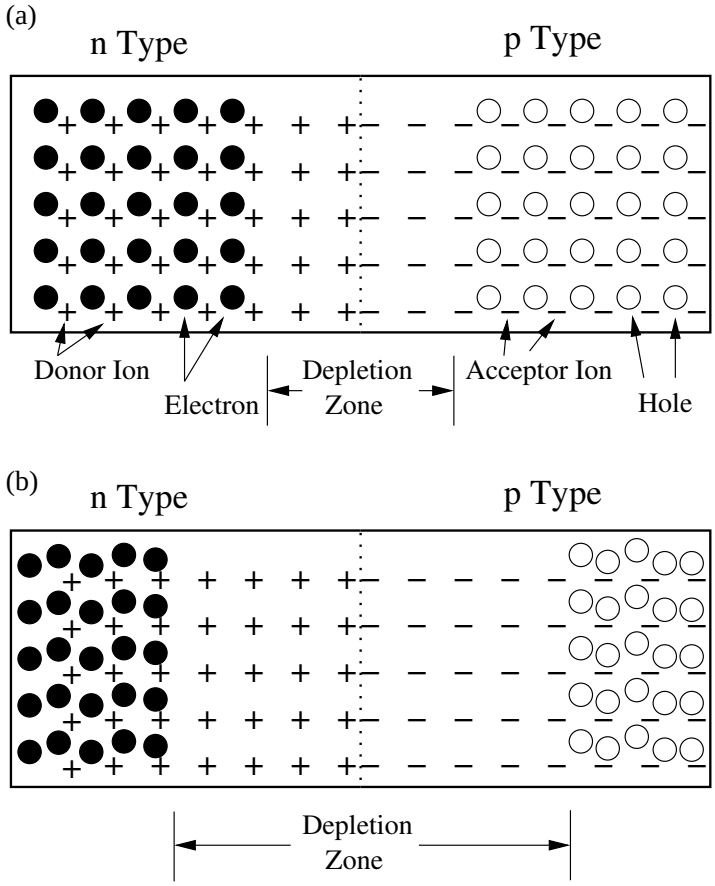

Figure 4.7: np junction

A gap is created where there are no mobile charge carriers. Any electron or hole entering this region will be swept away by the electric field. This region is known as a "depletion zone". Since

ionization radiation entering this space will create electron-hole pairs, which are swept away by the electric field, this junction can be used to detect the radiation. Typically, to increase the size of the radiation sensitive area, positive and negative voltages are applied to the n-type and p-type sides, respectively. This leads to a "reverse bias" situation. The positive voltage applied to the n-type material will attract mobile electrons away from the junction, and the negative voltage applied to the p-type material will attract mobile holes away from the junctions, thus increasing the depletion depth.

Another reason for wanting to increase the depletion depth is to reduce the detector capacitance, an important consideration for the electric noise. The capacitance of 2 parallel planes of area A separated by distance d is given by

$$C = \varepsilon \frac{A}{d} \tag{4.2}$$

where ε is the permittivity of the space between the two planes. The capacitance scales as the inverse of the depletion layer thickness.

4.1.2 Pre-Amplifier and Shaper Electronics

The detailed schematic diagram of the pre-amplifier and shaper amplifier electronics for the silicon strip detectors is shown in Figure 4.8. It consists of five different stages: a charge sensitive pre-amplifier, a pole zero controller, a shaping amplifier, shaper, and a final buffer amplifier stage.

The generic design of a charge-sensitive pre-amplifier is shown in Figure 4.9. The output of a charge-sensitive pre-amplifier depends on the time-integrated current at its input. This is in contrast to a voltage-sensitive pre-amplifier where the output signal for a given current pulse depends on the input capacitance. Since the capacitance of the semiconductor detector depends on the operating temperature, it is very undesirable to use voltage-sensitive pre-amplifiers. Referring to Figure 4.9, if the charged collected by the detector and sent to the pre-amplifier is Q, the output voltage of the circuit without considering R_f is given by

$$V_o = \frac{Q}{C_f} \quad . \tag{4.3}$$

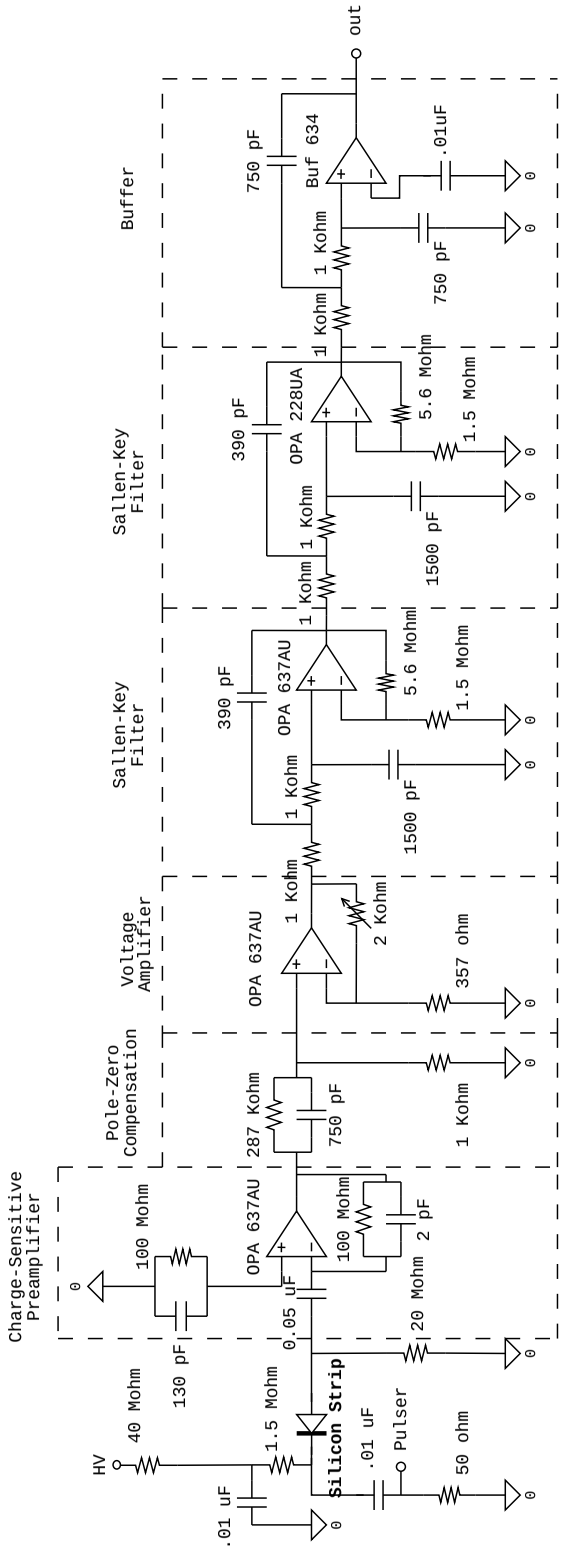

Figure 4.8: Diagram of pre-amplifier and shaper electronics

To avoid buildup of charge on the feedback capacitor C_f, it is necessary to place a discharge resistor R_f in parallel with C_f. This can be seen by looking at the transfer function of this circuit in the s domain (or complex frequency):

$$\frac{V_o}{V_i} = -\frac{Z_f}{Z_i} \tag{4.4}$$

$$= -\frac{R_f / (sC_f R_f + 1)}{1/sC_i} \tag{4.5}$$

$$= -\frac{R_f}{\frac{C_f}{C_i} R_f + \frac{1}{sC_i}} \tag{4.6}$$

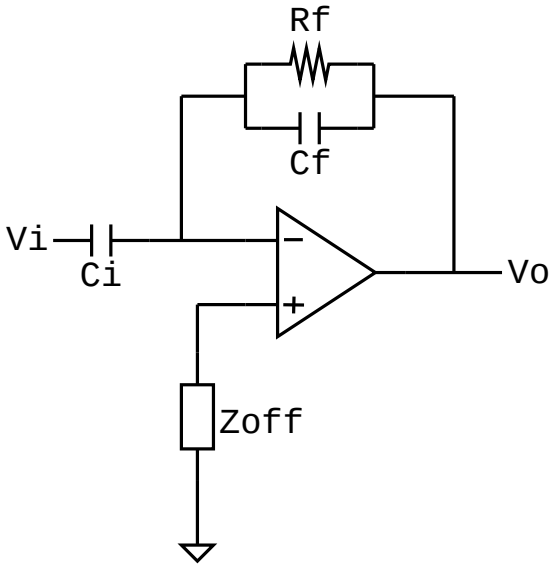

Figure 4.9: Charge Sensitive Pre-Amplifier

It is noticed from Equation 4.6 that it is a high pass filter with the cut-off frequency of

$$\omega_{cut-off} = \frac{1}{\left(\sqrt{2}+1\right) C_f R_f} \quad . \tag{4.7}$$

Therefore, R_f is used to reduce the slow charge buildup of this circuit. Using the values from Figure 4.8, the actual value for the cut-off frequency is

$$\omega_{cut-off} \approx 2 \times 10^3 \ (rad/sec)$$

$$or \quad 300 \ Hz \quad .$$

The shaper amplifier consists of two stages of the Sallen-Key filter circuit. The general form of the Sallen-Key filter is shown in Figure 4.10. Assuming the ideal operational amplifier (op-

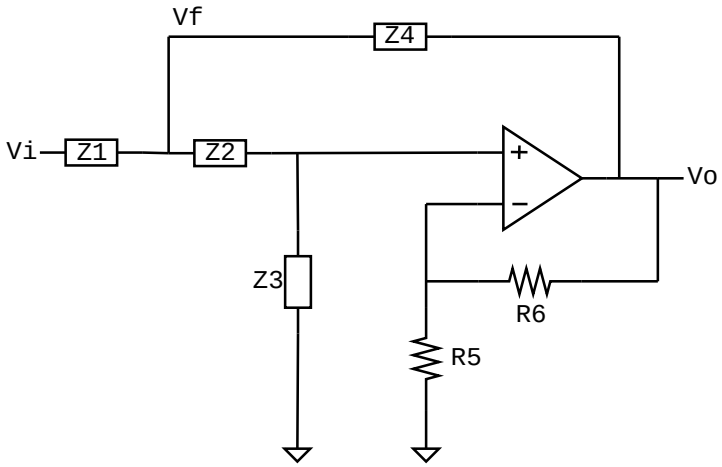

Figure 4.10: Sallen-Key Filter

amp), the transfer function of this circuit can be obtained. The voltage at the negative input, V_n, is

$$V_n = \frac{R_5}{R_5 + R_6} V_o \quad . \tag{4.8}$$

Since V_n is equal to the voltage at the positive input for an ideal op-amp, and since there is no current flowing to the inputs of the op-amp, the current through the elements Z_3 and Z_2 can be given by

$$i_{Z_2} = i_{Z_3} = \frac{V_n}{Z_3} = \frac{V_p}{Z_3} = \frac{R_5}{Z_3 (R_5 + R_6)} V_o \quad . \tag{4.9}$$

Therefore, the feedback voltage V_f is

$$V_f = i_{Z_2} Z_2 + V_p \tag{4.10}$$

$$= \frac{Z_2 R_5}{Z_3 (R_5 + R_6)} V_o + \frac{R_5}{R_5 + R_6} V_o \tag{4.11}$$

$$= \frac{Z_2 R_5 + Z_3 R_5}{Z_3 (R_5 + R_6)} V_o \quad . \tag{4.12}$$

By knowing V_f, the current for the element Z_4 can be calculated as

$$\begin{aligned} i_{Z_4} &= \frac{V_f - V_o}{Z_4} && (4.13)\\ &= \frac{1}{Z_4}\left\{\frac{Z_2R_5 + Z_3R_5}{Z_3\left(R_5+R_6\right)} - 1\right\}V_o && (4.14)\\ &= \frac{Z_2R_5 + Z_3R_5 - Z_3R_5 - Z_3R_6}{Z_3Z_4\left(R_5+R_6\right)}V_o && (4.15)\\ &= \frac{Z_2R_5 - Z_3R_6}{Z_3Z_4\left(R_5+R_6\right)}V_o \quad . && (4.16) \end{aligned}$$

Also, the current through Z_1 is

$$\begin{aligned} i_{Z_1} &= i_{Z_2} + i_{Z_4} && (4.17)\\ &= \frac{R_5}{Z_3\left(R_5+R_6\right)}V_o + \frac{Z_2R_5 - Z_3R_6}{Z_3Z_4\left(R_5+R_6\right)}V_o && (4.18)\\ &= \frac{Z_4R_5 + Z_2R_5 - Z_3R_6}{Z_3Z_4\left(R_5+R_6\right)}V_o \quad . && (4.19) \end{aligned}$$

Therefore, the input voltage is

$$\begin{aligned} V_i &= i_{Z_1}Z_1 + V_f && (4.20)\\ &= \frac{Z_4R_5 + Z_2R_5 - Z_3R_6}{Z_3Z_4\left(R_5+R_6\right)}V_oZ_1 + \frac{Z_2R_5 + Z_3R_5}{Z_3\left(R_5+R_6\right)}V_o && (4.21)\\ &= \frac{Z_1Z_4R_5 + Z_1Z_2R_5 - Z_1Z_3R_6 + Z_2Z_4R_5 + Z_3Z_4R_5}{Z_3Z_4\left(R_5+R_6\right)}V_o \quad . && (4.22) \end{aligned}$$

Then, the ideal transfer function is

$$\begin{aligned} \frac{V_o}{V_i} &= \frac{Z_3Z_4\left(R_5+R_6\right)}{Z_1Z_4R_5 + Z_1Z_2R_5 - Z_1Z_3R_6 + Z_2Z_4R_5 + Z_3Z_4R_5} && (4.23)\\ &= \frac{\frac{R_5+R_6}{R_5}}{\frac{Z_1Z_2}{Z_3Z_4} + \frac{Z_1}{Z_3} + \frac{Z_2}{Z_3} + \frac{Z_1}{Z_4}\left(1 - \frac{R_5+R_6}{R_5}\right) + 1} \quad . && (4.24) \end{aligned}$$

Comparing Figure 4.8 and 4.10, it is seen that $Z_1 = R_1$, $Z_2 = R_2$, $Z_3 = \frac{1}{sC_3}$ and $Z_4 = \frac{1}{sC_4}$. Therefore, the transfer function becomes

$$\frac{V_o}{V_i} = \frac{\frac{R_5+R_6}{R_5}}{s^2\left(R_1R_2C_3C_4\right) + s\left\{R_1C_3 + R_2C_3 + R_1C_4\left(1 - \frac{R_5+R_6}{R_5}\right)\right\} + 1} \quad . \qquad (4.25)$$

The standard transfer function of a second order low pass filter can be written as

$$H = \frac{K}{-\left(\frac{f}{f_c}\right)^2 + j\frac{f}{Qf_c} + 1} \tag{4.26}$$

where

$$\begin{aligned} K &\equiv \text{gain for low frequency,} \\ Q &\equiv \text{quality factor,} \\ f &\equiv \text{frequency , and} \\ f_c &\equiv \text{corner frequency .} \end{aligned}$$

Then, by letting $s = j2\pi f$ in equation 4.25, f_c, K and Q can be written as

$$f_c = \frac{1}{2\pi\sqrt{R_1 R_2 C_3 C_4}} \quad , \tag{4.27}$$

$$K = \frac{R_5 + R_6}{R_5} \quad \text{, and} \tag{4.28}$$

$$Q = \frac{\sqrt{R_1 R_2 C_3 C_4}}{R_1 C_3 + R_2 C_3 + R_1 C_4 \left(1 - \frac{R_5 + R_6}{R_5}\right)} \quad . \tag{4.29}$$

Using the values from Figure 4.8, one finds

$$f_c \approx 200 \text{ KHz,} \tag{4.30}$$

$$K \approx 5, \tag{4.31}$$

$$Q \approx 0.5 \quad \text{, and} \tag{4.32}$$

$$\frac{V_o}{V_i} = \frac{4.7}{5.8 \times 10^{-13} s^2 + 1.54 \times 10^{-6} s + 1} \quad . \tag{4.33}$$

Therefore, for $f \ll f_c$, the gain is about 5.

Between the charge-sensitive pre-amplifier and the first Sallen-Key stage, there is a pole-zero compensation circuit. The general circuit is shown in Figure 4.11. The transfer function of this

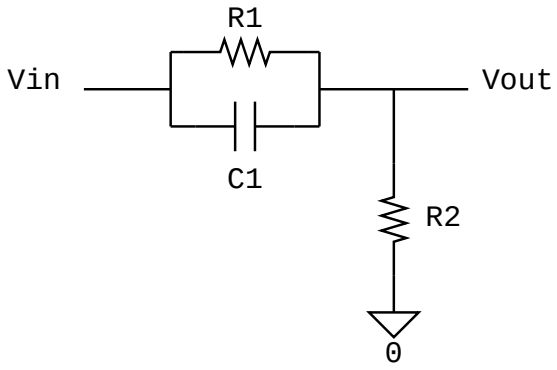

Figure 4.11: Pole-Zero Compensation Circuit

circuit is

$$\frac{V_{out}}{V_{in}} = \frac{R_2}{R_2 + \frac{R_1}{sC_1R_1}} \tag{4.34}$$

$$= \frac{sC_1R_1R_2 + R_2}{sC_1R_1R_2 + R_1 + R_2} \tag{4.35}$$

$$= \frac{s + \frac{R_2}{cR_1R_2}}{s + \frac{R_1+R_2}{cR_1R_2}} \quad . \tag{4.36}$$

The purpose of this function is to add stability to the electronics and to remove the under-shoot (or overshoot) of the output pulses. In the analysis of the feedback system, values of s that makes the denominator of the transfer function become zero are called poles. Values of s that make the numerator of the transfer function become zero are called zeros. The stability of a system such as the Sallen-Key circuit used here can be improved by adding an additional transfer function [51]. Ideally, the additional transfer function has zeros that cancel poles of the original transfer functions. However, the other requirements as well as the availability of electric components put limits on the design of compensation transfer functions. Using the values in Figure 4.8, the compensation transfer function is

$$\frac{V_{out}}{V_{in}} = \frac{s + 5000}{s + 1.34 \times 10^6} \quad . \tag{4.37}$$

This clearly does not cancel the poles from Equation 4.33. However, since Equation 4.37 has the attenuation of $5000/10^6$ at low frequency, it will attenuate under-shoots of any low frequency.

Since the addition of the pole-zero compensation circuit attenuates the signal, an adjustable

amplification stage was introduced between the pole-zero and Sallen-Key stages. It is very simple non-inverting amplifier, as is shown in Figure 4.12. The transfer function is written as

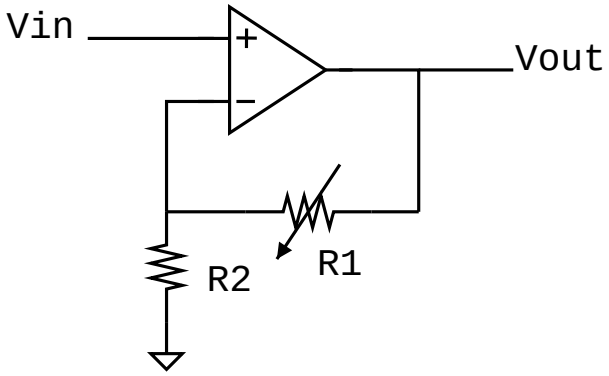

Figure 4.12: Non-inverting Adjustable Amplifier

$$\frac{V_{out}}{V_{in}} = \frac{R_1 + R_2}{R_2} \quad . \tag{4.38}$$

Using the values from Figure 4.8, the gain can be adjusted in the range of 1 to 10.

The last stage of the pre-amplifier shaper electronics is the buffer stage. It is designed to isolate output signals from the internal signals of the amplifier. In particular, it is necessary to produce a 50 ohm termination impedance for the output pulses. From Figure 4.8, the buffering stage is accomplished by the single operational amplifier.

4.1.3 Attenuator

An amplified analog signal from the current pre-amplifier-shaper electronics has a maximum voltage of about 6 volts. Since the signal is sent to a peak-to-charge module (PTQ) which, as discussed in the next section, has a maximum allowed voltage of 2 (or -2) volts, it is necessary to attenuate the amplifier output. Figure 4.13 shows the diagram of the attenuator used for this purpose. As seen in this figure, it is a simple voltage divider with a buffer amplifier used at the output for the signal sent to the PTQ. The level of attenuation is adjustable by the single variable resistance potentiometer. Also, the DC-offset level can be adjusted by a second potentiometer.

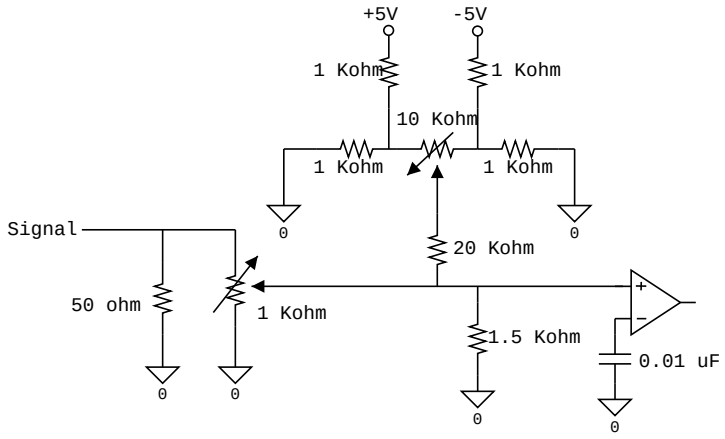

Figure 4.13: Diagram of Attenuator

4.1.4 PTQ

A PTQ module is located between the attenuator stage and the final fast-encoding analog-to-digital converter (FERA) for two purposes: peak stretching and attenuation. (See Figure 4.14) (Section 6.1.2 presents detailed description of this device characteristics.) The peak stretching function holds the size of the input signal for the gate period set for the FERA. The signals from the SiMA detectors have rise times of approximately 6 μs with a maximum amplitude of 6 V. Because of this slow rise time, it is not possible to include the entire signal within the FERA gate. Rather, the PTQ holds the peak value of the pulse for the duration of the FERA gate, which is delayed to occur after the peak is reached. Additionally, the PTQ provides an attenuation of 10 to produce an appropriate size pulse for the FERA module.

4.1.5 Data Acquisition

Acquisition of data involves several stages, some of which are discussed in the earlier section of this chapter. The basic diagram of the data acquisition for the SiMA is shown in Figure 4.14. A trigger for events is made by the Beam Beam Counters arrays (BBC) and the Zero Degree Calorimeter (ZDC). Each of these systems produce fast signals, which can be logically OR'ed to produce a timing signal for the event. The ZDC is a minimum bias detector and is estimated to be close to 100 % efficient. The BBC arrays are about 75% efficient with a factor of three better timing resolution than the ZDCs. The timing signal made by the BBC arrays and the ZDCs are delayed appropriately for the use of the PTQ and ADC. The digitized signals are then recorded

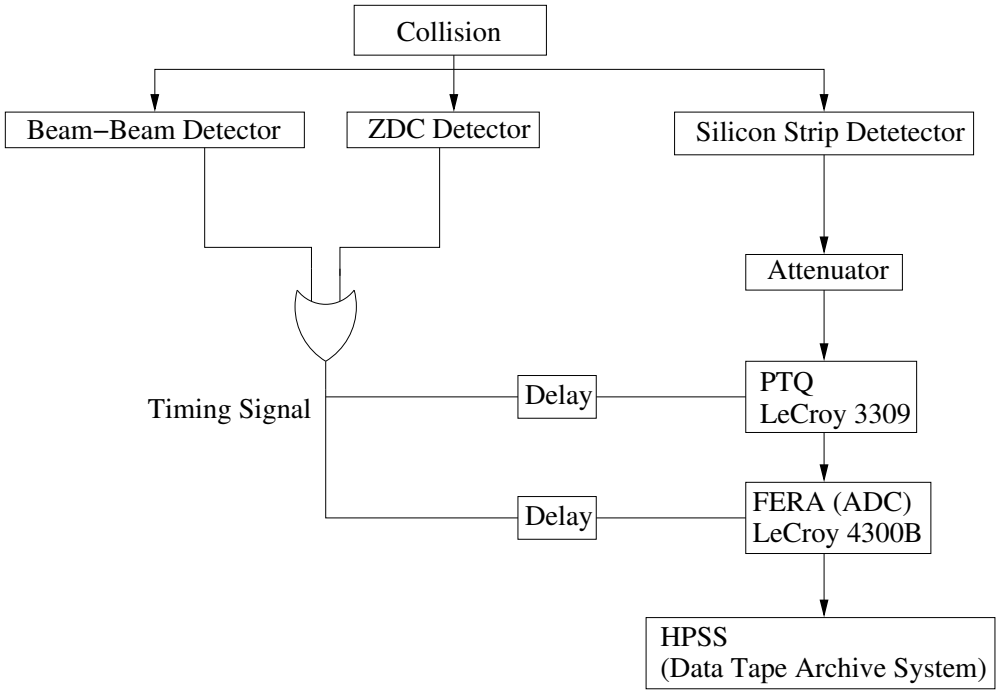

Figure 4.14: Data Acquisition Diagram for Silicon Strip Detector

to the RHIC HPSS data tape system for the subsequent analysis.

4.2 Scintillation Tile Detector Multiplicity Array (TMA)

The TMA shown in Figure 4.1 is located just outside of the SiMA with the same hexagonal shape. The distance from the beam axis to the front face of the detector is 13.86 cm. A planar view of the 38 tiles is shown in Figure 4.15. Each of tiles is dimensioned 12 cm x 12 cm x 0.5 cm. Again, the sides of the TMA facing the TPM1 and T1 detectors in the two spectrometer arms, respectively, are left empty to reduce background rates in these TPC detectors. The TMA has about a 60% larger solid angle coverage than the SiMA. From the nominal vertex location, the TMA covers the pseudorapidity range of $|\eta| < 2.2$.

Each scintillator tile is coupled with a wavelength-shifting optical fiber to guide photons created in the scintillator to a photo multiplier tube (PMT). Figure 4.16 shows the groove for this fiber. The reason for the wavelength-shifting fiber is to match the wave length of light created in the tile to the wavelength of optimum detection efficiency in the PMT. Two turns of the fiber are wound about the groove for good light collection. Both ends of the fiber are

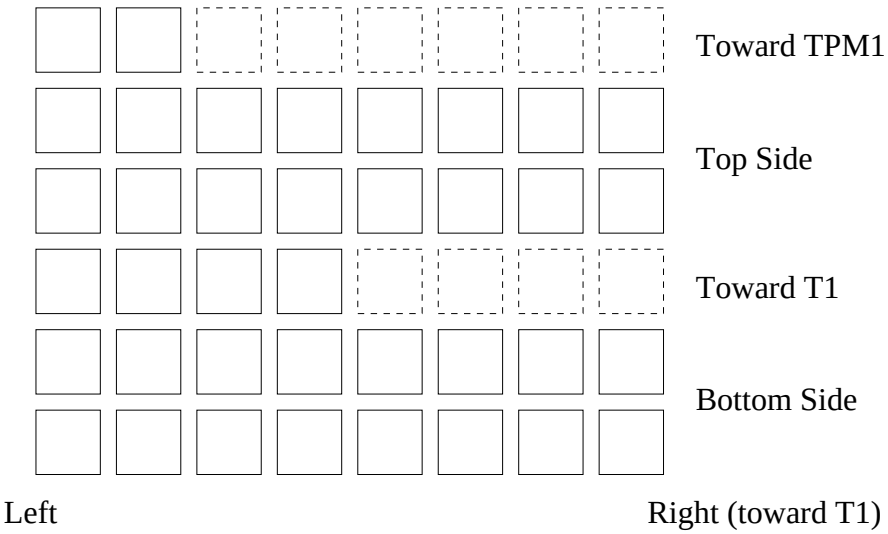

Figure 4.15: Configuration of Scintillator Tile Detector

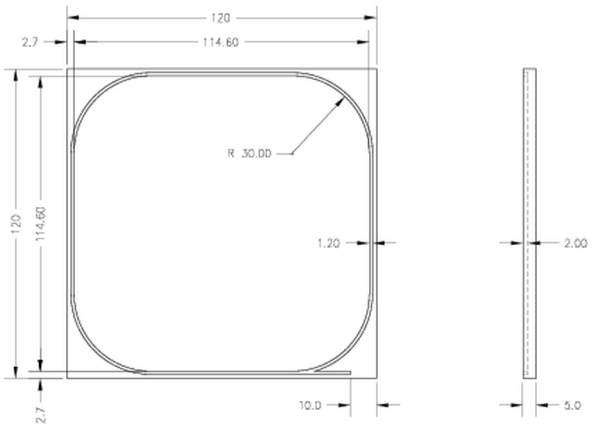

Figure 4.16: Detail Schematic Diagram of Scintillation Tile

connected to a PMT of 1.5 inch diameter. The length of the fiber between the tile and the PMT is 75 cm. More detail is found in Reference [52].

Similar to the SiMA, the TMA provides a measure of the number of particles that traverse each element. However, in this case, photons are emitted with the passage of the charged particles, as described further below. Also, the TMA provides the level 1 centrality trigger for the experiment taking advantage of the good time response of the detector element. This capability is not used, however, in the current analysis.

4.2.1 General Properties for Scintillation Detector

As charged particles pass through a scintillation detector, they lose energy according to the Bethe-Block Equation 4.1. Unlike semiconductor devices, which create electrons and holes by the passage of charged particles, scintillator devices result in photons being emitted as the charged particles traverse the element. The radiation from passing particles excites free valence electrons of molecules, which are occupying π molecular orbitals [53, 54]. Figure 4.17 shows the energy level diagram of typical scintillator material. In the case of electrons in the singlet

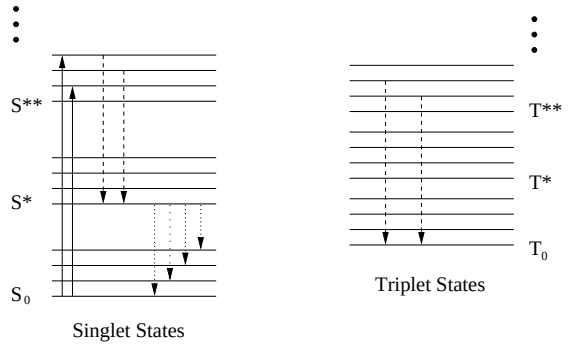

Figure 4.17: Energy Level Diagram of typical Scintillation Material
Thick and thin lines represents electron and their vibrational levels respectively. The dashed line is internal degradation. The dotted line represents fluorescence radiation.

states, electrons first decay to S* states by internal degradation and do not produce photons. However, from the S* states, there is a subsequent decay to the ground state S_0 or its vibrational states, where light is emitted. When electrons are in excited triplet states, they decay to the triplet ground state T_0 by internal degradation. Then, rather than decaying to the singlet state, which is highly prohibited by the selection rule of dipole transition, electrons interact with other

electrons in the triplet ground state through a process of

$$T_0 + T_0 \rightarrow S^* + S_0 + \text{phonons} \quad . \tag{4.39}$$

The electron in the S^* state subsequently decays to the ground state by fluorescence radiation.

4.2.2 Photomultiplier Tubes

A photomultiplier tube (PMT) is a device that converts a light signal to an electrical signal. It is designed such that the amount of charge or current produced in a PMT is proportional to the number of photons entering the PMT. The basic diagram of a PMT is shown in Figure 4.18. At first, photons entering a PMT will hit a photo cathode, which produces electrons by

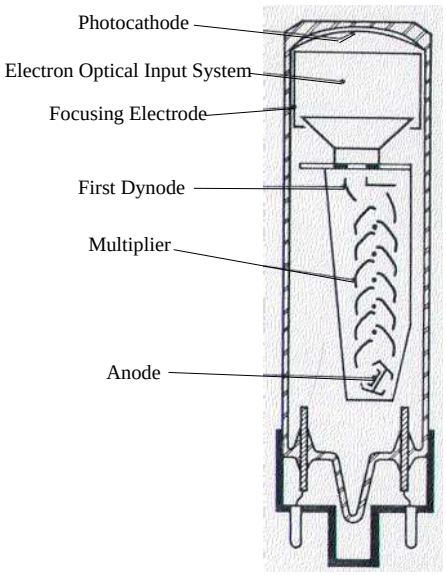

Figure 4.18: Schematic Diagram of Photomultiplier Tube
Copied from Reference [53].

the photoelectric effect. A typical photo cathode has a quantum efficiency of between 10% and 30%, which means that it will create 1 to 3 electrons with 10 initial photons. Electrons are then guided toward the first dynode by focusing electrodes. The first dynode creates more electrons by the energy applied from the incoming electrons. The resulting electrons then accelerate to the next dynode. This process is repeated 10 to 14 times until the last stage, where electrons are collected at an anode. During this process, the number of electrons can be amplified by a

factor of 10^3 to 10^7, depending on the type of tube and the applied voltage.

4.2.3 Data Acquisition

Figure 4.19 shows the basic diagram of the data acquisition system for the TMA. It is very

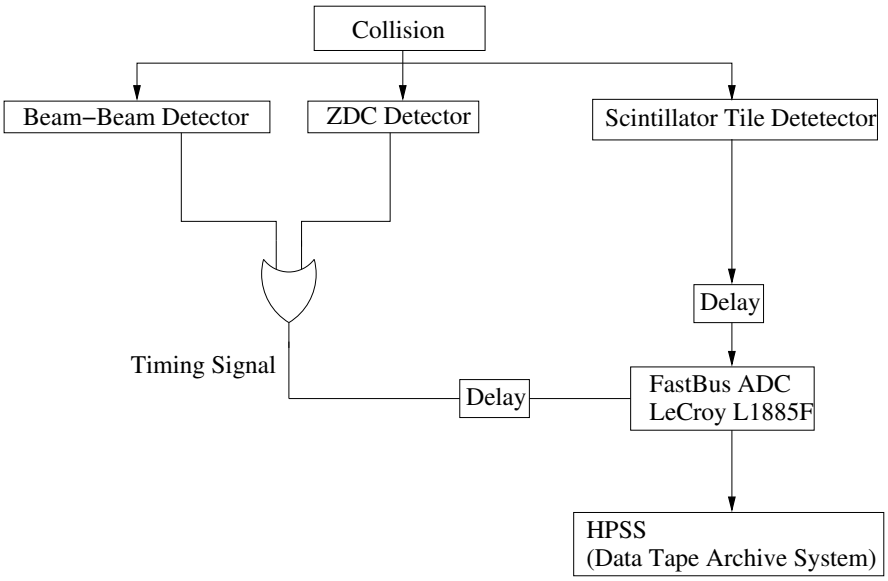

Figure 4.19: Data Acquisition Diagram for Scintillation Tile Detector

similar to that of the SiMA except that an additional delay is introduced in the signal path to allow synchronization of the relatively fast TMA signals with the timing signal obtained with the BBC and the ZDC detectors. The delayed signal is fed directly into a FastBus ADC with the resulting data stored in the HPSS system.

4.3 Beam-Beam Counter Arrays

The Beam-Beam Counter arrays (BBC), which are shown in Figure 3.4, are located 2.1 m to the left and to the right side of the nominal vertex location along the beam axis. The left array consists of 44 Cherenkov radiators which are coupled with PMTs. They are grouped into 5 sets of elements by their distances from the beam axis. The right array consists of 35 radiator-PMT pairs. They are grouped into 7 sets, also by their distances from the beam axis. A more detailed discussion of the detector configuration is found in Reference [55, 49]. In the analysis of charged particle multiplicity, the BBC arrays offer a measurement of the number of charged particles at

large pseudorapidity, outside of the acceptance by the SiMA and the TMA.

4.3.1 General Properties of Cerenkov Detector

The Beam-Beam counters are basically a set of simple Cherenkov detectors. When a particle traverses the radiator material at a speed above the speed of light in that material, it loses energy by creating an electromagnetic shock wave, similar to the sonic shock wave produced by a super-sonic jet plane when it travels faster than the speed of sound in air. The condition for creating this radiation is expressed as

$$v > \frac{c}{n} \tag{4.40}$$

where c is the speed of light, n is the index of refraction of the material and v is the velocity of the particle. The coherent wave has a conical shape with an angle of

$$\cos\theta = \frac{1}{\beta n\left(\omega\right)} \quad , \tag{4.41}$$

where β is v/c, and $n\left(\omega\right)$ is the frequency dependent index of refraction.

One of the most important properties in designing a Cherenkov detector is the number of photons produced in the radiator. For a particle of charge ze, this can be written in terms of the wavelength, λ, as

$$\frac{d^2N}{d\lambda dx} = \frac{2\pi z^2 \alpha_e}{\lambda^2}\left(1 - \frac{1}{\beta^2 n^2\left(\lambda\right)}\right) \quad , \tag{4.42}$$

where α_e is the fine structure constant. Integrating Equation 4.42 over the wavelength acceptance of the coupled PMT, the number of photons produced in the radiator for which the PMT will be sensitive can be estimated. The signal from the photons is amplified with the PMT as discussed in Section 4.2.2.

4.3.2 Data Acquisition for the Beam-Beam Counter Arrays

Figure 4.20 shows the basic diagram of the data acquisition system for the Beam-Beam Counter arrays. Each PMT for the BBC has two outputs. One is used to identify the occurrence of a collision. This signal is fed into the logic system to produce the timing signal for all detectors. The other signal is fed into the FastBus ADC after delay and recorded into the HPSS data archive system. This digitized analog signal is used for the analysis of the charged particle

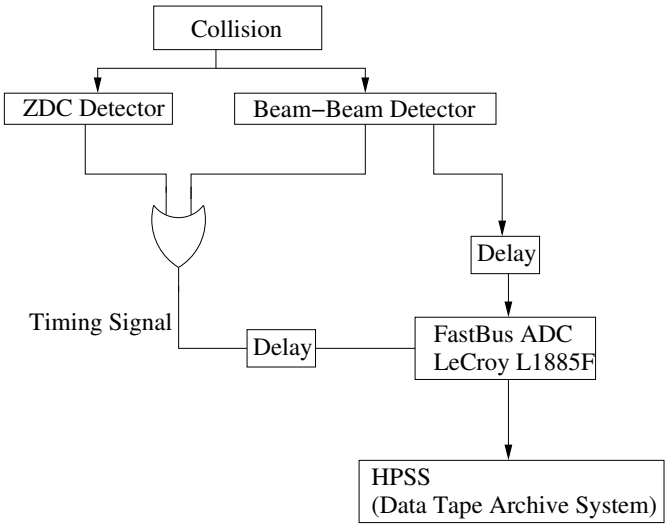

Figure 4.20: Data Acquisition Diagram for Beam-Beam Counter

multiplicity at large pseudorapidity.

Chapter 5

Vertex Determination

Since the RHIC experiment is not a fixed target experiment, it is necessary to determine the vertex location for each collision event. The Zero Degree Calorimeters (ZDC), which have close to 100% efficiency for detecting a collision event, are used to determine the vertex position for minimum bias events. These detectors lead to a vertex resolution of 2.0 cm in the direction of the beam axis. The Beam-Beam Counter arrays (BBC), which have an efficiency of 85%, are also used to find the vertex location and have a resolution of 9 mm. In addition, the TPM1 time projection chamber can be used to provide a very accurate vertex location with a resolution of 3 mm, although this chamber has a limited overall efficiency of 30%.

5.1 Methods for Finding the Vertex Position

The ZDC and BBC detectors employ the same technique for finding the collision vertex. The difference in arrival times for particle hitting the left and the right detectors along the beam axis is measured. Figure 5.1 shows the basic diagram for locating the collision vertex. The change in the location of the vertex is reflected in a change in the time of flight measured to the left and the right detectors. When collisions occur at the midpoint between two detectors (the nominal vertex location), the flight times measured by the left and right detectors are the same. Whereas collisions that occur to the left of the nominal vertex location results in a shorter flight time to the left detector than to the right detector. Assuming the particles that hit the detectors are highly relativistic so that their velocity is approximately the speed of light, the vertex location

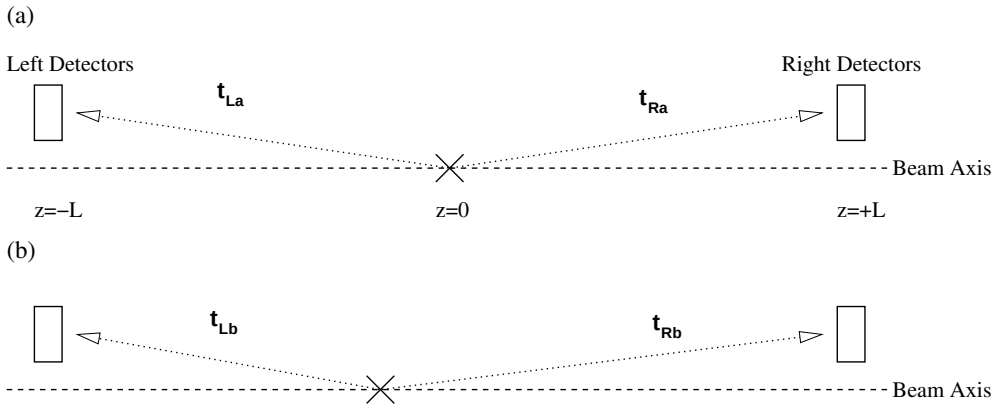

Figure 5.1: Diagram of Vertex Location

can be written as

$$z_{vertex} = \frac{c}{2}\left(t_L - t_R\right) \tag{5.1}$$

where

$$\begin{aligned} c &= \text{the speed of light} \quad , \\ t_L &= \text{the flight time to the left detector} \quad , \text{ and} \\ t_R &= \text{the flight time to the right detector} \quad . \end{aligned}$$

In the experiment, this equation must be modified to use the experimentally measurable variables. The method used to determine the difference in the two flight times is shown in Figure 5.2. A coincidence unit checks whether two signals arrive within a time consistent with the occurrence of a collision. This coincidence is necessary to establish that both detected signals from the left and right detectors come from the same collision. The output of the coincidence unit is used as a start signal for a multichannel Time-to-Digital Converter (TDC). The signals from the two detectors, suitably delayed, are used as stop signals for the TDC.

The TPM1 detector can also be used to measure the vertex location of selected events. It does so by extrapolating the track measured inside TPM1 to the plane defined by the beam axis and the vertical axis. Figure 5.3 shows the diagram for the TPM1 vertex finding method. As particles traverse the chamber volume, the counter gas is ionized along the path of the track. Liberated electrons are detected as a "cluster" in TPM1. By connecting different clusters by

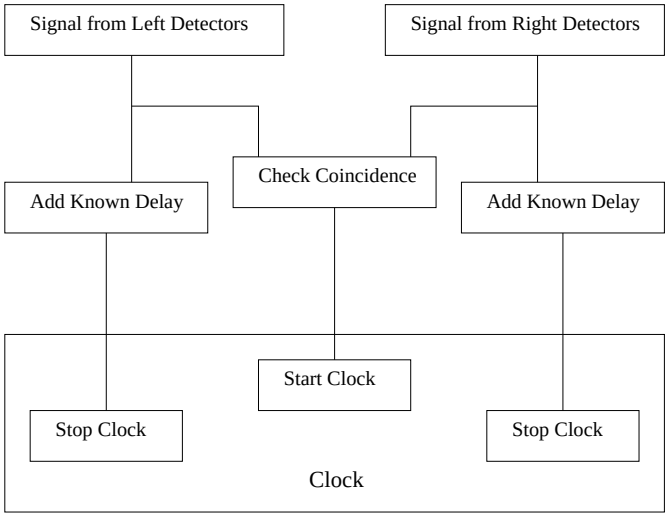

Figure 5.2: Diagram for Vertex Clock

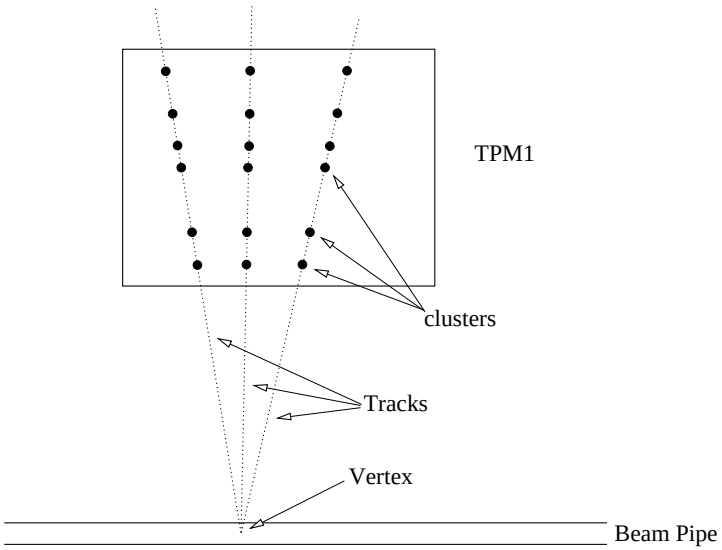

Figure 5.3: Diagram for TPM1 Vertex Finding

straight lines, the track of the passing particle can be reconstructed. It is then possible to find the collision vertex by extrapolating several tracks to the beam axis. This method clearly requires at least two good tracks, and hopefully more. BRAHMS also use a second method of finding the vertex by TPM1. It is called the "Cluster Vertex" method and works by creating lines matching every combination of cluster pairs and extending these lines to the beam axis. The real vertex shows up as a pronounced peak on top of a background of false vertex positions. A more detailed discussion of the TPM1 vertex methods can be found in Reference [48].

5.2 Vertex Resolution

The three methods of locating the collision vertex (using the ZDC detectors, the BBC arrays and the TPM1 detector, respectively) differ considerably in their respective precisions. All three methods are necessary, however, since the efficiency of locating a vertex for the three methods are quite different. For TPM1, the resolution of vertex position depends primarily on the uncertainty in locating the TPM1 detector. The observed vertex resolution for TPM1 is about 3 mm. Both the ZDC and BBC vertex determinations are done by measuring the flight time of the particles hitting these detectors. Consequently, the timing resolutions of the detectors dominate the vertex resolution. These timing resolutions are intrinsic to the design and construction of the detectors. One way to optimize the timing resolution is to apply a "Slewing Correction" to the data. This correction tries to compensate for variations in timing caused by the different amplitudes of the detector signals. Timing information is obtained by using leading-edge discriminators on these signals to pick off the instant when the signal goes above a preset threshold. Figure 5.4 depicts this case in a simple diagram. In this figure, there are two negative pulses of different sizes with equal peaking time, that is, the time it takes for a pulse to reach its maximum (or minimum if it is a negative pulse) value. For many types of detectors, the peaking time tends to remain constant for different pulse sizes. As illustrated in the figure for a given discriminator level, the time difference between signal onset and when the signal reaches the discriminatory level depends on the signal amplitude. The larger the size of a pulse, the earlier the time signal is generated.

In the experiment, this variation of timing by pulse size is easily seen by plotting measured time minus a reference time against pulse height. The reference time is typically obtained by

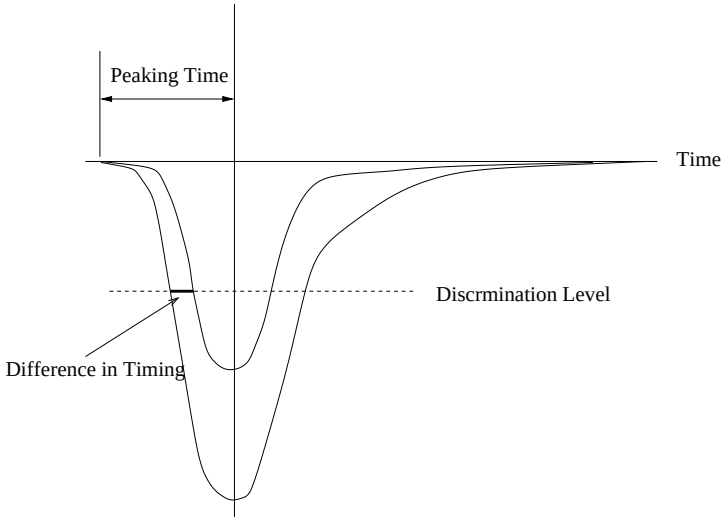

Figure 5.4: Cause for Slewing

selecting signals in a limited amplitude range from a second detector. The typical slewing figure for a BBC detector is shown in Figure 5.5. Figure 5.5a shows the dependence on pulse size of the timing. This causes widening of the timing resolution. The corrected timing has the following form from its shape:

$$TDC_{corrected} = TDC_{raw} - \frac{a}{\sqrt{ADC}} - \frac{b}{ADC} \quad , \tag{5.2}$$

where a and b are parameters to be determined from Figure 5.5a. With the slewing correction, the dependence on pulse height is minimized. The typical resolution is about 150 ps before the slewing correction and 60 ps after the correction. Greater detail regarding the BBC slewing correction can be found in Reference [55]. The ZDC detectors are analyzed in the same manner and have their own set of slewing corrections.

Despite the slewing correction to reduce the dependence on pulse size, the vertex determined by the BBC and ZDC detectors still show some sensitivity to pulse height. Figure 5.6 shows this tendency by plotting deduced vertices vs. the sum of ADC channels for the TMA detectors. The two profile plots (Figure 5.6b and d, which plot mean values of Figure 5.6a and c along the y axis) clearly show this trend. This residual correction is probably due to limitations of the slewing corrections and it might suggest that the functional form given in Equation 5.2 is not fully adequate. After the slewing correction described above, the BBC counters show up

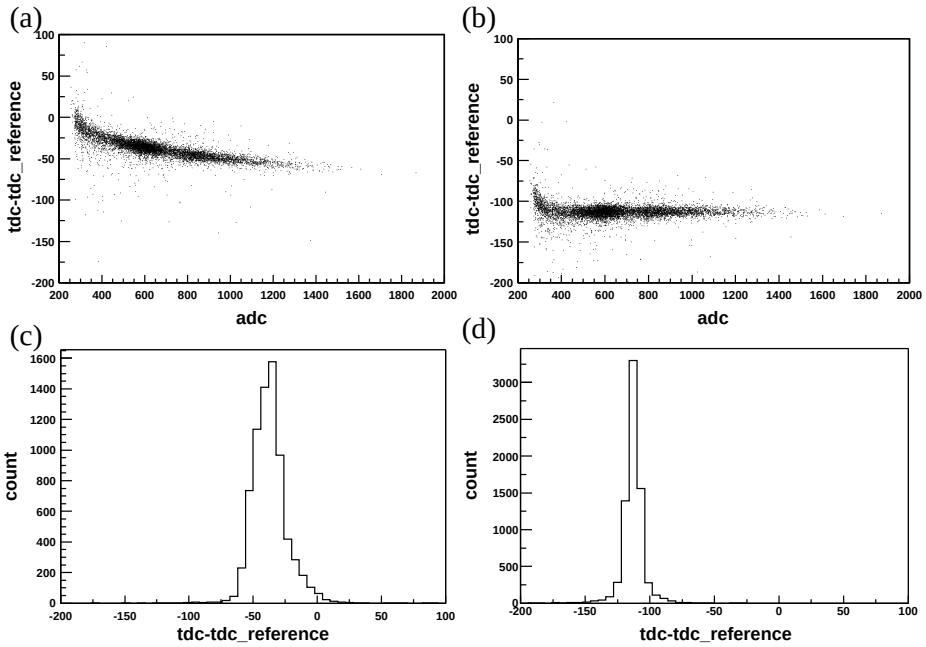

Figure 5.5: Slewing for the BBC arrays
(a) and (c) shows before slewing correction. (b) and (d) shows after slewing correction. (a) and (b), (c) and (d) use the same bin sizes for their histograms to easily compare two cases.

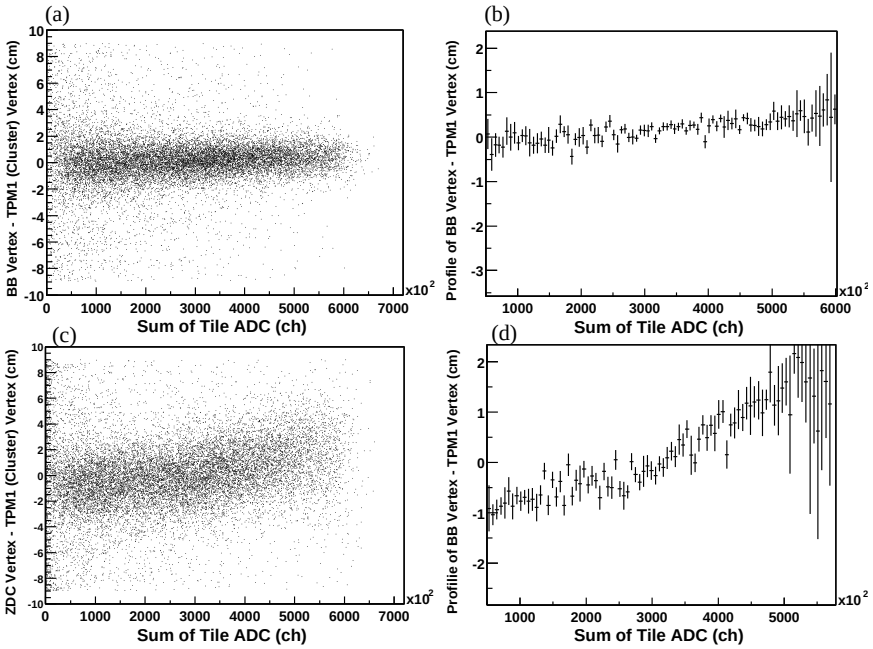

Figure 5.6: Dependence of vertex location to signal size after slewing correction
(a) and (c) show the 2 dimensional histograms of deduced vertex location (the BBC and ZDC detectors, respectively) vs. the sum of ADC channels for the TMA detectors. (b) and (d) show the profile plots of (a) and (c), respectively.

to 5mm vertex shifts with the tile ADC sum, and the ZDC detectors show about 2.0 cm shifts. Since multiplicity measurements done by the SiMA detectors are sensitive to vertex shifts in the order of 3 to 4 mm, it is essential to correct for this behavior. Otherwise, the measured multiplicity would be asymmetric about the center of mass of a system with a symmetric mass entrance channel. To remedy this situation, an empirical correction factor is introduced. This factor is obtained by fitting a straight line to the profile plots of Figure 5.6 for the BBC and ZDC detectors. Figure 5.7 shows the vertex resolution of the BBC and ZDC detectors after this correction. The vertex resolution obtained using the BBC detectors is about 9 mm, and that

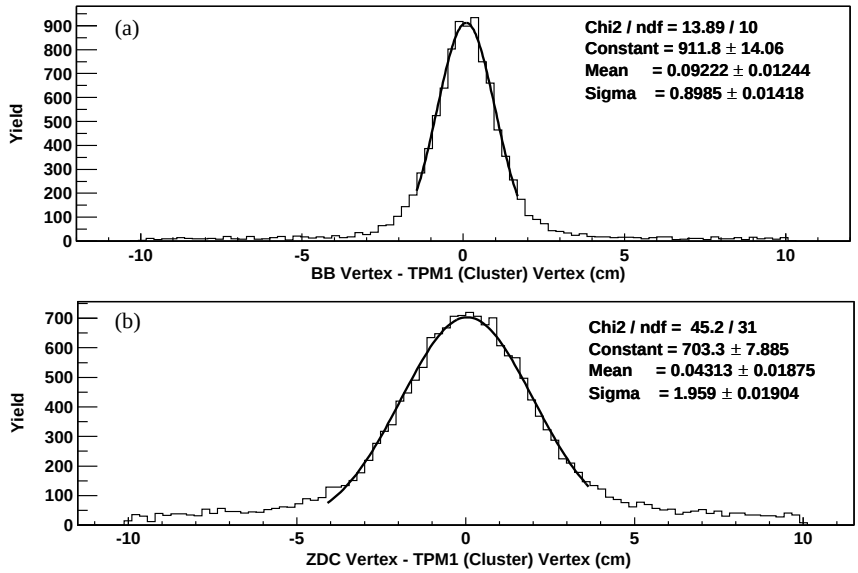

Figure 5.7: Vertex Resolution
(a) and (b) shows the vertex resolution of the BBC and ZDC detectors, respectively.

using the ZDC detectors is about 2.0 cm.

5.3 Vertex Efficiency

As stated earlier, there are three different methods for finding a collision vertex for a given event. Not only does each method result in quite different position resolutions, but they also have very different efficiencies for finding a vertex. Figure 5.8 shows the efficiencies for finding a vertex for the three different methods. The TPM1 detector, which has the best vertex resolution, is the least efficient. Its yield as a function of the charged particle multiplicity is shown by the shaded

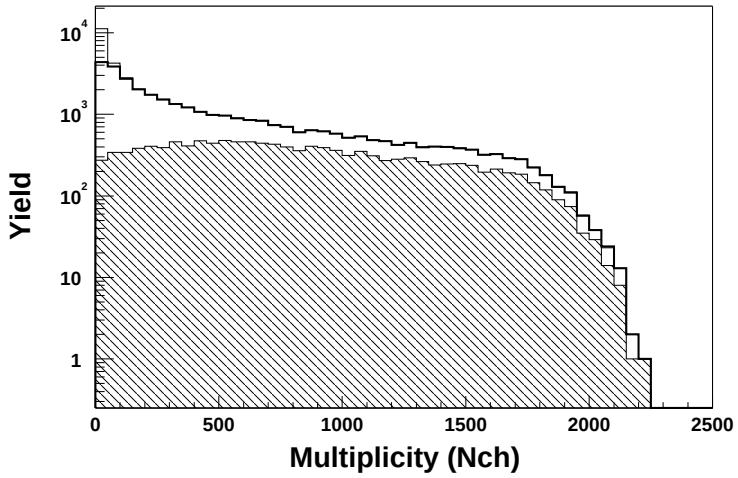

Figure 5.8: Vertex Efficiency
Shaded area represents the events determined by TPM1 cluster vertex method. Area enclosed by the dark line represents the events determined by BBC vertex method. The area enclosed by the thin line represents the ZDC detector.

region of the figure. Its efficiency ranges from about 70% for very central, high multiplicity events to 2% for very peripheral, low multiplicity events with a 30 % overall efficiency. The yield vs. multiplicity behavior of the BBC detectors is shown as the region enclosed by the darker line in the figure. Its efficiency ranges from 100% for the central events to 38% for peripheral events with the overall efficiency of 85%. The ZDC detector is used as the minimum bias detector for finding a vertex, and it is represented as a area enclosed by the thin line in the figure. The difference of the yields between the BBC and ZDC detectors is particularly noticeable for the low multiplicity event. Hence, the ZDC detector is primarily used to find vertices for the most peripheral collisions.

5.4 Choice of Vertex Methods

With three different methods for finding the interaction vertex, a choice has to be made to select the best vertex for a given collision. In general, the vertex method giving the best resolution is chosen. A summary of performance for the three vertex methods is shown in Table 5.1. From the table, it is clear that TPM1 has the best resolution for finding an event vertex. Hence, this vertex is used if available. However, because of the relatively low TPM1 efficiency, the other methods are also used. When the TPM1 detector fails to find a vertex, the BBC detector vertex

Table 5.1: Summary of Vertex Methods

Methods	TPM1	BB	ZDC
Resolution	3.0 mm	0.9 cm	2.0 cm
Overall Efficiency	30 %	85 %	~100 %
Efficiency for Central Collisions	70 %	100%	~100%
Efficiency for Peripheral Collisions	2 %	40 %	~100%

is chosen. If the BBC detectors further fail to find a vertex, as is often the case for peripheral collisions, the ZDC vertex is used.

Chapter 6

Multiplicity Detector Calibration

The global detectors are not track-counting detectors. It is thus necessary to calibrate these detectors to measure charged particle multiplicity. The SiMA and TMA detectors sense the passage of charged particles by the energy deposited by these particles in the sensitive volumes according to Equation 4.1. The BBC arrays rely on the detection of Cherenkov lights produced by the passages of charge particles in the associated Cherenkov radiators. Since the global detectors do not sense the direction of the detected particle's trajectory, it is crucial to determine the backgrounds in each detector system. This amounts to a correction for the amount of energy or light produced by particles that do not originate from the main collision vertex. These secondary particles emerge from supporting structures by inelastic collisions of primary particles with these structures. Because of the very large number of primary particles produced in a single collision, the number of secondary particles is also large despite extensive efforts to use thin and light-weight materials for the supporting structures.

6.1 Silicon Strip Detector Multiplicity Array (SiMA)

6.1.1 Linearity of the Preamplifier-Shaper Electronics

Any detector non-linearities can have a large effect on the resulting multiplicities since such a nonlinearity will skew the results if not corrected. It is, therefore, necessary to check the linearity of the different detector system before any measurements. The linearity of the pre-amplifier-

shaper electronics for the SiMA detectors has been checked by the use of an electronic pulse generator (pulser). The pulser injects a pulse of a desired size to the input of the charge-sensitive pre-amplifier. After the signal is amplified by the electronics, the size of the output pulse can be checked by an oscilloscope. Using this procedure, the pre-amplifier-shaper electronics has been determined to be linear within the precision of the measurement.

6.1.2 PTQ Calibration

The PTQ is a peak stretcher. It will hold the peak value of a signal for a specified period of time as determined by a reset signal. Figure 6.1 shows the diagram of this case. It is necessary

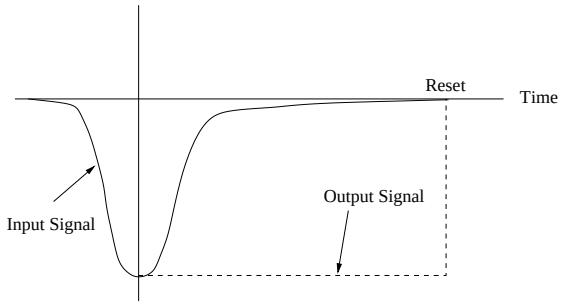

Figure 6.1: Peak Stretcher (PTQ)

to introduce this electronics because the duration of a signal from a silicon strip detector is too long to be directly integrated by the charge-sensitive ADCs used in the experiment. Using the PTQ with a fixed-length ADC gate, the signal integrated over the duration of the gate will be proportional to the signal amplitude. The PTQ-ADC arrangement results in a measurement similar to that of a peak-sensing ADC. However, during final testing of the electronics, it was noticed that the PTQ has a nonlinear response for low-amplitude signals. Figure 6.2 shows the response of a PTQ with different sizes of input pulses. For larger amplitude signals, as shown in Figure 6.2a, the measured ADC value seems to be fairly linear. However, focusing on the low amplitude signals as shown in Figure 6.2b, a strongly nonlinear response is apparent for signals smaller than 1000 mV. Since the electronics was designed to put the signal from a minimum ionizing particle in this range, it was important to correct for this nonlinear behavior. In Figure 6.2, the solid lines show fits to the data, which are used to correct for the PTQ non-linearity.

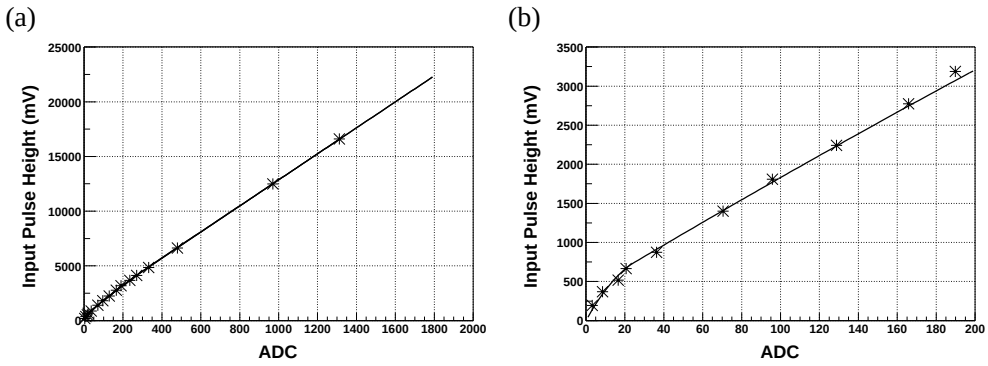

Figure 6.2: PTQ Linearity
(a) shows whole range of PTQ response. (b) shows the range for small input pulse. The dark line indicates the fit to this curves, which is used to correct the non-linearity of PTQ.

All PTQ channels are calibrated individually in this manner.

6.1.3 Energy Calibration

A silicon strip detector detects the passage of particles by sensing electrons and holes produced in the depletion zone of the detector. As particles travel through the detector, they lose energy by knocking electrons out of the crystal lattice, with the output signal then being proportional to the energy loss of the particles passing through the detector. Since this detected signal is used to calculate the number of particles passing through the detector, the calibration of detected pulse size to corresponding energy loss is crucial. This calibration is done using the same data as used for the multiplicity analysis.

It is easily realized that for a given silicon strip of the detector, the distance that a particle travels inside the strip depends on the location of the vertex. Figure 6.3 illustrates this point. Particle 'a', which is incident normal to the detector face, has the shortest possible travel distance within the detector. Particle 'b', which is incident at an angle θ with respect to the plane of the detector surface, has a travel distance within the detector given by

$$\text{travel distance} = \frac{L}{\sin\theta} \tag{6.1}$$

where L is the thickness of the strip. Since the differential energy loss is approximately constant for a particle passing through the detector, the total energy loss is proportional to the distance traveled through the detector. This effect is directly visible from the data. Figure 6.4 shows

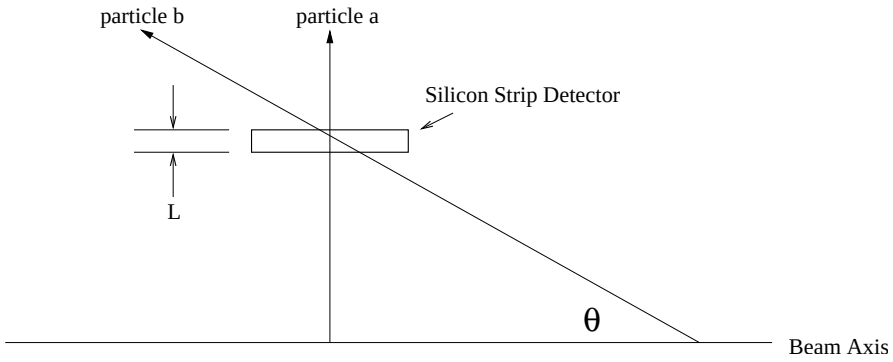

Figure 6.3: Travel Distance of a Particle in a Detector

plots of the detected pulse height (ADC value) of one strip as a function of vertex location. The left figure includes all events. The 'v' shaped line corresponds to single particles traversing

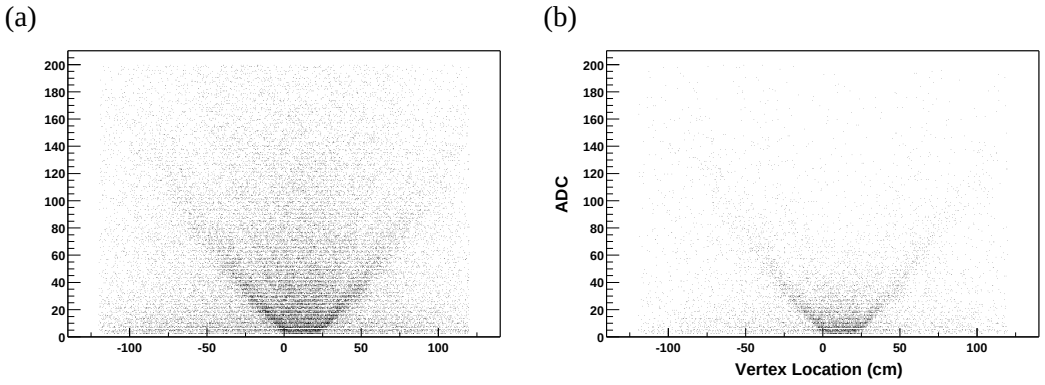

Figure 6.4: Si ADC vs Vertex Location
(a) is without any conditions and (b) is with low multiplicities conditions.

the detector element. The large "background" results from events with more than one particle hitting this strip. To reduce the effect of multiple-particle hits, the condition that only low (total) multiplicity events are selected can be used. By reducing the total multiplicities, the chance of multi-particle hits in a given strip is also reduced. This is shown in Figure 6.4b. Now, the 'v' shaped curve is very clear. This observed response for single particle events can be used to calibrate the detectors and associated electronics.

By projecting Figure 6.4 onto the y-axis within a small region of vertices, the detector response for single-particle hits can be represented as a peak in a one-dimensional histogram. Since this peak represents the energy loss of a particle in the detector, the location of the peak depends on the type and momentum as well as the travel distance of the particle passing through

the detector. Since the type and momentum of the passing particle is not known, one cannot use Equation 4.1 to determine the expected energy of this peak. Rather, the peak is compared with the results from GEANT Monte Carlo simulations to obtain the corresponding energy loss. (The reliance on the GEANT simulation for the energy calibrations does not cause a large uncertainty for the charged-particle multiplicity measurement since the subsequent conversion from energy loss of particles in the detectors to the number of charged particles is also based on the same GEANT simulations, as discussed in the next section. Hence, the GEANT simulation does not provide an absolute energy calibration but rather leads to a relative calibration of energy loss of the charged particles passing through the detectors.) The GEANT simulation has the added advantage of also simulating the background contribution to the energy spectra. Figure 6.5 shows the process for energy calibration of the SiMA detectors. The response of one particle

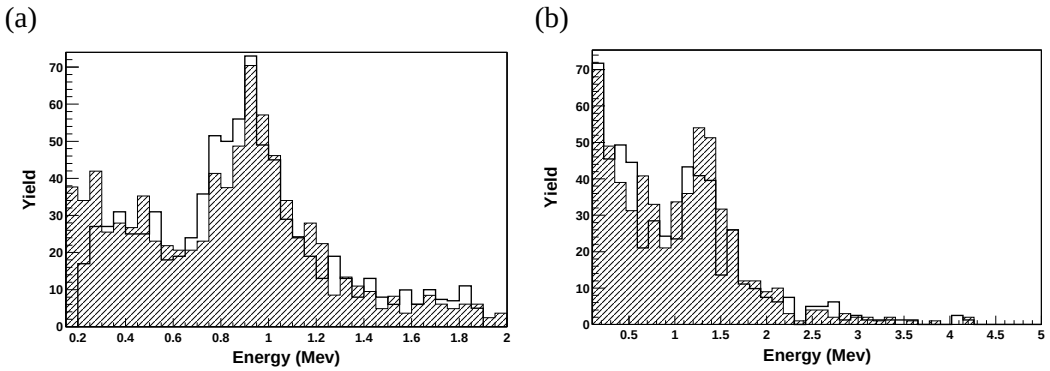

Figure 6.5: Energy Calibration for Silicon Detector
The area enclosed by the thick line represents the data. The shaded area represents GEANT simulation. (a) is with vertex located at 60 cm right of the nominal vertex location, and (b) is with vertex located at 60 cm left of the nominal vertex locatioin.

is visible and well defined. The GEANT package reproduces the backgrounds under the single charged-particle peaks quite well. Repeating this process for many different locations of vertices for a given silicon strip, the pulse height to the corresponding energy-loss value is obtained. In the calibration, the systematic error is estimated to be 6%.

6.1.4 Multiplicity Calibration with Background

Once the energy loss of particles passing through the detector elements is known, it is possible to obtain the corresponding number of charged particles with a conversion function. The conversion function used for the SiMA detectors must account for particles striking the detector elements

with varying momentum. Figure 6.6 shows the momentum distribution of particles hitting the SiMA detectors based on GEANT simulation using the Hijing event generator. It is clear that

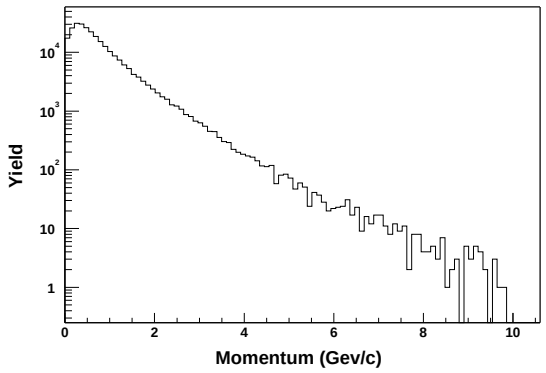

Figure 6.6: GEANT Simulated Momentum Distribution of Particles Hitting Silicon Strip Detector by Hijing Model

the SiMA detectors receive particles with a large distribution of momenta. The mean value of this distribution is about 0.75 GeV/c. By assuming that the majority of particles are pions, one finds that most of the particles have momenta equal to or greater than that of a minimum ionized particles. They, therefore, deposit almost the same amount of energy. However, the particles with low momentum are of concern since they can have very large energy loss in the detector and can thereby skew the results.

The conversion function from the energy loss in the SiMA detector element to the corrresponding number of charged particles is also required to account for the many different types of particles striking the detectors. Figure 6.7 shows the simulated yields of particles striking a typical SiMA detector based on the GEANT simulation using the Hijing event generator. It is clear that π^+ and π^- particles dominate the yield. Although this is a model dependent result, it is safely assumed that the majority of particles are pions. Furthermore, for different particles of the same charge, the minimum stopping power is about the same. This is clearly seen in Figure 4.3. Therefore, with the assumption that most of particles are minimum ionizing, it can be assumed that most of the particles deposit approximately the same energy, except for the small number of particles of low momentum.

Finally, the conversion function must be able to remove the background signals since the SiMA detector will accept particles incident from any direction. This is a significant complication since not all particles hitting the detector are from the collision vertex. Particles can be

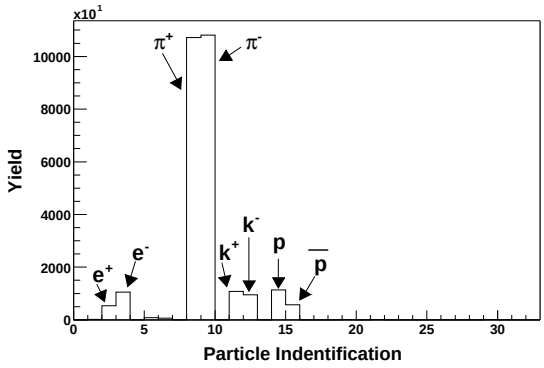

Figure 6.7: Types of Particles Hitting Silicon Strip Detectors by GEANT Simulation with Hijing Model

created by the interaction of primary (or original) particles with the material of the supporting structures, or the material of the detector itself. Considering that there are thousands of primary particles emerging from a single Au-Au collision, there can be a multitude of secondary particles. For the SiMA detectors, the GEANT simulations indicate that between 5% and 10 % of detected energy is associated with the secondary particles, depending on the detector and vertex positions. In the multiplicity measurement, a correction factor based on GEANT simulation is applied to account for these effects.

From the above description of the SiMA detectors, it is clear that to measure the particle multiplicity of an event, it is necessary to use some averaged, expected values to convert the detected energy signal to the number of particles. This is essential since multiple particles may pass through a single silicon strip in a given event. For the most central events, the average number of particles striking a single strip of silicon can be greater than ten. There are a couple different ways to map from detector signal to charged-particle multiplicity. One way would be to use the response of the minimum ionizing particle (ADC_{MIP}) shown in Figure 6.4 and to divide the measured ADC value by ADC_{MIP} for a given vertex location. The deduced multiplicity can then be corrected for secondary particles by applying the 5% to 10% correction found using the GEANT simulations. However, this method has the problem that the single MIP peak is unresolved from the pedestal peak when the vertex is within 20 cm from the location of the strip along the beam axis. Under these conditions of near-normal incidence of the particle onto the silicon strip, the energy loss of the particle is minimized. Through electronic noise and the nonlinearity of the PTQs, as discussed in Section 6.1.2, the resolution of the detector is at its

worst, preventing single MIP resolution. Also, this method may not adequately account for low momentum particles. Therefore, it was decided to make an all inclusive conversion function to map from the detected energy to the number of primary particles.

Figure 6.8 shows the result of the GEANT simulation used to produce this conversion function. The definition of N_{ch} is defined as particles emerging from the region within 3 cm of

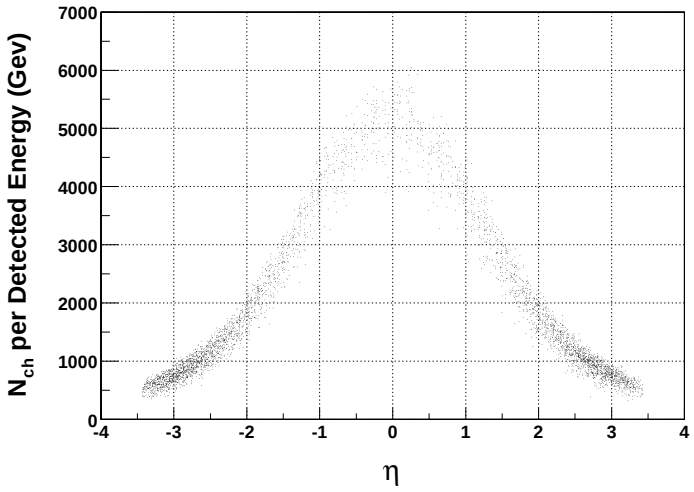

Figure 6.8: Silicon Energy to N_{ch}

the collision vertex. There are two reasons for this definition of the primary particles. One is to include the short-lived resonances as primary particles. Also, this definition excludes many particles produced from the beam pipe which has a radius of 3.81 cm. Figure 6.9 demonstrates this clearly by showing the origins of all particles that strike the SiMA detectors in the GEANT simulation. It is clearly seen that the beam pipe is one major source of secondary particles. The other sources include silicon strips and scintillator tiles as well as the supporting structures.

To test the conversion function shown in Figure 6.8, the charged-particle distribution deduced from the simulated energy loss in a model array was compared to the "known" results. Figure 6.10 shows the result. The "data" with open-circle markers represent the values from the HIJING model used as input to the GEANT simulations. They are the expected values for this test. The closed-circle markers represent values obtained through the above analysis, using the conversion function shown in Figure 6.8. It is clearly seen that the conversion function accurately reproduces the expected values of the particle production. This test was also conducted with other model inputs to evaluate the model dependence. The results indicated that the model dependency was

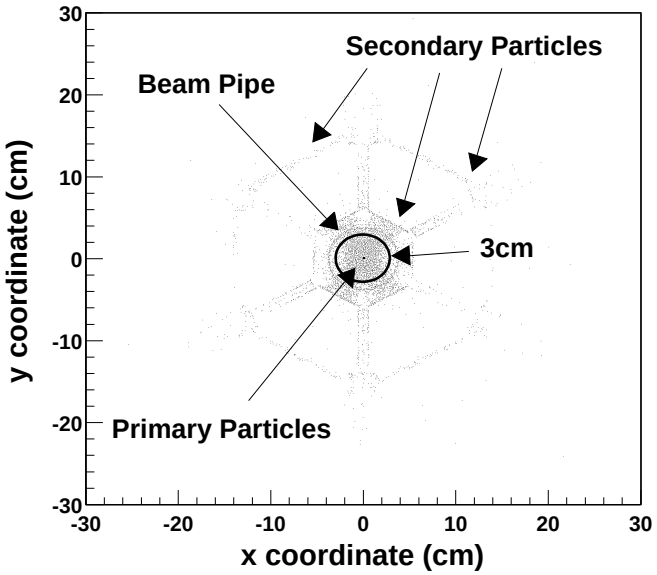

Figure 6.9: Definition of Primary Particles by GEANT Monte Carlo Simulation

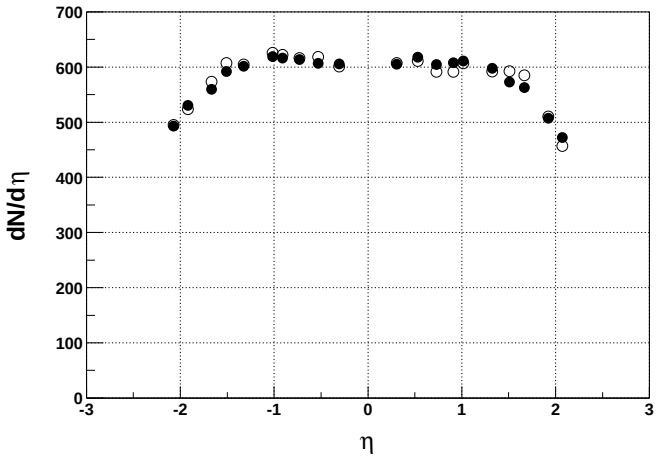

Figure 6.10: Comparison of Particle Productions in the GEANT simulation with the HIJING Model
The open circle is obtained from the using the conversion function of Figure 6.8. The close circle is HIJING Model.

less than a few percent of the charged particle production.

6.2 Scintillation Tile Detector Multiplicity Array (TMA)

The calibration method used for the TMA detectors is quite similar to that of the SiMA detectors due to the similar energy-loss characteristics as well as the similar configuration of the detectors. The major difference in SiMA and TMA is that the TMA detectors use phototubes whose output signals can be fed directly into charge-sensitive ADCs, without requiring an intermediate PTQ. They are therefore free of the PTQ nonlinearity.

6.2.1 Linearity of Photomultiplier Tubes

For the TMA detectors, the overall linearity of the detector response is the major concern for determining the event multiplicity. This is, perhaps, even more a concern for these detectors since the extrapolation from the single MIP events to the more central Au+Au collision events is much greater than necessary for the SiMA. For the most central collisions, the number of particles hitting a single tile can be above 100, whereas the maximum number for a single silicon strip is close to 10. Since the energy calibration is determined by the response of one particle, the extrapolation by 100 folds could yields large errors if the linearity of the detector is not well understood.

The linearity of the photomultiplier tubes was tested using the setup shown in Figure 6.11. In this setup, the photomultiplier tube is placed in the light-tight box with a isotropic light source [52]. The light source is mounted in the rail which is controlled by a stepping motor. The amount of light entering the PMT is controlled by the distance between the PMT and the light source. By measuring the output pulse size from the PMT, the linearity of the PMT were checked. In this test, the PMTs for the TMA detectors exhibit good linearity.

6.2.2 Energy Calibration

The energy calibrations of the TMA detectors were done using the single-particle response of each tile, similar to how the SiMA detectors were calibrated. Figure 6.12 shows the typical raw detector response of a single scintillator tile. In Figure 6.12a, the single-particle response is faintly visible within a large background. The large background is expected since the size

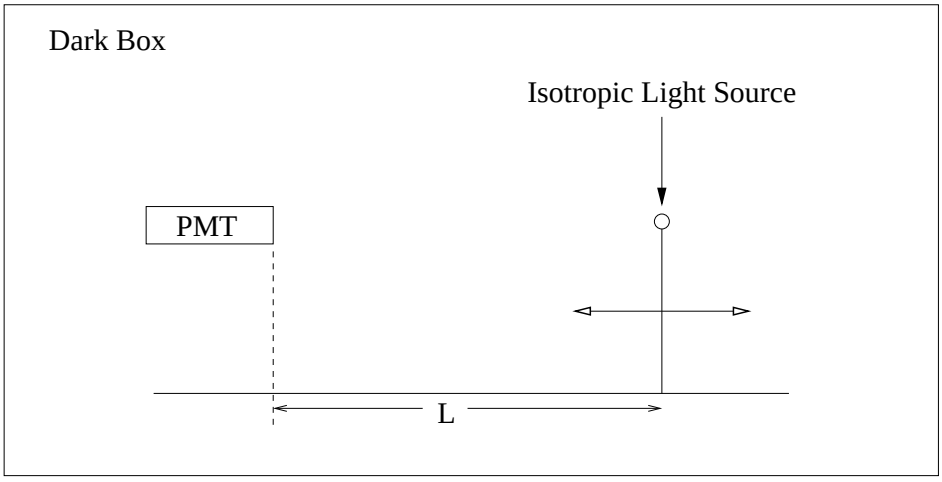

Figure 6.11: Linearity test setup for PMTs used in the Scintillation Tile Detector

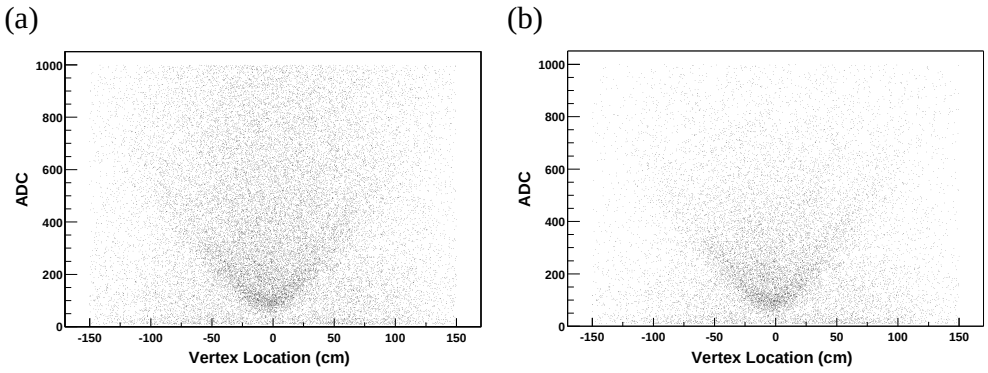

Figure 6.12: Si ADC vs Vertex Location
(a) is without any conditions and (b) is with low multiplicities conditions.

of each tile element is much larger than a single silicon strip element and, consequently, most events lead to multiple particles passing through any given tile element. By selecting low total multiplicity events, as shown in Figure 6.12b, a clean "v-shaped" response is observed.

Using the technique discussed in Section 6.1, the above detector response from the data is used to calibrate each tile. Figure 6.13 shows the experimental one particle response of a single tile with the corresponding GEANT simulation. It is clearly seen that the GEANT simulates the

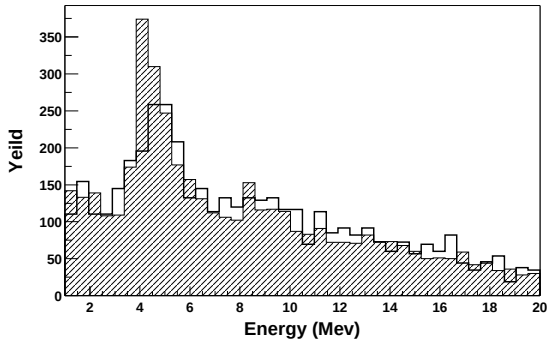

Figure 6.13: Energy Calibration for Scintillation Tile Detector
The area enclosed by the thick line represents the data. The shaded area represents GEANT simulation.

detector response well, including the background. By comparing the experimental and simulated one particle response, an energy calibration is obtained for each tile element. In the calibration, the systematic error is estimated to be 10%.

6.2.3 Multiplicity Calibration with Background

As found for the SiMA, once the energy calibrations are known for the tile elements, it is still necessary to use model-dependent conversion functions to obtain the corresponding charged-particle multiplicities. However, unlike the common conversion function that was found adequate for the SiMA elements, there are eight functions needed for the TMA elements, one for each tile "ring", because of the relatively large background in the TMA elements. In a single silicon strip, only 5% to 10% of the detected energy originates from the secondary particles, whereas, in one tile, 30% to 40% of the detected energy is from secondary particles. Since the amount of the background reflects the configuration and location of the tile, it was determined that eight conversion functions were necessary, one for each of the eight rings of the TMA detectors. The resulting GEANT-based, energy-to-primary particle yield conversion functions are shown

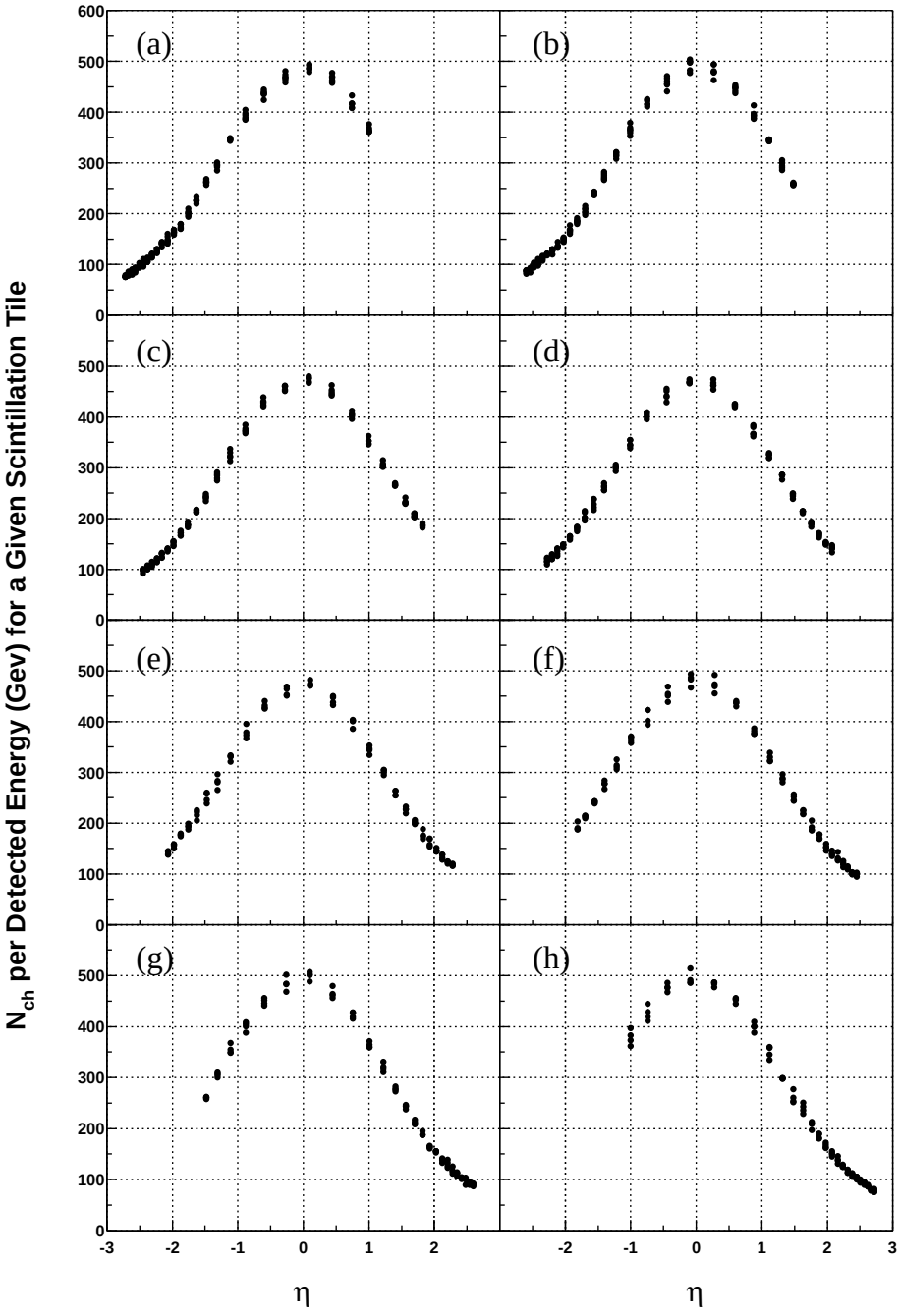

Figure 6.14: Tile Energy to N_{ch} Conversion
(a), (b) ... (h) corresponds to the columns of Figure 4.15, which shows eight columns along the beam axis.

in Figure 6.14. The actual calibration functions are obtained by fitting polynomial functions to the plots in this figure.

As a test of the unfolding procedure, a GEANT simulation using the Hijing event generator was used to simulate "experimental" data for central collision events. These "data" were then analyzed to determine the number of primary particles emitted as a function of pseudorapidity. Comparison of the actual primary distribution and that deduced based on the simulated data is shown in Figure 6.15, where excellent agreement is achieved. When the same test is conducted

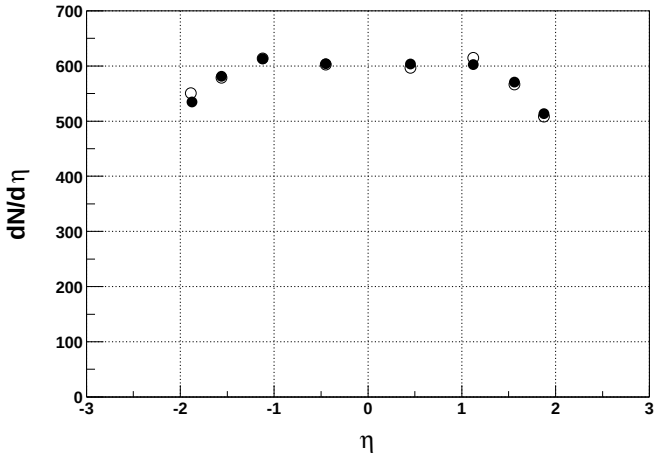

Figure 6.15: Comparison of Particle Productions in the GEANT simulation with the HIJING model
The open circle is obtained from the using the conversion function of Figure 6.8. The closed circle is from the Hijing model.

with the use of different event generators, which have a somewhat different mix and size of primary particles, similar agreement is achieved. These results suggest that the above conversion functions are well defined, at least within the GEANT simulations.

6.3 Beam-Beam Counter Arrays

6.3.1 Linearity

The Beam-Beam Counter arrays (BBC), which are comprised of Cherenkov radiators coupled to photomultiplier tubes (PMT), were primarily designed to produce a good time-zero (or a vertex) measurement for the collisions. Two different sizes of photomultiplier tubes are used in the detector: one with 3/4" diameter and other with 2" diameter. During the commissioning and

first-year run, it was realized that the small PMTs were receiving too many photons from the Cherenkov radiators to produce a linear response of output signals with respect to the number of incident photons. Figure 6.16 shows the non-linearity of one of the small PMTs. The left figure

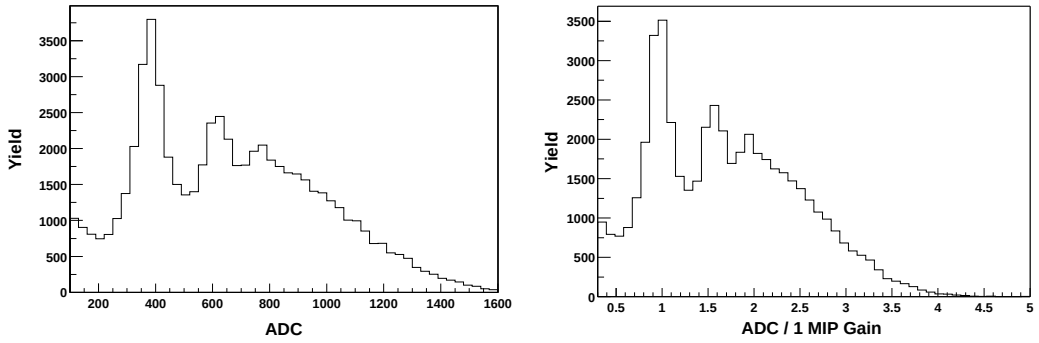

Figure 6.16: Typical BBC Small PMT Non-linearity
The left figure is raw ADC distribution. The right figure shows the distribution, which is the left figure divided by 1 MIP ADC value (constant).

shows the raw ADC distribution of the PMT after pedestal subtraction. The peaks representing the response of the PMT to one, two and three charged particles are clearly seen. However, close inspection reveals that the ADC gap between the pedestal (0 ch) and the first peak (~400 ch) is considerably larger than the gap between the first peak and the second peak (~210 ch). Furthermore, the gap between the second and the third peaks (~ 140 ch) is even smaller. The right figure shows this trend more clearly by dividing the left figure by the mean ADC value (offset from the pedestal) of the first peak. If a PMT produces a linear response to the number of input photons, the mean values of all peaks should be aligned to the integer number except for small shifts resulting from the presence of the background. However, that is not the case here.

The larger PMTs used for BBC detectors do not have any noticeable non-linearity. This is shown in Figure 6.17 for one of the large PMTs. It is clearly seen that the mean values of all visible peaks are located close to integer values. Although this does not guarantee the linearity of the large PMTs over the full dynamic range, the fact that good linear response of the large PMTs up to the size of input corresponding to 4 charged particles is used to calibrate the small PMTs. Figure 6.18 shows the experimental setup for this calibration. To calibrate the small PMTs, a pulsed laser is used as a light source. From the laser, the light will travel through the filter, which is used to control the amount of light, to a beam splitter. The splitter passes one

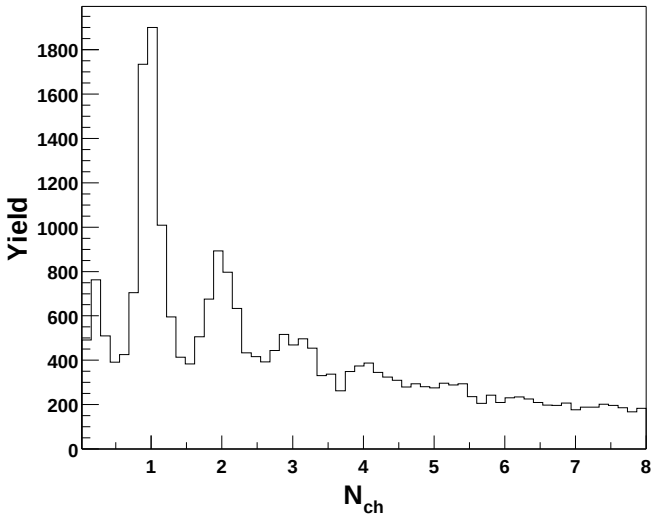

Figure 6.17: Typical BBC Large PMT response

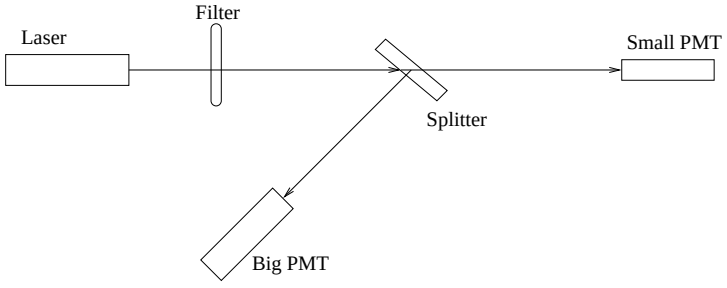

Figure 6.18: Setup for Beam-Beam Small PMT Calibration

half of the light to a small PMT and reflects the other half to a large PMT. Therefore, the small and the large PMTs receive well known amounts of lights. By changing the filter to produce a different intensity of light, the response of the small PMT is studied against that of the large PMT.

Figure 6.19 shows the results of this calibration after correcting for different gains of the small PMTs. The figure shows clearly that the small tubes are saturating. Without saturation,

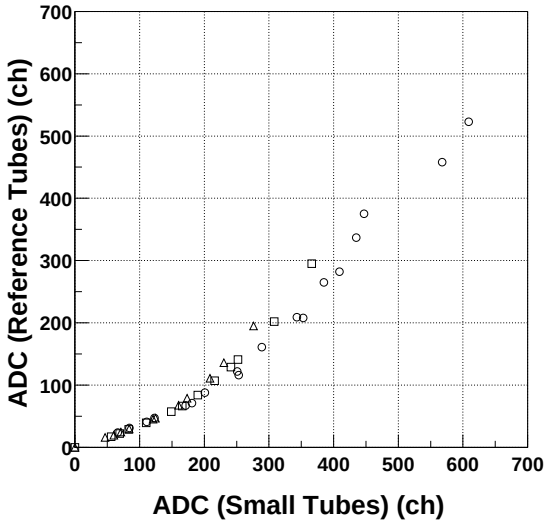

Figure 6.19: Beam-Beam Counter Non-linearity Correction
The different markers correspond to the different small PMTs used for calibration. The gain of the small PMTs are matched by single MIP response. The gain of the large PMT is different from that of the small PMT.

all data points should be aligned to a straight line. (The line does not necessarily have unit slope since the gains of the large and small PMTs are different.) Moreover, on closer inspection, it is seen that there are small variations among the small tubes with up to 20% differences in their relative response. Therefore, the data for each tube need to be carefully calibrated for non-linearity.

Figure 6.20 shows the distribution of a typical small BBC PMT after the non-linearity correction. The mean values of all peaks are close to integer values, indicating good linearity of the calibrated data.

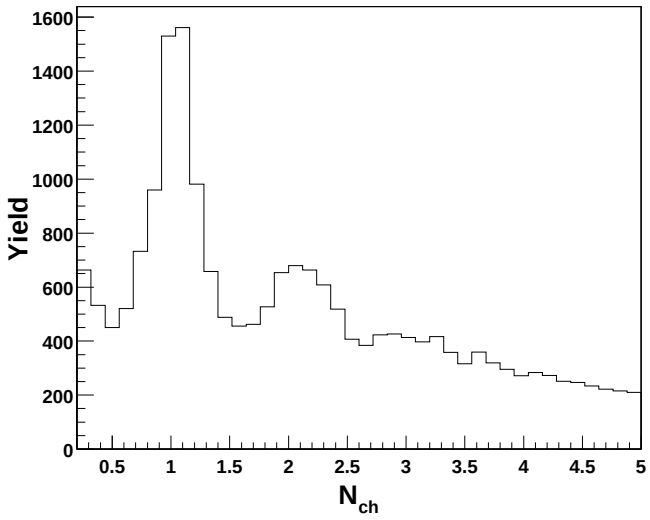

Figure 6.20: BBC element MIP response after Non-linearity Correction

6.3.2 Background subtraction

The raw multiplicity distribution seen in Figure 6.20 was made by particles passing through the Cherenkov radiators and producing photons that subsequently hit the PMT photo-cathode. While it is true that the BBC detectors have some directionality, based on the properties of the Cherenkov radiators coupled to the PMTs, it is still possible for background particles originating from sources away from the vertex to contribute to the signals. Therefore, the situation is similar to that of the SiMA and TMA detectors. A Monte Carlo simulation using GEANT is used to estimate the level of this background in the BBC detectors. Figure 6.21 shows the results of this simulation for the large PMTs. The figure shows that the output of the GEANT simulation far exceeds the input of the Hijing event generator. In fact, the $dN_{ch}/d\eta$ values deduced using the BBC detectors is about 50% more than the input values. To remove this difference, the ratio of the output $dN_{ch}/d\eta$ to that of the input was calculated. This ratio is applied to the real data to remove the background contribution. More information for the background correction for the BBC detectors is found in Reference [55].

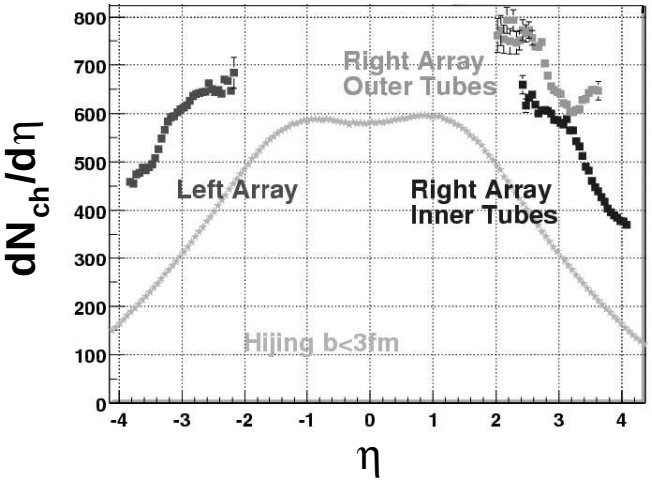

Figure 6.21: BBC simulation for large PMTs.
The line indicates the Hijing model input distribution for the simulation. All other points are the $dN_{ch}/d\eta$ values that would be deduced based on the simulated tube response without considering the background contributions. The simulations are done using GEANT to determine the expected background.

Chapter 7

Determination of Multiplicity and Centrality

The multiplicity array was designed with the expectation that a single ultra-relativistic collision of two Au nuclei could result in the production of over a thousand particles. The actual number of particles detected is influenced by two major factors. The first one is the location of the event vertex. Since RHIC is a particle collider experiment, the location of the collision vertex changes event-by-event. Consequently, since the detector positions are fixed, their acceptances also change event-by-event, affecting the number of particles detected. The finite size of a gold ion also leads to an event-by-event variation in the particle multiplicity. The severity of a collision depends on the distance between the two colliding nuclei. This is called the centrality of an event. This chapter shows how the charged particle multiplicity and reaction centrality are measured using the Silicon Strip Detector Array (SiMA), the Scintillation Tile Detector Array (TMA) and the Beam-Beam Counter arrays (BBC).

7.1 Multiplicity Determination

The charged-particle multiplicities of events are determined by the BBC and the Multiplicity Array detectors (MA). The MA is composed of the separate SiMA and TMA elements. The phase space covered by the BBC and MA systems are quite different. At the nominal vertex

location, the BBC measures charged-particle multiplicity for $3.0 < |\eta| < 4.2$, whereas the MA measures charged particles in the range of $|\eta| < 2.2$.

7.1.1 Silicon Strip Detector Multiplicity Array

The Silicon Strip Detector Multiplicity Array (SiMA) measures the multiplicity of an event by detecting energy loss of charged particles passing through the detector elements. The details of the method have already been discussed in Section 6.1. If all collisions occurred at the nominal vertex position, obtaining an event multiplicity would, in principle, be a simple matter of summing the measured multiplicity of each Si strip of the array. In reality, this is not the case because of the change in the detector acceptance caused by having a range of vertex positions. Figure 7.1 shows a histogram of the measured vertex locations for a typical run. The distribution

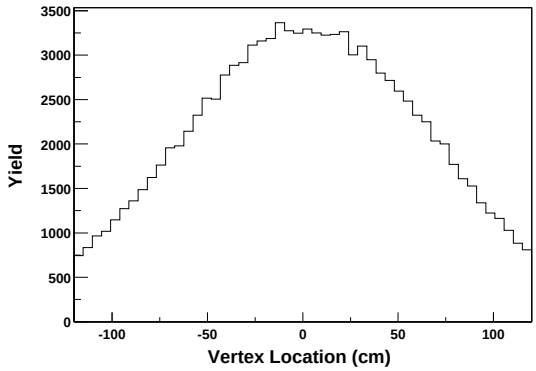

Figure 7.1: Vertex Distribution

has a Gaussian-like shape with, for this particular run, a small offset from the nominal location of the vertex observed. The vertex distribution has a typical Gaussian width σ in the range of 40cm to 100cm depending on the particular condition of the beam.

For a given event, the detected number of charged particles is highest at midrapidity, and it becomes smaller as the particle rapidity gets closer to the beam rapidity. Because of this and the limited detector coverage, the measured, "raw" multiplicity is strongly dependent on the location of the vertex. Figure 7.2 shows this effect clearly. The maximum value of measured multiplicities that have not been corrected for detector acceptance is relatively constant between ± 10 cm of the nominal vertex location. Then, it decreases dramatically as the vertices go further away from the nominal location. Figure 7.2b shows the same plot after application of the acceptance

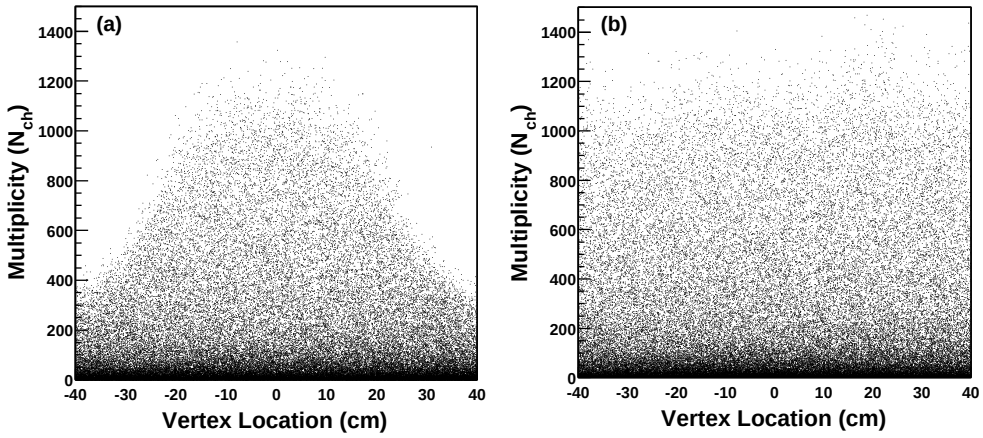

Figure 7.2: Event multiplicities for different vertices by the Silicon Strip detector (a) represents the distribution of event multiplicities without the correction of the detector acceptance. (b) shows the same thing after the correction.

corrections. Once the acceptance is corrected, the distribution is flat against the locations of the vertices. This correction is achieved by taking mean values of multiplicities for the same centrality class with the different vertex cuts. Figure 7.3 shows an example of this technique. The centrality class is determined by the measured multiplicity. The range of vertices for each

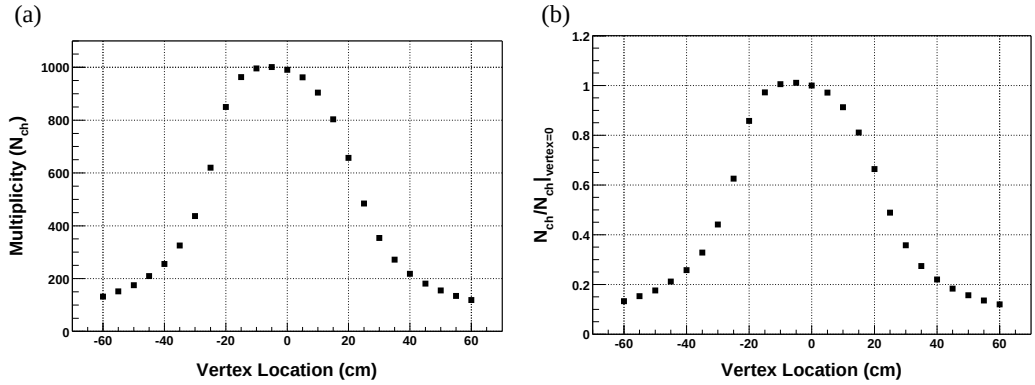

Figure 7.3: Geometric acceptance correction for the given strip of a Silicon strip detectors (a) represents the mean value of multiplicities for top 5% central events. (b) shows the ratio of measured multiplicity at the different vertices relative to the nominal vertex.

cut is set to 5 cm to minimize the effect of acceptance change within the selected range. Then, for each selected range, the mean multiplicities of different centrality classes are obtained, assuming a linear relationship between centrality and multiplicity. The ranges of centralities used for this analysis are 0-5%, 5-10%, 10-20%, 20-30%, 30-40% and 40-50%. Figure 7.3a shows mean

multiplicities for the 5 % most central events. These values are compared to the mean value of multiplicity at the nominal vertex in Figure 7.3b. A function for acceptance correction is obtained by fitting a polynomial function to this curve. As a result, all measured multiplicities are normalized to that at the nominal vertex.

To obtain an event-by-event multiplicity, one more correction needs to be applied. This correction stems from the fact that the SiMA covers less solid angle than the TMA. (The multiplicity by the TMA detectors is discussed in the next section.) To obtain an average multiplicity from the two arrays, a correction was made to normalize the SiMA multiplicities to the TMA multiplicities. This constant normalization, which has a value of 1.55 and 1.66 for the $\sqrt{s_{NN}} = 130$ GeV $\sqrt{s_{NN}} = 200$ GeV runs, respectively, is obtained by comparing the multiplicities from the SiMA to that from the TMA for many events. Figure 7.4 shows the correlation of multiplicities by the two arrays after all corrections have been applied. As expected, a strong,

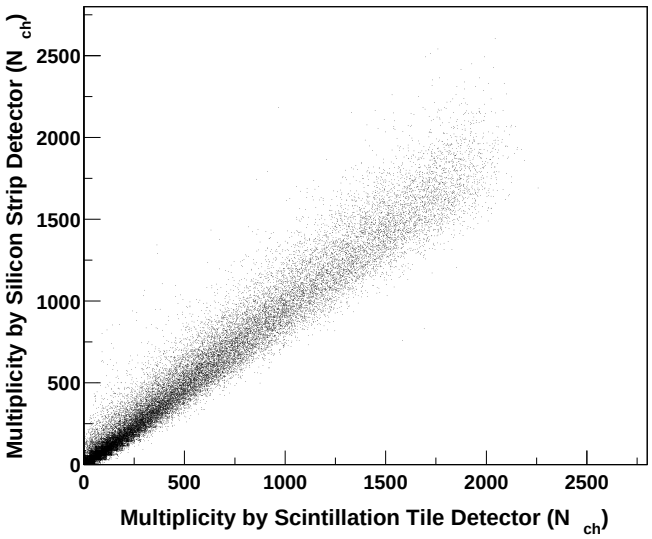

Figure 7.4: SiMA vs TMA

linear correlation exists between the two measurements.

7.1.2 Scintillation Tile Detector Multiplicity Array (TMA)

Similar to the SiMA, the TMA measures event multiplicity by detecting energy loss of particles through its detector elements. The details of the measurement technique are discussed in Section 6.1. Because of the similarity of the SiMA and the TMA, the technique used for the acceptance

correction is also identical between the two systems. Figure 7.5 shows the multiplicities of events as a function of vertex positions. It is clearly seen that the maximum value of the multiplicities is

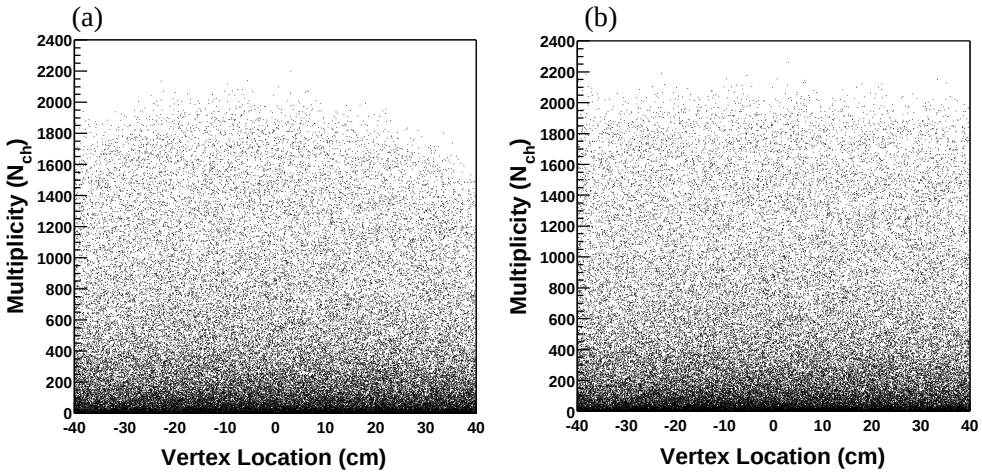

Figure 7.5: Event multiplicities for different vertices by the Scintillator Tile detector (a) represents the event multiplicity without the correction of the detector acceptance. (b) shows the multiplicity after the correction.

achieved for the vertices within 10 cm left of the nominal vertex location. The asymmetry about the nominal vertex results from the configuration of the detectors, as shown in Figure 4.15. Since there are more tiles on the left of the nominal vertex location, the measured multiplicity is larger there. Also, comparing Figure 7.5a to Figure 7.2a, one finds that the acceptance correction for the TMA is smaller than the SiMA. Despite the similar coverage in pseudorapidity, the physical extent of the TMA is greater than that of the SiMA, leading to a more uniform response over the indicated range of vertex positions. Figure 7.6 shows the TMA acceptance correction factor. The correction factor is less than 20% within $\pm$30 cm of the nominal vertex location, whereas that of the SiMA is as much as 50% for the same range.

7.1.3 Beam-Beam Counter Arrays (BBC)

The Beam-Beam counter arrays (BBC) measure the charged-particle multiplicity of an event by detecting the Cherenkov light of particles passing through Cherenkov radiators mounted onto photomultiplier tubes (PMT). The detail of the analysis method used for each radiator-PMT combination is discussed in Section 6.3. Similar to the SiMA and the TMA, the acceptance of the arrays change with vertex location, and a corresponding geometric correction must be applied to

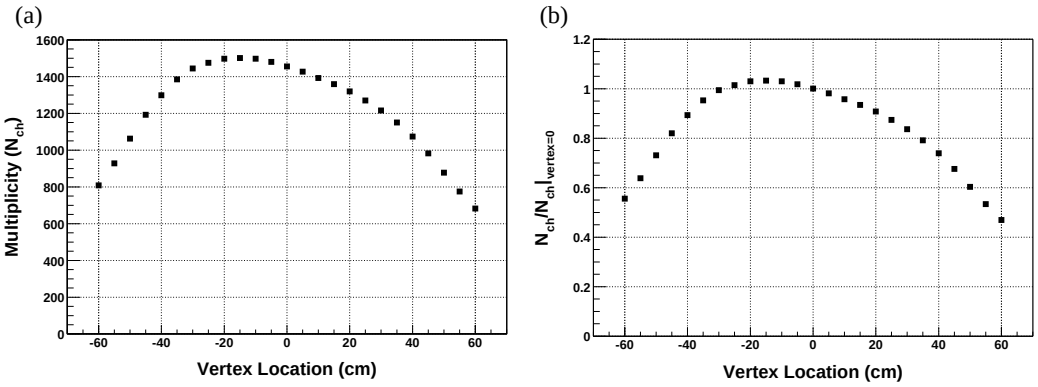

Figure 7.6: Geometric Correction for Multiplicity by Scintillator Tile Detector
(a) represents the mean value of multiplicities for the top 5% central events. (b) shows ratio of multiplicities at the different vertices to that at the vertex=0 cm.

the data. Figure 7.7 shows a plot of multiplicities by the BBC against vertex position. The effect

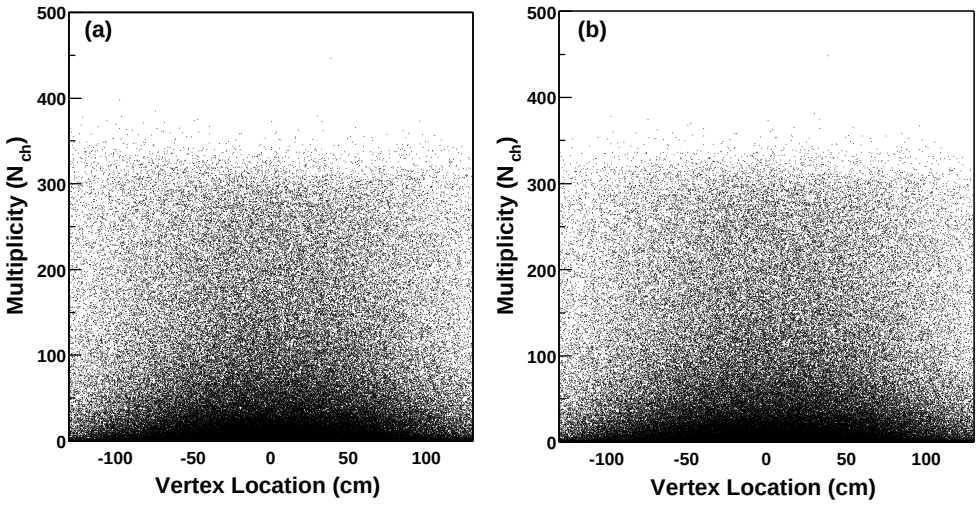

Figure 7.7: Event multiplicities for different vertices based on the BBC arrays
(a) represents the event multiplicities without the correction of the detector acceptance. (b) shows the multiplicities after the application of the acceptance correction.

of vertex position is small for the BBC arrays because they are located far away (2.1 m on both sides) from the nominal location of a vertex. Only a small increase in the maximum multiplicity is observed as the vertex moves to the extreme left (or negative) direction. Since the solid-angle coverage of the left array of the BBC is larger than that of the right array, the multiplicities tend to increase as vertices move closer to the left array. Using the same technique discussed in Section 7.1.1, a small correction is applied to obtain the acceptance-corrected multiplicities

shown in Figure 7.7b.

Figure 7.8 shows the correlation between the acceptance-corrected multiplicities by the BBC and the MA. As expected, the two measurements are found to have a strong linear correlation.

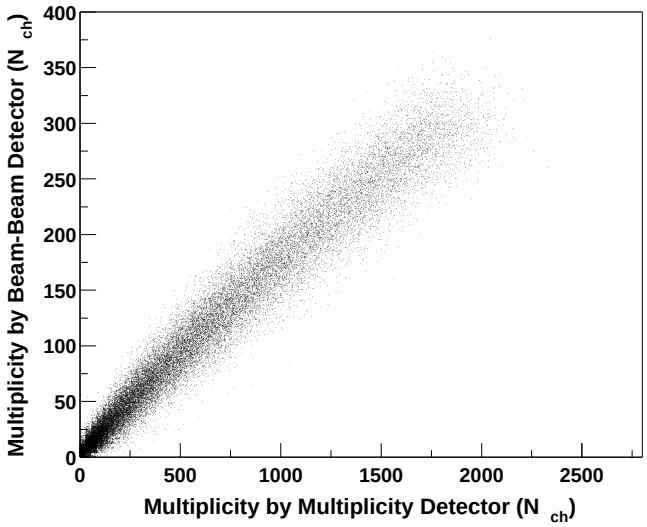

Figure 7.8: Correlation of multiplicities by the BBC and the MA measurement

However, the small saturation for the BBC arrays is still visible because of the imperfection in the non-linearity correction of the PMTs used in the BBC arrays.

7.2 Centrality Determination

Defining an event centrality gives a way to categorize the fraction of the total cross section in the nucleus-nucleus collision by the distance of closest approach between the centers of the two colliding nuclei. Figure 7.9 depicts this by two simple diagrams representing very central and peripheral collisions, respectively. In the central collision shown in Figure 7.9a, the centers of two colliding nuclei are very close to each other. In this case, most of the volumes of two nuclei participate in the collision, leading to a more violent collision. In the peripheral collision shown in Figure 7.9b, the centers of two colliding nuclei are far apart. (But, the distance between the two can not be more than the twice the size of the radius of the nucleus for a reaction to occur.) Then, only a small fraction of their total volumes participates.

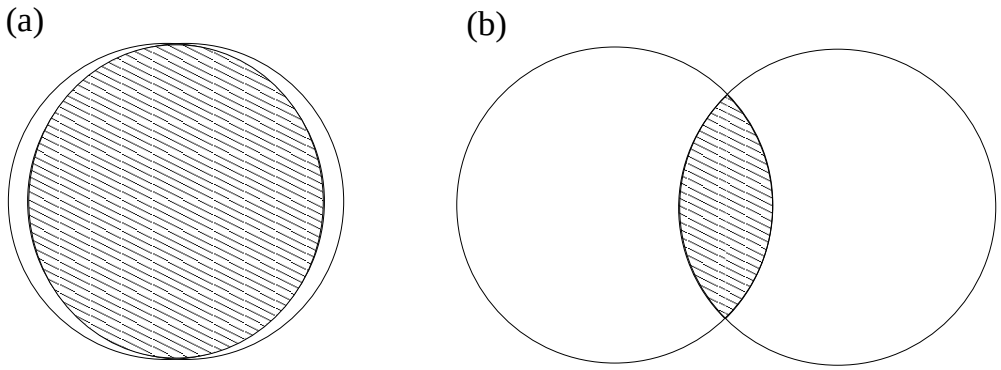

Figure 7.9: Definition of Centrality
The large open circle represents two colliding nucleus. The directions of two nuclei are into or out of the drawing. The shaded region represents the sections of each nucleus that suffers a collision. (a) represents a very central collision. (b) represents a peripheral collision.

7.2.1 Event Selection for the Centrality Measurement

With the acceptance-corrected values of event multiplicities, the determination of reaction centrality is a relatively simple operation since the larger the value of the event multiplicity, the more violent and the more central the collision is. However, since the centrality is related to the fraction of events with a charged-particle multiplicity above a certain value, it is important to base this fraction on the accurate total number of events undergoing a nuclear interaction. Because of background processes, the triggering system can be triggered by "false" collisions. Figure 7.10a illustrates some of these false triggers. In this figure, the area enclosed by the

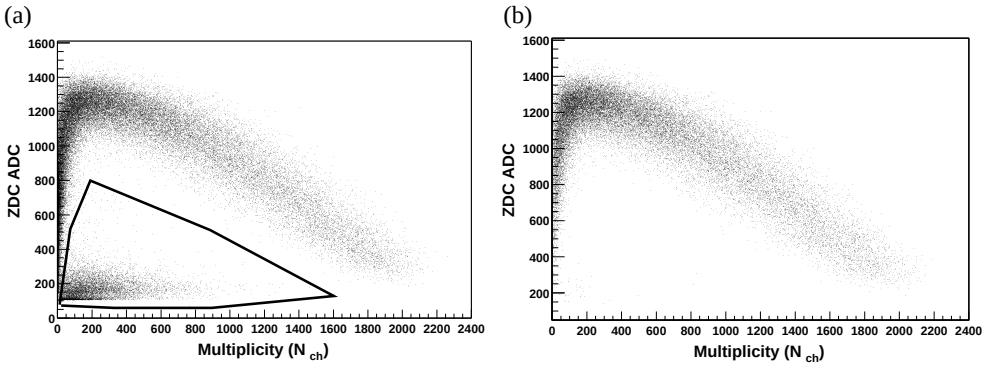

Figure 7.10: ZDC energy (ADC) vs Multiplicity
(a) The events enclosed by the line represent the false triggers. (b) represents the same correlation when the location of vertices determined by ZDC and BBC are within 5 cm.

line represents "false" collisions. They are associated with relatively low energy in the ZDC and

with a reasonable value of multiplicity. One possible cause of these events is that the ZDCs are triggered by background particles and, consequently, give the wrong location for the event vertex. Figure 7.10b shows how the background events can be reduced by requiring vertices determined by the ZDC and the BBC detectors to be within 5 cm of each other.

Figure 7.11 shows another way to see if the events enclosed by the line in Figure 7.10a are false collisions. This figure shows the simulated and experimental distribution of the difference

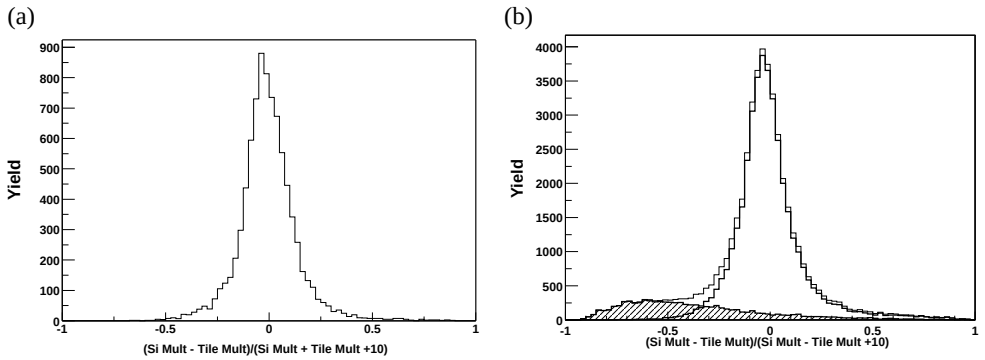

Figure 7.11: Difference of Multiplicities by Silicon and Tile detector
(a) GEANT simulation (b) experimental events. The shaded region represents the collisions enclosed by the line in Figure 7.10 (a). The dark line represents events after the subtraction of the shaded region.

in the SiMA and the TMA multiplicities by calculating the following equation:

$$(N_{ch-SiMA} - N_{ch-TMA})/(N_{ch-SiMA} + N_{ch-TMA} + 10) \tag{7.1}$$

where

$$N_{ch-SiMA} \equiv \text{multiplicity determined by the SiMA detectors} \quad ,$$
$$N_{ch-TMA} \equiv \text{multiplicity determined by the TMA detectors} \quad ,$$

and $N_{ch-SiMA}$ takes into account the solid-angle difference of the two arrays. If the event multiplicities determined by the two arrays are well calibrated, they should produce a symmetric distribution. This is seen in Figure 7.11a, which is based on the GEANT simulation. In Figure 7.11b, it is shown that the experimental distribution is not symmetric but, rather, has a large tail towards negative values. A closer inspection reveals that much of this tail is associated with

the area enclosed by the line in Figure 7.10a. This is shown by the shaded area in Figure 7.11b.

Once the obvious background is removed, there is one more concern for the possible background. This condition happens when the measured multiplicity is very small but still above zero. Because the pedestal distribution of each detector element in the MA system has an associated width of finite size, the summation of all elements of the MA detectors can yield non-zero multiplicity. When this condition occurs with a "false" collision event triggered by background particles in the ZDC detectors , there can exist events with small values of the charged-particle multiplicity with "false", but acceptable, vertex positions. Unlike the previous situation, these events, which are numerous, can not be easily removed by the correlation of vertex positions between the ZDC and BBC detectors because of the lack of efficiency in the BBC system for low multiplicity reactions. As a result, a correction for these "false" collisions was devised based on the GEANT simulations.

The technique used to account for this difficulty in measuring very low multiplicity events is as follows. First, it is assumed that there are no false events with charged-particle multiplicity larger than 200 N_{ch-TMA}. This is reasonable because the vertices of those events can be checked by the BBC and because the average number of detected charged-particle multiplicity of each element in the TMA detectors is relatively large (at least 5) for such events. Second, it is assumed that the GEANT simulation using the Hijing event generator can correctly reproduce the low multiplicity distribution. This reliance on the model calculation is questionable and contributes to the systematic uncertainties. Other event generators were used to check the model dependence, which was found to be very small. Then, using simulated "data", the ratios of the total number of events with TMA multiplicity less than a given value m to the number of events with multiplicity less than 200 are calculated:

$$R(m) = \frac{\sum_{N_{ch-TMA}=0}^{N_{ch-TMA}=m} n(N_{ch-TMA})}{\sum_{N_{ch-TMA}=0}^{N_{ch-TMA}=200} n(N_{ch-TMA})} \tag{7.2}$$

where

$$\begin{aligned} m &= \text{cut value of multiplicity } (0 \leq m \leq 200) \\ N_{ch-TMA} &= \text{charged multiplicity by the TMA detectors} \\ n &= \text{number of events} \quad . \end{aligned}$$

(Only the TMA system was used for this correction because of its superior resolution for single minimum ionizing particles.) Figure 7.12 shows this technique visually by displaying the distribution of simulated measured multiplicities in two different ranges. In the top figure, the

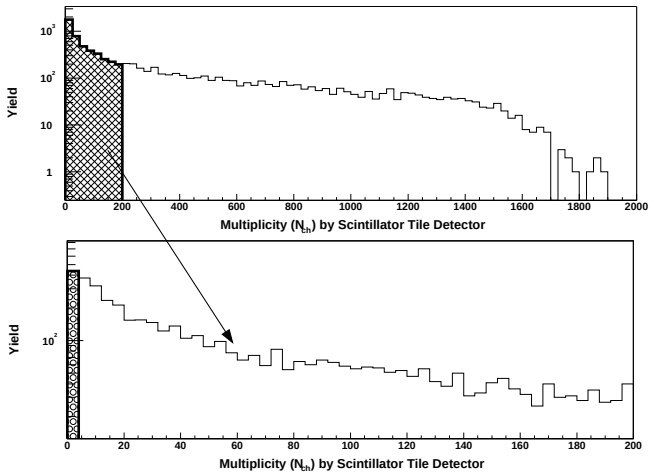

Figure 7.12: Centrality Normalization Simulation
The top figure represents the simulated multiplicity distribution by GEANT with the Hijing input. The bottom figure is a close up view of this multiplicity between 0 to 200 N_{ch}.

shaded region represents the events with their multiplicities less than 200 $N_{ch-tile}$. The yield (or number of events) in this shaded region represents the denominator of Equation 7.2. In the bottom figure, the shaded region represents the numerator of Equation 7.2 for the case of m=4. By varying the value of m in Equation 7.2, the ratio of yields in the two shaded regions of Figure 7.12 are obtained for several values of m.

With these ratios, a correction is applied to the experimental data to obtain the number of events less than a certain value m. Then, the corrected total yield of collisions, $Y(m)$, as a function of m is given by

$$Y(m) = \left(\sum_{N_{ch-TMA}=m}^{N_{ch-TMA}=200} n \right) * \frac{1}{1-R(m)} + \sum_{N_{ch-TMA}>200}^{N_{ch-TMA}=max} n \qquad (7.3)$$

Figure 7.13 shows the ratio $Y(m)/Y(4)$ for several values of m. As can be seen, for the value of m larger than 4, the total yield is very stable, with a deviation of less than one percent. This indicates that the model calculation and the experimental data produce very similar distributions within the multiplicity values of 4 to 200. But, when the value of m is less than 4, the estimated

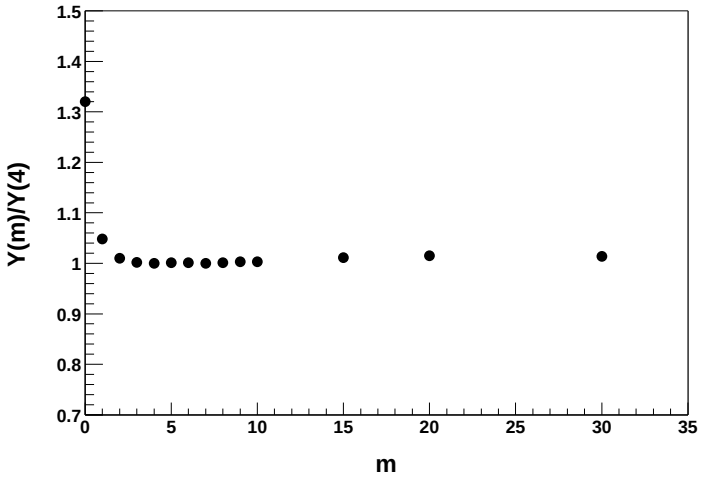

Figure 7.13: Effect of Value m in Equation 7.3

total yield gets larger as m becomes smaller. In fact, if there is no cut, which is the case for m being zero, the total yield is more than 30% larger than that of m being equal to 4. Since it is desirable to use as small a value of m as possible without including background events, a value of $m = 4$ was choosen for this analysis.

7.2.2 Centrality Selection using the Multiplicity Array

The method of determining the event centrality based on the observed charged-particle multiplicity and the relationship of the deduced centralities to the reaction impact parameter was studied using the GEANT simulations. In Figure 7.14a, the simulated multiplicity distribution is shown

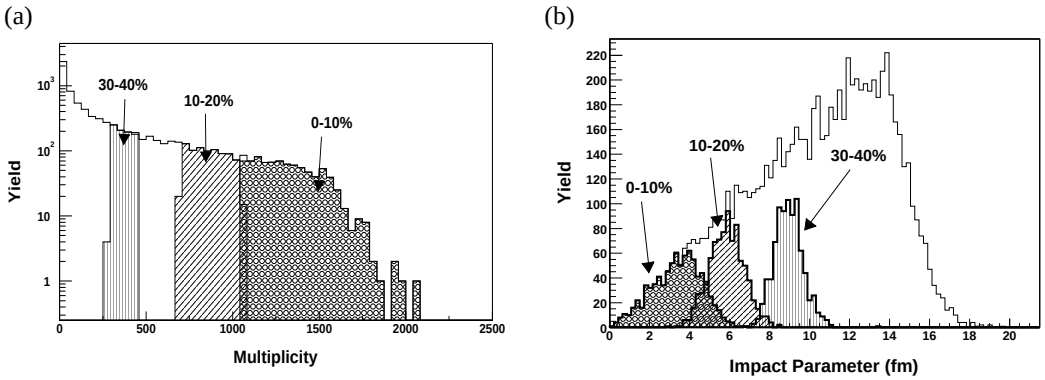

Figure 7.14: Centrality Selection in GEANT Simulation with Hijing Input

with a few centrality selections indicated by the different shaded regions. While the centralities

of collisions are determined experimentally by the value of multiplicities, the theoretical centrality is usually interpreted as a statement of impact parameter range. Therefore, Figure 7.14b shows the corresponding impact-parameter distributions for the selected event multiplicities. It is observed that the multiplicity-based centrality does not map directly to impact parameter, but exhibits a Gaussian-like distribution, except for the highest centrality selection. Since the highest experimental centrality can not be more central than that of the theoretical model, any experimental deviations will tend to lower the experimental centrality. For a more quantitative inspection of this behavior, Table 7.1 shows the mean values of impact parameters selected by the experimental and theoretical methods for given centralities. This clearly shows that the

Table 7.1: Comparison of Mean Value of Impact Parameter b at $\sqrt{s_{NN}} = 200$ GeV

Centrality Range	Mean b by Impact Parameter	Mean b by Multiplicity Detector
0-5%	2.35±0.04	2.61±0.05
5-10%	4.15±0.02	4.11±0.04
10-15%	5.37±0.02	5.39±0.04
15-20%	6.32±0.02	6.34±0.03
20-25%	7.15±0.02	7.17±0.03
25-30%	7.93±0.01	7.93±0.03
30-35%	8.61±0.01	8.63±0.03
35-40%	9.25±0.01	9.29±0.03
40-45%	9.84±0.01	9.87±0.03
45-50%	10.4±0.01	10.4±0.03

centrality obtained by selecting a range in multiplicity results in the same selection of impact parameters as found using a direct conversion from the model centrality to impact parameter, except for the most central collisions where the multiplicity method leads to a somewhat larger value.

Figure 7.15 shows the experimental centrality selections used for this analysis at the two beam energies. It is easily noticed that the data with $\sqrt{s_{nn}} = 200$ GeV exhibits slightly larger (about 12%) multiplicity distributions than that at $\sqrt{s_{nn}} = 130$ Gev. The lowest centrality range is the 40-50% range. Because of the steep increase of yields for lower multiplicity events, the systematic uncertainty of centralities in those events is higher than the centralities selected from the flat section of the distribution.

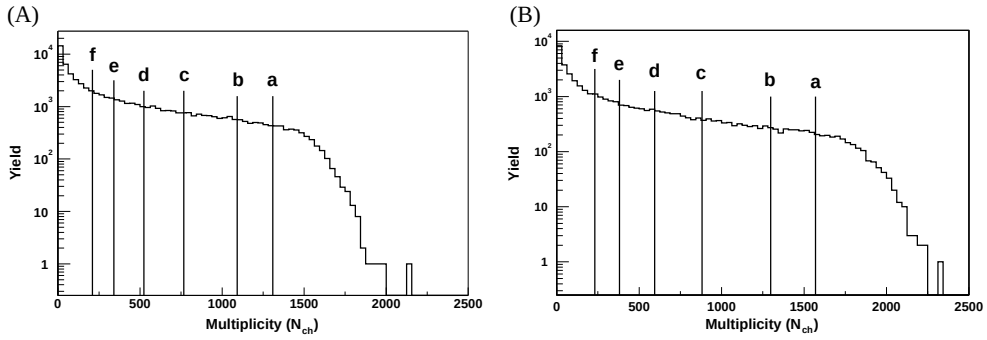

Figure 7.15: Experimental Centrality Selection
The lines (a) through (f) represent different centrality cuts. They are 0-5%, 5-10%, 10-20%, 20-30%, 30-40% and 40-50%. (A) is for $\sqrt{s_{nn}} = 130$ GeV. (B) is for $\sqrt{s_{nn}} = 200$ GeV.

7.2.3 Centrality Selection using the Beam-Beam Counter Arrays

As the Beam-Beam Counters also measure charged-particle multiplicity, they can also be used to determine the reaction centrality. Ideally, this should not be necessary since the SiMA and the TMA detectors already provide a good centrality measurement for the collisions. Also, one would like to use the same detectors to determine the centralities for all events to make the analysis consistent. However, to use the BBC to extend the pseudorapidity-dependent multiplicity distribution to high pseudorapidities, it was realized that it would be necessary to have a separate centrality determination than that offered by the SiMA and the TMA detectors. The geometry of the BBC arrays is such that a very wide range of vertex locations ($\pm$120 cm of the nominal location of the vertex) can be used to achieve a wide pseudorapidity coverage. The SiMA and the TMA can not provide centralities for events with vertices located much outside of the geometrical extent of these arrays (about $\pm$30 cm on either side of the nominal vertex position). This is easily understood by viewing the acceptance corrections for these two detectors, which are shown in Figure 7.3 and 7.6. The correction for more distant vertex locations becomes large and introduces a significant systematic uncertainty in the experimental results. Unlike the MA, the acceptance correction of the BBC arrays, shown in Figure 7.7, is very small for a very wide vertex range. It was therefore decided to use the separate centrality determined by the BBC arrays in the analysis of the BBC charged-particle multiplicities.

To assure consistency of the MA and the BBC centrality determinations, all of the BBC centrality calibrations were done using events with collision vertices within $\pm$30 cm of the nominal vertex position. Figure 7.16 illustrates the technique used to calibrate the BBC centralities.

First, collisions in a certain centrality range are selected based on the MA detectors. This is

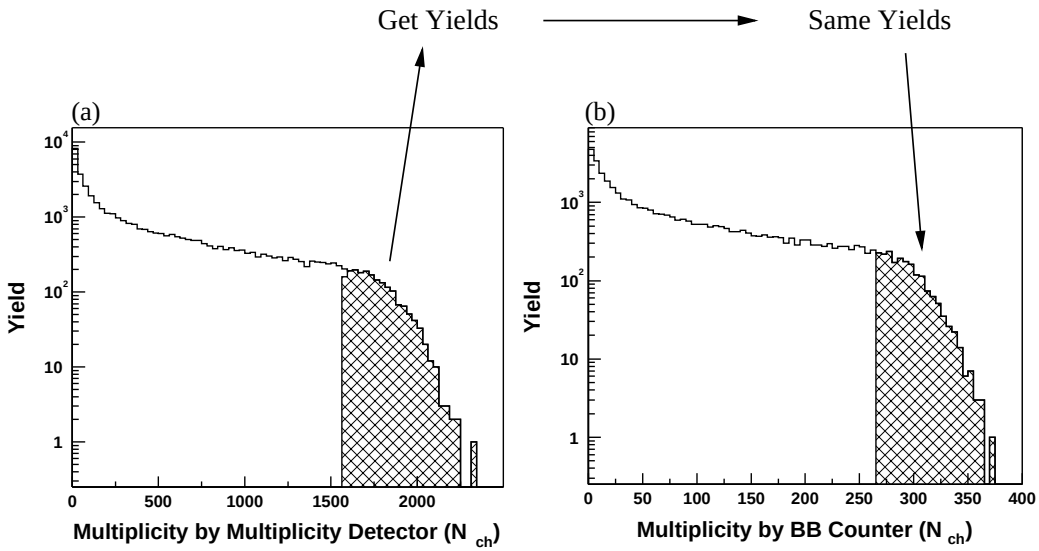

Figure 7.16: Centrality Selection by the Beam-Beam Counter

shown as a shaded region in 7.16a. Then, using the multiplicity distribution observed by the BBC arrays, the same number of the most central events are selected from this distribution, as shown by the shaded region in Figure 7.16b. This provides a BBC multiplicity cut for the specified centrality. Figure 7.17 shows how the MA and BBC multiplicities compare. Figure 7.17a, reproducing Figure 7.8, shows the correlation of the multiplicities determined by the two systems. The shaded region in Figure 7.17b shows the MA events that are selected by a 5% centrality cut using the BBC, to be compared with the region enclosed by the dark line which are the 5% most central MA events. Obviously, the two methods of selecting centralities do not select exactly the same events. However, about 70%-80% of the events are common to both centrality measurements. Moreover, for events with collision vertices within 30cm of the nominal vertex, the BBC pseudorapidity distributions selected by the two centrality methods were found to be the same within 2 %. Therefore, this technique was used to obtain the centrality cuts for the BBC arrays over the extended range of vertex location that could be used for these arrays.

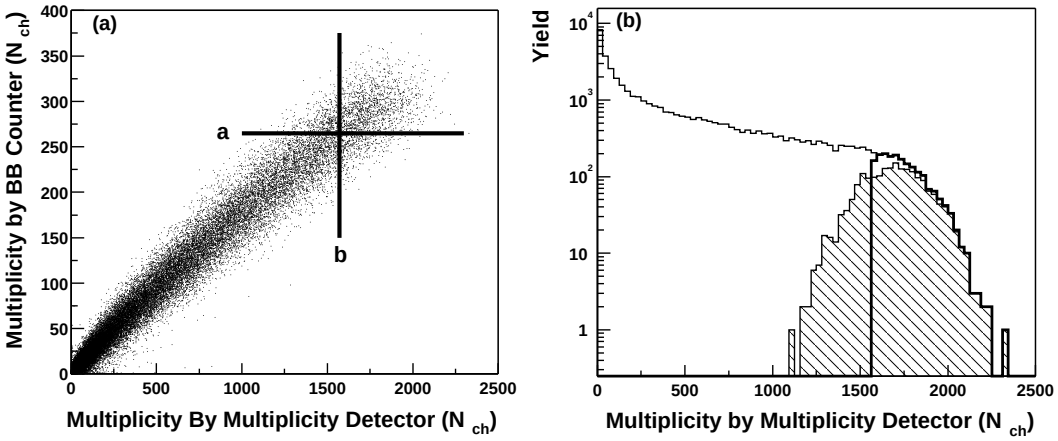

Figure 7.17: Comparison of Centralities by the BBC and the MA
(a) shows the correlation of multiplicities determined by the two arrays. The lines a and b indicate the 5% centrality cut for the BBC and the MA, respectively. (b) shows the projection of figure (a) onto the horizontal axis. The area enclosed by the dark line is the 0-5% central selection by the MA. The shaded region represents the 0-5% central selection by the BBC.

Chapter 8

Charged Particle Production in Ultra-Relativistic Au+Au Collisions

The charged particle multiplicity, N_{ch}, of Au+Au collisions is analyzed for data collected during a two-year period from 2000 to 2001 at RHIC. During the first run in year 2000, the accelerator operated at 65% of its maximum design energy to produce Au+Au collisions at $\sqrt{s_{NN}} = 130$ GeV. During the second year run, the machine operated at the design energy of $\sqrt{s_{NN}} = 200$ GeV. N_{ch} and its pseudorapidity distribution, $\frac{dN_{ch}}{d\eta}$, were measured with a combination of the Zero Degree Calorimeters (ZDC), the Silicon Strip Detector Array (SiMA), the Scintillation Tile Detector array (TMA) and Beam Beam Counter arrays (BBC) subsystems of the BRAHMS experiment. Detailed descriptions of these subsystem are presented in Chapter 4. The BRAHMS data put severe limits on theoretical models describing relativistic heavy-ion collisions.

8.1 Model Predictions

Finding evidence for the creation of a quark-gluon plasma from the final-state hadrons emerging from an ultra-relativistic heavy-ion collision requires comparison of the theoretical model predictions with experimental results. Most of the current theoretical models highlight one or more aspects of the relativistic heavy-ion collision, placing lesser emphasis or ignoring others. Since none of the present models include all of the known expected physical processes, comparisons of

theoretical values to experimental data provide a deeper understanding of the underlying physical processes by eliminating (or suppressing) one feature of a model and accepting others. For example, in terms of charged-particle production, the different models predict a pseudorapidity density at midrapidity, $dN_{ch}/d\eta|_{\eta=0}$, to be in the range of 600 to 1400 for Au+Au reactions at the highest RHIC energy. With a difference of a factor of two in the model predictions, the experimental results can easily highlight inadequacies of certain models. Although there exist many models in this field, four popular models with different features are discussed briefly in this section.

8.1.1 Hijing Model

The Hijing model [56, 57] is based on perturbative QCD (pQCD) with emphasis on the production of multiple mini-jets. A mini-jet [58] is a jet with small transverse momentum and one that is not resolvable as a distinct jet experimentally. Since it is believed that the production of mini-jets contributes significantly to transverse energy in the relativistic heavy-ion collisions, this model tries to address this feature by considering hard and semi-hard parton scattering based on pQCD. For soft interactions, the model considers multiple-soft gluon exchange between quarks. The effect of jet quenching is included as a final state parton interaction.

Figure 8.1 shows the pseudorapidity distribution predicted by this model. For the 0-5%

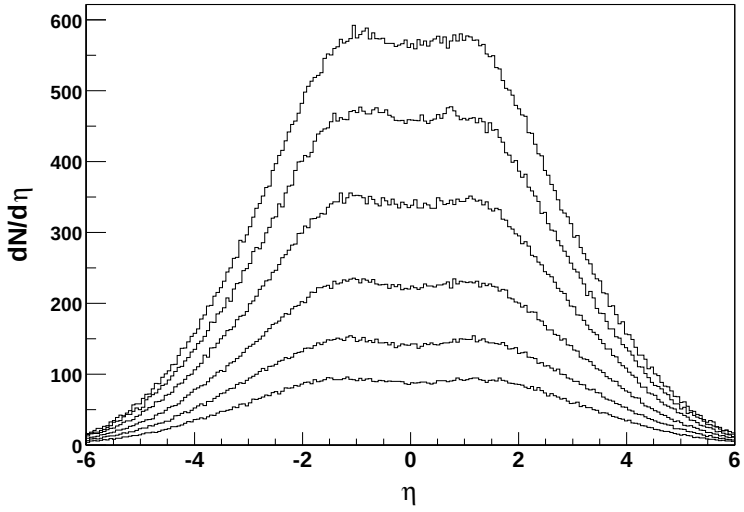

Figure 8.1: Pseudorapidity Distribution by the Hijing Model at $\sqrt{s_{NN}} = 130$ GeV
Each line represents the different centrality selections. From the top to bottom, the corresponding centralities are 0-5%, 5-10%, 10-20%, 20-30%, 30-40% and 40-50%.

central events, this model predicts $dN_{ch}/d\eta|_{\eta=0}$ to be about 550, which is one of the smallest predicted values for charged-particle pseudorapidity density of any of the models. (Since the experimental pseudorapidity density is close to this value, as discussed in a later section, this model is very popular for comparison with data.)

8.1.2 AMPT Model

The AMPT [59] model is a multiphase transport model for relativistic heavy-ion collisions. It utilizes the Hijing model as a source of initial parton distributions. The AMPT model differs from the Hijing model in the evolution of partons by not including energy loss of jets by way of an average stopping power dE/dx. Instead, parton collisions are included explicitly. The partons are hadronized after the proper formation time, and final-state scattering of these hadrons is explicitly included.

Figure 8.2 shows the pseudorapidity distributions based on this model. Since it uses the Hi-

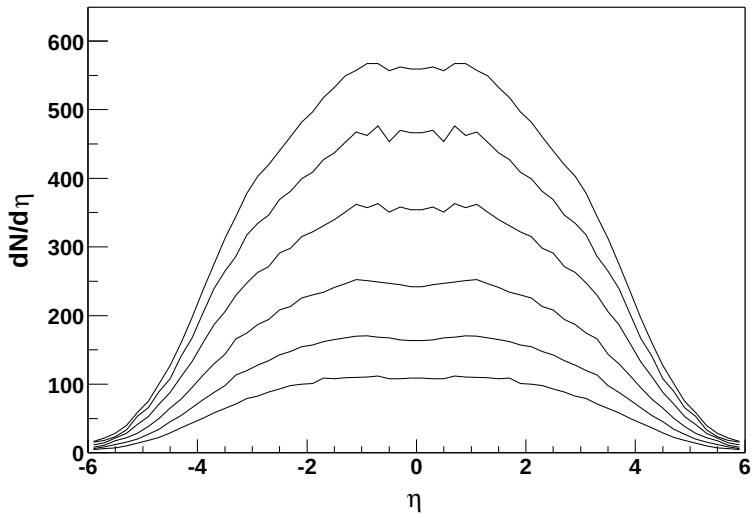

Figure 8.2: Pseudorapidity Distribution by AMPT Model at $\sqrt{s_{NN}} = 130$ GeV
Each line represents the different centrality selections. From the top to bottom, the corresponding centralities are 0-5%, 5-10%, 10-20%, 20-30%, 30-40% and 40-50%.

jing model as input, the AMPT model produces a similar value for the maximum pseudorapidity density. However, the AMPT distribution is noticeably wider than that of the Hijing model due to the inclusion of the final state scattering.

8.1.3 UrQMD Model

UrQMD [60, 61] is a microscopic transport model. It is an ultra-relativistic extension to the quantum molecular dynamic model (QMD) [62]. Instead of using a statistical-type calculation as employed by Hijing, it solves the complex N-body Hamiltonian equation for heavy-ion collisions. By explicitly solving the equation of motion, it tries to find the equation of state for the hot dense matter created by the relativistic heavy-ion collisions.

Figure 8.3 shows the pseudorapidity distribution obtained using this model. For the 0-5%

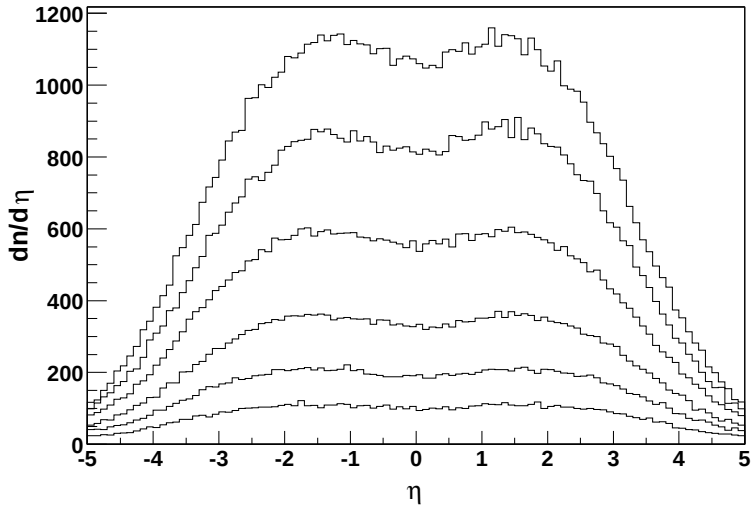

Figure 8.3: Pseudorapidity Distribution by UrQMD Model at $\sqrt{s_{NN}} = 130$ GeV
Each line represents the different centrality selections. From the top to bottom, the corresponding centralities are 0-5%, 5-10%, 10-20%, 20-30%, 30-40% and 40-50%.

central collisions $dN_{ch}/d\eta|_{\eta=0}$ is found to be about 1100. Since the experimental value for this quantity is about 550 (as discussed later), this model predicts far too large a level of particle production.

8.1.4 Saturation Model

The saturation model stems from the idea that the number density of partons can saturate in the relativistic heavy-ion collisions [63, 64]. Since partons are confined in the Lorentz-contracted plane with transverse area $\pi 1.2^2 A^{2/3}$, they will start to interact with each other as their wave functions overlap. In the limiting case, this leads to a particle multiplicity that is proportional to A (the number of participants), and not to the number of collisions or the collision energy.

(See Section 8.2.3 for a discussion of the number of participants and collisions.)

Figure 8.4 shows the pseudorapidity distribution found using this model. It reproduces the

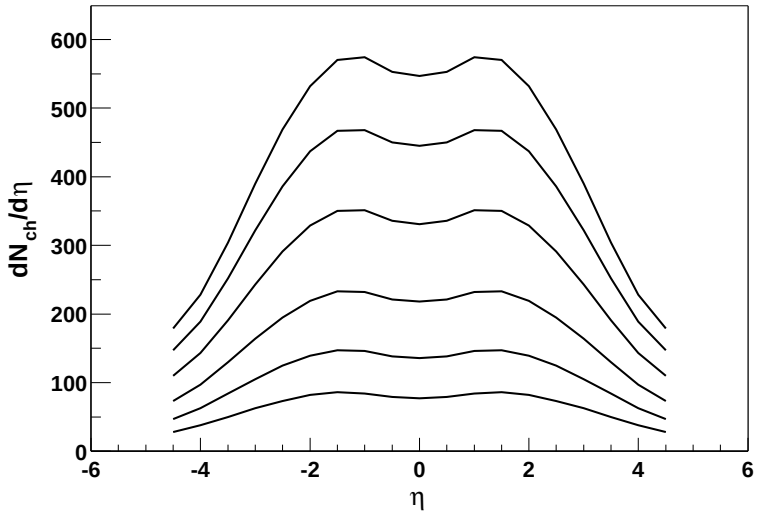

Figure 8.4: Pseudorapidity Distribution by a Saturation Model at $\sqrt{s_{NN}} = 130$ GeV
Each line represents the different centrality selections. From the top to bottom, the corresponding centralities are 0-5%, 5-10%, 10-20%, 20-30%, 30-40% and 40-50%.

overall experimental level of the charged-particle production well. The figure also shows that this model seems to have more pronounced shoulders (or a larger dip at midrapidity) than that of the Hijing model discussed earlier.

8.2 Experimental Charged Particle Production

This section describes the charged-particle pseudorapidity densities measured for Au+Au collisions at $\sqrt{s_{NN}} = 130$ GeV and $\sqrt{s_{NN}} = 200$ GeV. The theoretical calculations are then compared to the experimental results.

8.2.1 Experimental Charged Particle Production of Au+Au Collisions at $\sqrt{s_{NN}} = 130$ GeV and $\sqrt{s_{NN}} = 200$ GeV

During the first experimental program at RHIC, collisions of Au+Au at $\sqrt{s_{NN}} = 130$ GeV were achieved. Using the method discussed earlier in Chapter 6, the charged-particle multiplicities of events were measured by the SiMA, the TMA and the BBC. With the centrality selections

discussed in Section 7.2, the pseudorapidity distribution of charged particles was obtained for different centrality ranges. Figure 8.5 shows the resultant distributions [65].

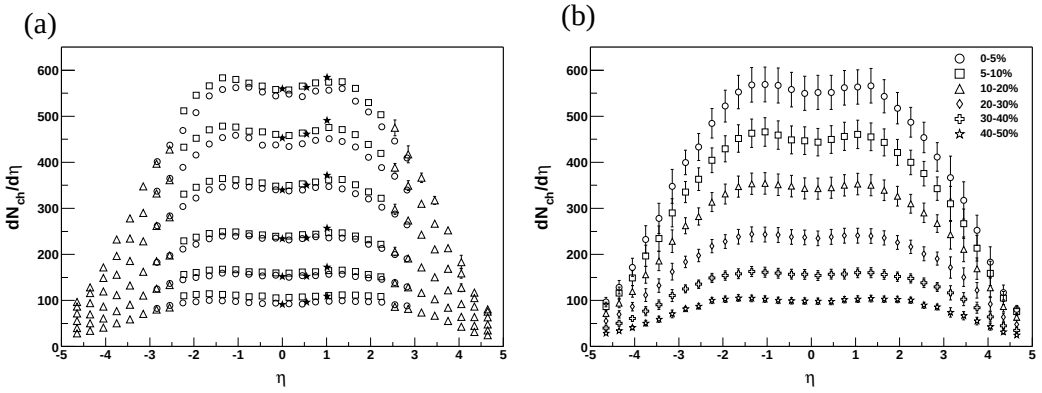

Figure 8.5: Pseudorapidity Distribution of Charged Particles at $\sqrt{s_{NN}} = 130$ GeV (a)Distribution by experimental subsystems: the SiMA (open circles), the TMA (open squares), BBC (open triangles) and the TPM1 (closed stars). From top to bottom, different distributions for the same marker represent the different centrality ranges as given in panel (b). Only statistical errors are shown. (b) The averaged results for the subsystems, weighted by their relative uncertainties, are shown for the different centrality classes. The errors include both systematic and statistical uncertainties.

In Figure 8.5a, it is seen that the three independent detector systems produce reasonably similar pseudorapidity density distributions for a given centrality class. The matching of the distributions by the SiMA and the BBC systems at the pseudorapidity of 2.5 (or -2.5) is very good with no obvious discontinuities. However, although the results from the TMA and the SiMA systems are consistent within systematic uncertainties, it is noticed that the TMA detectors tend to produce larger values of charged-particle density than the SiMA detectors. This might indicate a few things: the first is that the energy calibrations for the TMA detectors were not quite accurate. This is deemed unlikely since the resolution of single minimum-ionizing particles is fairly good for the TMA detectors, which the energy calibration heavily relies on. Another possibility is that the photo-multiplier tubes (PMTs) used for the TMA detectors were not quite linear. This is also unlikely since such a nonlinearity would be expected to decrease the observed particle densities and not to increase their values, as observed. Also, PMT nonlinearity should result in an increased discrepancy between the SiMA and TMA results as more central events are analyzed. This is not seen. Rather, the difference remain about the same for all centrality ranges. The most plausible explanation for the TMA results has to do with background contributions. It is possible that the TMA detectors see particles from background sources such as particles

scattered upstream of the MA in the beam line. If these particles are detected at the same time as the particles from real collisions, they would skew the results. Since the physical size of a scintillator tile is much larger than that of an individual Si strip, such background sources will have a relatively larger effect on the TMA results than the corresponding SiMA results. (The cross sectional areas of one silicon strip and one scintillator tile viewed along the beam axis are 1.2 mm^2 and 600 mm^2, respectively.) Since the Monte Carlo simulation that was used to correct for secondary scattering effects does not include non-collision related processes, this type of background would remain unaccounted in the analysis of the experimental data.

To check the validity of the results, the front time projection chamber of the mid-rapidity spectrometer (TPM1) was also used to measure $dN_{ch}/d\eta$ at three values of η: 0, 0.5 and 1. The reason for using the TPM1 detector is that it has the unique capability, absent in the other detectors used, of being able to count the number of particles directly without having to deduce a particle count from a measured energy loss. Since it can record the tracks of particles in three dimensions, the TPM1 detector can distinguish particles from the event collision vertex and from other sources. Hence, the TPM1 detector is able to check the validity of the analysis procedures used for the other detectors. (For more information about the technique used by the TPM1 detector, a reader should refer to Ref [48].) Figure 8.5a includes the results from the TPM1 detector. It shows that the TPM1 detector agrees well with other three detector systems. However, the systematic error in the TPM1 measurement is not quite sufficient to discriminate between the SiMA and TMA results.

In the second RHIC running period, the accelerator was operated at $\sqrt{s_{NN}} = 200$ GeV for Au+Au collisions. Figure 8.6 shows the results from that run [66]. It is noticed that there exists a small asymmetry in the distribution, most noticeable for the two most central ranges. Since the reaction symmetry requires a symmetric charged-particle distribution about midrapidity, the observed asymmetry must indicate a systematic error. The asymmetry is not evident in the lower energy data, which was analyzed using the same procedures, suggesting the asymmetry might result from a background contamination in the 200 GeV run that is larger than found for the 130 GeV run. However, the lack of directionality in the global detectors prevents a clear identification of the background source.

Since RHIC is currently operated as the highest energy accelerator for heavy-ion collisions, it is of interest to compare the RHIC results with those obtained at lower energy facilities.

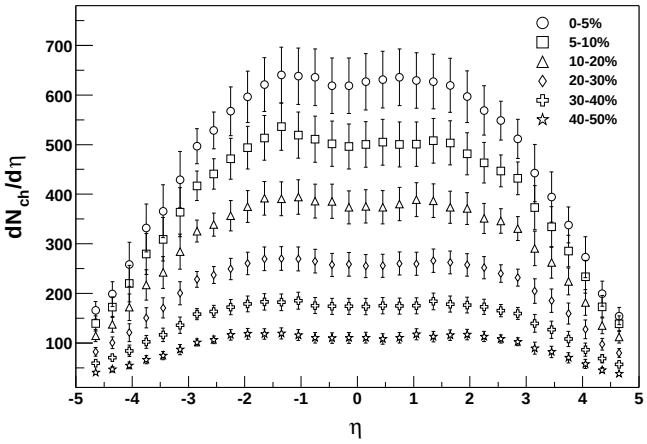

Figure 8.6: Pseudorapidity Distribution of Charged Particles at $\sqrt{s_{NN}} = 200$ GeV

Figure 8.7 shows the dependence of the maximum pseudorapidity density at midrapidity on the center of mass energy for the system. The figure shows how RHIC achieves the highest

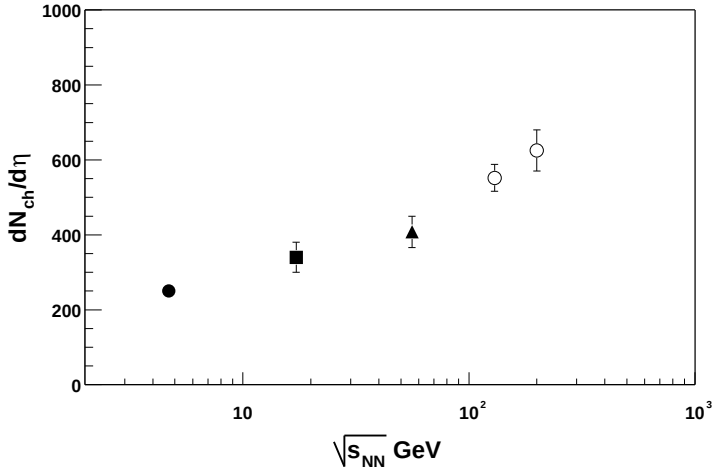

Figure 8.7: Maximum $dN_{ch}/d\eta$ as a function of center of mass energy for Au+Au Collisions The two open circles represent results from this analysis. The closed circle is from the E877 experiment [67]. The closed square is from the NA49 experiment [68]. (Since NA49 was Pb+Pb experiment, the above data is scaled by the expected number of participants.) The closed triangle is from the PHOBOS experiment [69].

pseudorapidity density of charged particles at midrapidity for heavy-ion collisions. Comparing to the Alternating Gradient Synchrotron (AGS) experiments such as E877 [67], the observed density is about 2.5 times larger. RHIC achieves a particle density that is about twice that by the NA49 [68] experiment at the Super Proton Synchrotron (SPS). Using Equation 2.31, the

initial energy density in the RHIC collisions can be estimated as

$$\varepsilon = \frac{.5 \text{ (GeV/c)}}{1.0 \text{ (fm/c)}\ \pi\, 1.2^2 \times 197^{2/3} (\text{fm}^2)} \times \frac{3}{2} \times 625 \tag{8.1}$$

$$\approx 3 \text{ GeV/fm}^3 \tag{8.2}$$

It is assumed that the mean transverse mass of particles and the proper time are 0.5 GeV/c and 1.0 fm/c, respectively. Although this value is lower than originally expected, it still indicates creation of a localized region that is a lot more dense than ordinary nuclear matter ($\varepsilon \approx .14$ GeV/fm^3). Before the RHIC experiments started to report results, an energy density of $\varepsilon \approx 6$ was expected, consistent with earlier values of expected particle densities of $dN_{ch}/d\eta|_{\eta=0} \approx 1200$. It should also be noted that the energy density expression uses the average value for the overlapping area of a nuclear collision; at the center of the nucleus, it is expected that the actual energy density might be much higher than the above value. Furthermore, since this result is derived from 0-5% central events, the use of more central events would clearly increase this energy density. However, for those very central collisions, the uncertainty in the centrality becomes very large. Hence, it is not used in this analysis. With this value of energy density, the initial temperature can be also estimated with Equation 2.94. Assuming the chemical potential is zero, and with $p = \frac{1}{3}\varepsilon$,

$$(kT)^4 = \frac{90\hbar^3 c^3}{37\pi^2} * \frac{\varepsilon}{3} \tag{8.3}$$

$$kT = \left(\frac{90\hbar^3 c^3}{37\pi^2} * \frac{\varepsilon}{3} \right)^{1/4} \tag{8.4}$$

$$T \approx 160 \text{ MeV} \tag{8.5}$$

Therefore, the resultant initial temperature is in the range of values expected to lead to the creation of a QGP (see Section 2.3.3).

Although particle production at midrapidity has gained the greatest attention with the early RHIC data, the overall level of particle production can also be compared with the data for the different energy regions. Figure 8.8 shows the trend of total charged-particle production as a function of the center of mass energy. Since the detector acceptance does not extend to large pseudorapidity, the missing particle yields are estimated from the experimental pseudorapidity distribution, assuming the tail of the pseudorapidity distribution in Figure 8.6 can be extended

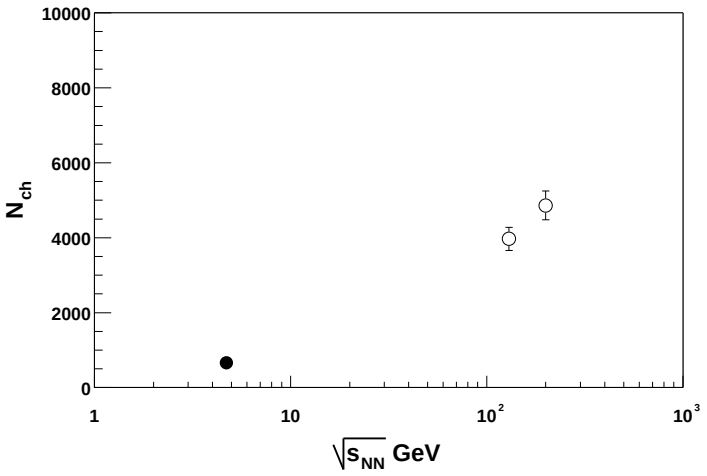

Figure 8.8: Total Charged Particle Production
The two open circles are from this analysis. The closed circle represents the results from E877 [67].

using either a Gaussian or Wood-Saxon shape. The two functional forms produce similar values of the missing charged-particle yields, within 5% of each other, with values of 234 and 226 for the Gaussian and Wood-Saxon shapes, respectively. This translates to an uncertainty of less than 1% in the total charged-particle production. For Figure 8.8, an average of the extrapolated yields based on the two functional forms is used to estimate the total number of charged particles. Comparing to the E877 results at $\sqrt{s_{NN}} = 4.7$ GeV, the present results at $\sqrt{s_{NN}} = 200$ GeV show an increase of 736 % in the total charged-particle production. Since the charged-particle pseudorapidity density at midrapidity only increases by 250%, this indicates that the particle production is increasing more longitudinally than transversely. This is also evident by comparing the $\sqrt{s_{NN}}$ =130 GeV and $\sqrt{s_{NN}}$ =200 GeV data. From the lower to the higher energy, $dN_{ch}/d\eta$ at midrapidity increases by 14 %, while the total number of charged particles increases by 24 %.

8.2.2 Comparisons of Theory to Experimental Results for the Charged-Particle Productions

With no clear signature for the presence of a QGP, progress in relativistic heavy-ion physics requires careful comparisons of theoretical models to experimental data. Figure 8.9 shows the comparison of charged-particle pseudorapidity distributions calculated using the theoretical models discussed previously to the experimental results. In this figure, the UrQMD model has not

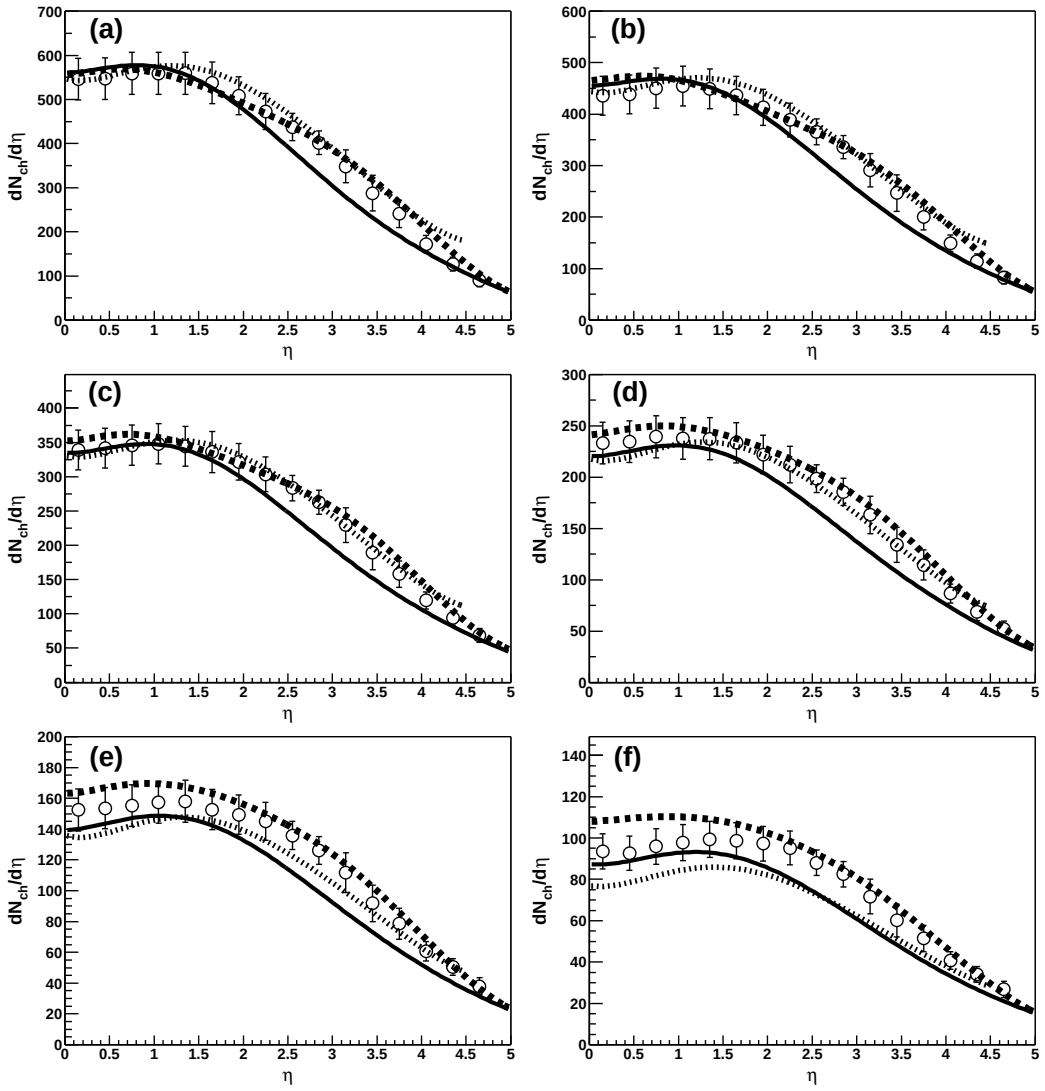

Figure 8.9: Comparison $dN_{ch}/d\eta$ at $\sqrt{s_{NN}}$ =130 GeV
Panels (a) through (f) correspond to the different centrality ranges, in alphabetic order from 0-5%, 5-10%, 10-20%, 20-30%, 30-40% to 40-50%. The open circles represent the experimental values. The solid lines are from the Hijing model. The dash and dot lines are the AMPT and the Saturation models, respectively.

been included since it produces almost twice as large a value at midrapidity as the experimental charged-particle productions. The other models all do a reasonably good job at reproducing the experimental results. The distribution from the Hijing model is somewhat narrower than found experimentally. Particularly, around $\eta = 3$, the gap between the Hijing m8odel and experimental data is fairly large. On the other hand, the final state rescattering mechanism included in the AMPT model seems to increase the width of the baseline Hijing model, and the AMPT distribution is within the systematic errors of the experimental values for almost the entire range of η. The Saturation model also seems to reproduce the experimental results quite accurately. A careful comparison of the Saturation and AMPT models reveals somewhat different shape for their "shoulders" near $\eta = 2$. The Saturation model has a distinct peak at the shoulder, which better resembles to the experimental results than the AMPT model. However, the uncertainty in the experimental result is too large to clearly distinguish between the AMPT and Saturation models.

To explore more carefully the energy dependence of the pseudorapidity distributions, the ratios of $dN_{ch}/d\eta$ from Figure 8.5 and 8.6 have been plotted in Figure 8.10. The figure shows that for all centralities, the ratio remains relatively constant from $\eta = 0$ to $\eta = 2$. Then, it increases for pseudorapidities larger than 2. This clearly indicates that the width of the distribution is getting wider as expected for the larger beam rapidity. Also, for the region between $\eta = 0$ and $\eta = 2$, the ratios for different centralities are very close. The smallest value is 1.09 for 20-30% centralities, and the largest value is 1.16 for 40-50% centralities. This indicates that to obtain the pseudorapidity distribution of $\sqrt{s_{NN}} = 200$ GeV from that of $\sqrt{s_{NN}} = 130$ GeV for an extended range near midrapidity, one simply needs to shift the distribution upward by about 13%. Comparing these ratios with the model calculations, both the AMPT and the Saturation models reproduce the experimental results quite well between $\eta = 0$ and $\eta = 3$. At larger values of pseudorapidity, the AMPT model shows the same pronounced increase in the ratio, whereas the Saturation model shows a smaller increase.

Finally, to compare the shapes of the pseudorapidity distributions between the different centralities, the distributions are divided by the measured number of charged particles. Figure 8.11 shows the results at three different pseudorapidity values: 0, 3 and 4.5. It is seen that as the collisions become more central, a greater fraction of the charged particles is emitted at midrapidity.

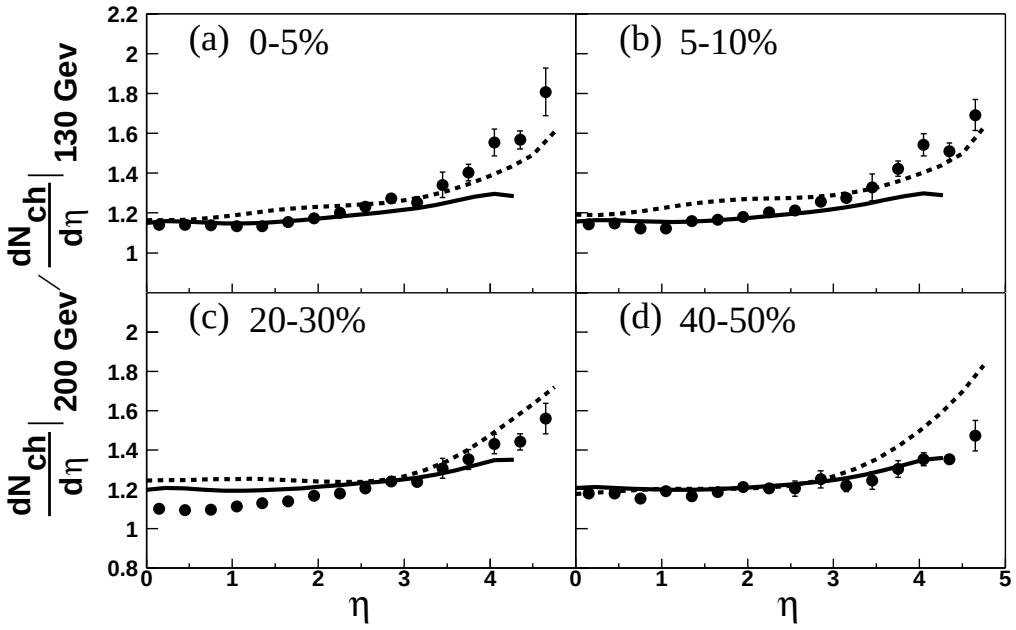

Figure 8.10: Ratio of charge particle productions between $\sqrt{s_{NN}}$ = 200 GeV and $\sqrt{s_{NN}}$ = 130 GeV.
The solid and dotted line represent the Saturation and AMPT models respectively. The experimental data shows only the point-to-point errors.

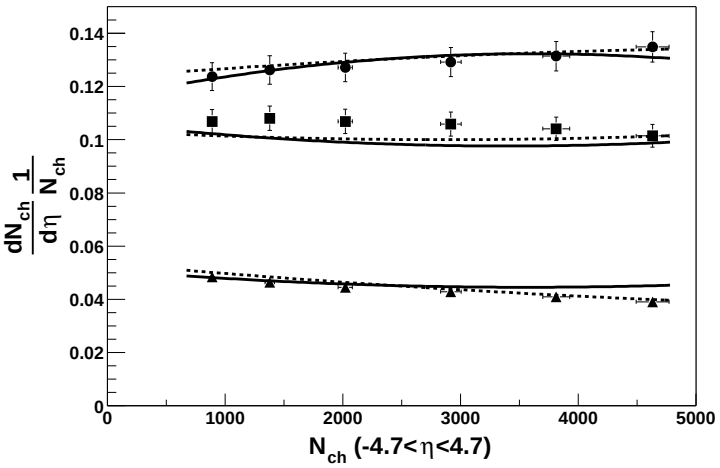

Figure 8.11: Pseudorapidity per total charge at $\sqrt{s_{NN}}$ = 200 GeV/A
The solid and dotted line represent the Saturation and AMPT models respectively. The closed circle, square and triangles represent data at three different value of η:0, 3 and 4.5 respectively. Here, N_{ch} is the measured amount of charged particles within $\eta = -4.7$ and $\eta = 4.7$.

8.2.3 Number of Participants and Collisions

The large number of collisions that nucleons inside the parent nucleus suffer in a single heavy-ion collision is believed to be one of the contributing factors leading to the creation of a QGP. (Here, nucleons that suffer collisions are called participants, whereas the non-participating nucleons are called spectators. The total number of nucleon-nucleon collisions is called the "number of collisions". In the case of collisions between two nuclei of mass number A, the maximum value for the number of participants and spectators is $2A$ while the maximum number of collisions is A^2 if every nucleon of one nucleus collides once with every nucleon in the other nucleus.) To see the effect of the number of collisions, it is necessary to compare the results from heavy-ion collisions with those from pp (or $p\bar{p}$) collisions whose number of participants and collisions are two and one, respectively. Usually the scaling from pp to AA is done based on a the number of participants in the AA collisions. However, there is a problem in that the number of participants is not an experimentally measurable quantity (or, at least, not by the current BRAHMS detectors). At the BRAHMS experiment, the Zero Degree Calorimeter (ZDC) can detect spectator neutrons. In principal, this measurement can be used to deduce the number of participants as the difference of the number of incident nucleons minus the spectator nucleons, estimating the spectator protons based on the measured spectator neutrons. However, the observed number of spectator neutrons is low since some of these neutrons can combine with spectator protons to form ions. These ions would not be detected by the ZDC detector. Furthermore, there is no way, in principle, to measure the number of collisions in a heavy-ion collision.

Since the number of participants and the number of collisions are not experimentally measurable quantities, it is necessary to rely on model calculations for these values. Here, the Hijing model has been used to translate the experimental centralities into the number of participants and collisions. Figure 8.12 shows the dependence of these numbers on impact parameter. The Hijing model calculates these numbers based on the Wounded-Nucleon model. The number of participants saturates as the collisions become more central and reaches a maximum value of 2A. However, at the center of mass energy of $\sqrt{s_{NN}} = 200$ GeV, the number of collisions does not seem to saturate in this model, but rather reaches a maximum value of over 1000 for very central collisions. To obtain the number of participants and collisions that corresponds to the experimental centralities, average values of these numbers from the corresponding centrality bin

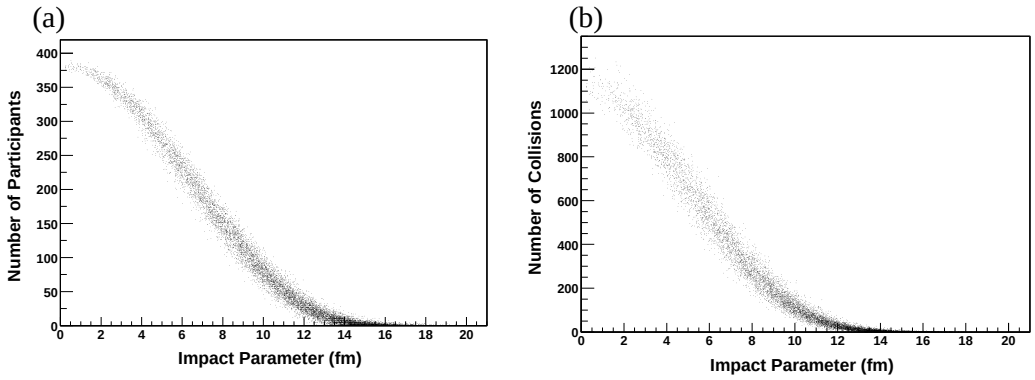

Figure 8.12: A number of participants and collisions by the Hijing model at $\sqrt{s_{NN}} = 200$ GeV (a) and (b) show correlation plots of impact parameter with the number of participants and the number of collisions, respectively.

are obtained from Figure 8.12. The results are tabulated in Table 8.1 and 8.2 at the end of this section.

In the Wounded-Nucleon calculations, nucleons inside a nucleus are distributed to achieve a density profile of Wood-Saxon shape. This leads to two parameters: the radius and the surface thickness of the density distributions. To decide if a nucleon experiences a collision, the nucleon-nucleon cross-section is used, which is also taken as a model parameter. To explore the systematic effects of these parameters on the calculated number of participants and collisions, values of these parameters were changed individually. Figure 8.13 shows the effects of the individual parameters on the calculated values. The value of surface thickness parameter has been measured by electron scattering to be about .535 fm. However, since this value is for the charge density, it might not be identical to that for the nucleon density. The effect of this parameter is obvious from the figure. As the surface thickness parameter increases, the volume of the nucleus becomes larger. Since the density of nucleons in the nucleus then decreases, both the number of participants and collisions decreases. Although the actual value of the surface thickness of a Au ion may not be known, it is not expected to differ from the electron scattering results by more than a few hundredths of a Fermi. From the top two plots, the effect of this parameter within this uncertainty is less than one for the number of participants and about ten for the number of collisions. The effect of the radius parameter in the Wood-Saxon equation is very similar to that of the surface thickness parameter. The value given by electron scattering is 6.38 fm and, again, the effect of this parameter within a reasonable range of values is relatively

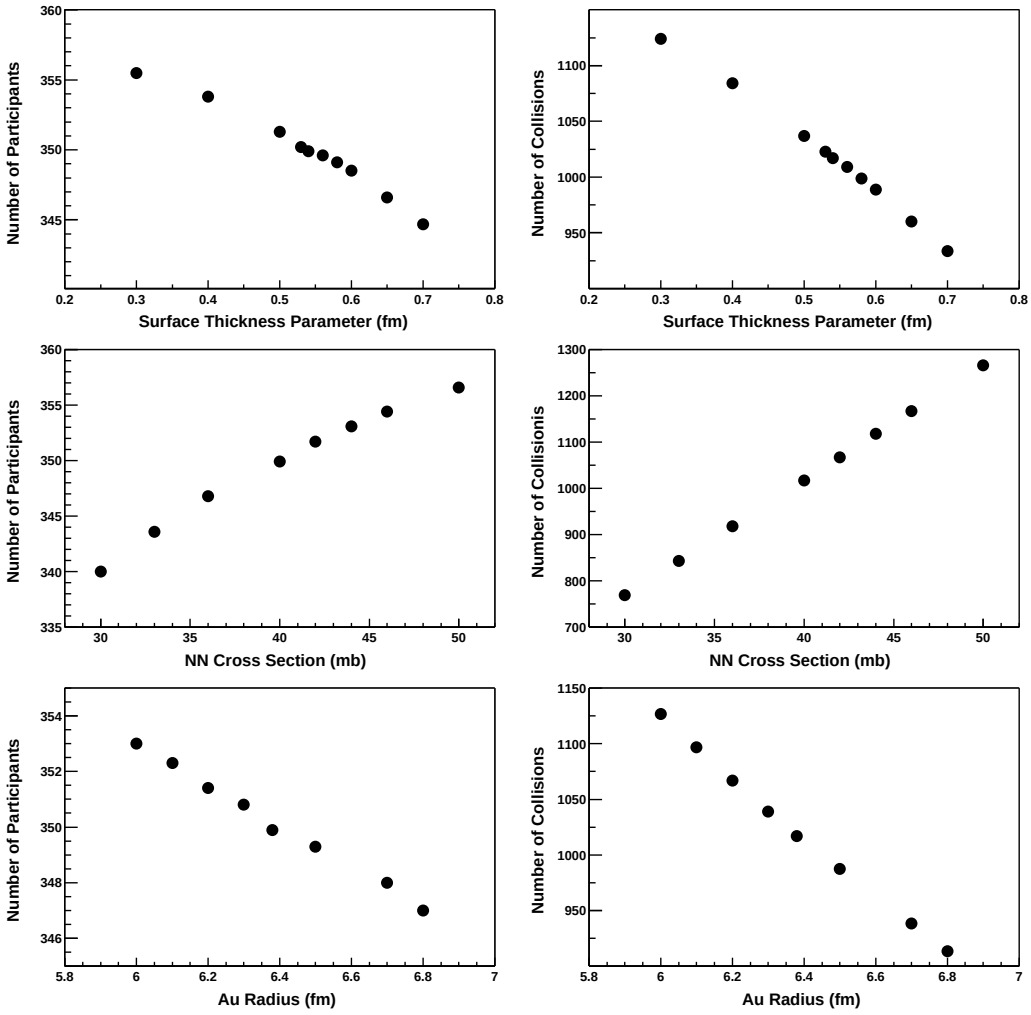

Figure 8.13: Effect of surface thickness, NN cross section and radius on the number of participants and collisions
The reference values of the parameters are: .535 fm for the surface thickness; 40 mb for NN cross section; and 6.38 fm for the radius parameter.

small.

The inelastic cross section of pp and p$\bar{\text{p}}$ has been measured over an extended energy range. From Figure 8.14, it is about 40 mb at the center of mass energy of 200 GeV. The effect of the

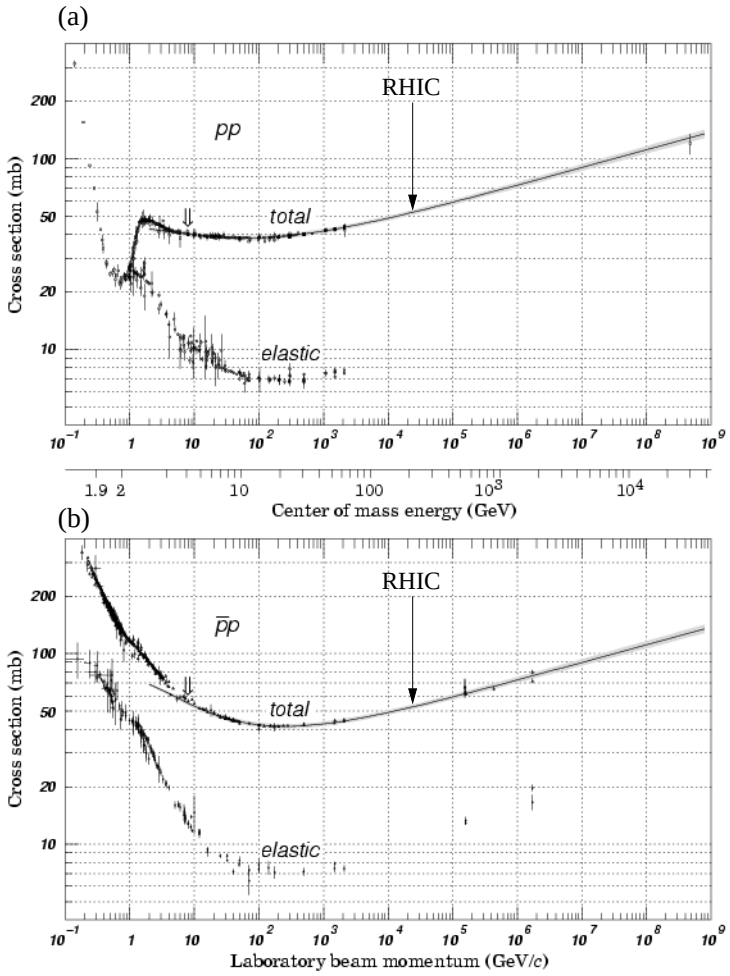

Figure 8.14: (a) pp and (b) p$\bar{\text{p}}$ cross section (Copied from particle Data Book [70])

cross section on the Wounded-Nucleon calculation is quite simple. The larger the cross section, the larger is the chance of collision. Hence, there are more participants and collisions. From the middle two plots in Figure 8.13, one finds that a few percent change in nucleon-nucleon cross section would change the number of participants by less than 1 and the number of collisions by about 20. Therefore, unless the nucleon-nucleon cross section in the heavy-ion collisions differs from the free-particle nucleon-nucleon cross section by a large amount, the calculated number of participants and collisions are not strongly sensitive to this parameter.

With the numbers given by the Hijing model, it is now possible to scale the results of heavy-ion collisions to compare with the results from p$\bar{\text{p}}$ collisions. To scale the results from the heavy-ion collisions, $dN_{ch}/d\eta$ is divided by one half of the number of participants. Figure 8.15 shows these scaled results with the corresponding p$\bar{\text{p}}$ data. The figure shows that there is a 40%

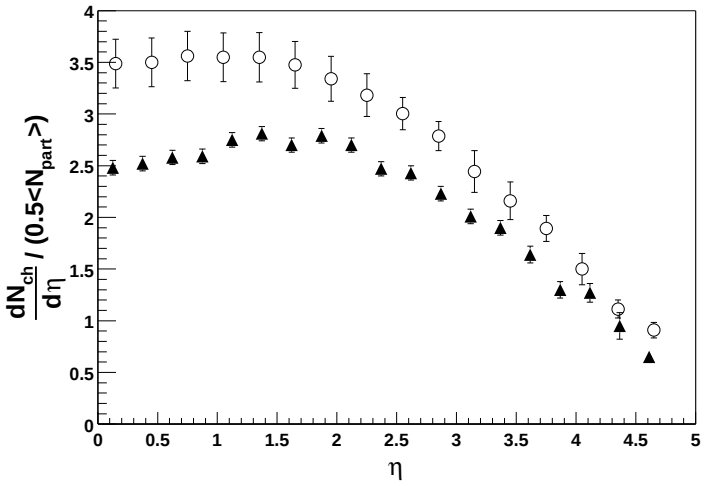

Figure 8.15: Comparison of $dN_{ch}/d\eta$ per participant pair between Au+Au and p$\bar{\text{p}}$ at $\sqrt{s_{NN}}$ = 200 GeV
The open circle represents 0-5% central Au+Au data from this analysis. The closed triangle is from p$\bar{\text{p}}$ data from UA5 experiment [70] at $\sqrt{s_{NN}}$ =200 GeV.

increase in the charged particle production per participant pair from p$\bar{\text{p}}$ to Au+Au collisions at midrapidity, with the enhancement for the heavy-ion collisions remaining relatively constant over the entire range of pseudorapidity at between 30-40%.

Figure 8.16 also shows the scaled values in a similar manner to that used in Figure 8.11 to emphasize the centrality dependence of the pseudorapidity distributions. At midrapidity, more particles are produced per participant nucleon pair as the collisions become more central. At $\eta = 3$, the particle production per participant nucleon pair is almost constant. Whereas at $\eta = 4.5$, it seems to slightly decrease as collisions become more central. Comparing with pp data, at all three pseudorapidity values, more particles are produced per participant pair. (It is noted here that in this figure, both the x-axis and y-axis require estimates of the number of participants, which is not an experimental value. Hence, there may be a systematic uncertainty, particularly for the peripheral collisions, that might affect these slopes. Future measurements with lighter ions at RHIC should address this concern.) It has been suggested that this figure might be used to estimate the fraction of particle productions by the soft and hard scattering

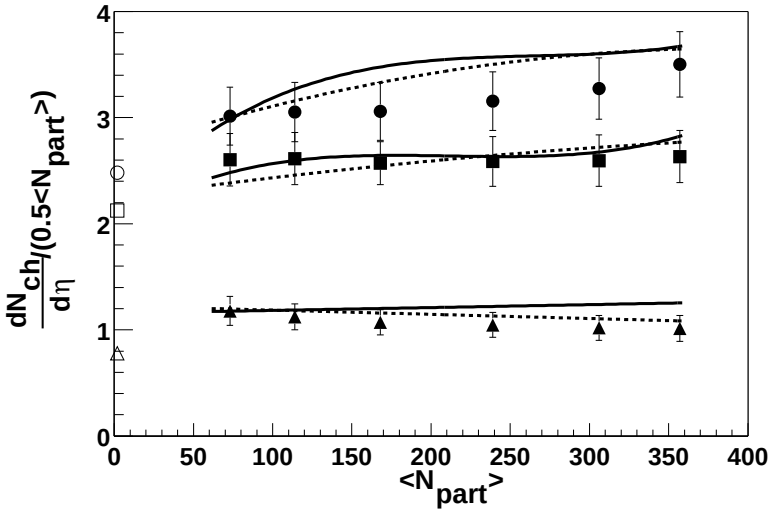

Figure 8.16: Centralities dependence of $dN_{ch}/d\eta$ per participants pair at $\sqrt{s_{NN}} = 200$ GeV The solid and dotted line represent the Saturation and AMPT models respectively. The closed circles, squares and triangles represent data at three different values of η:0, 3 and 4.5 respectively. The open circle, square and triangle symbols represent the PP data from UA5 experiment [70].

processes since these can be related to the number of participants and collisions, respectively [71]. Their fraction is found using the expression

$$\frac{dN_{ch}}{d\eta} = \alpha \cdot \langle N_{part} \rangle + \beta \cdot \langle N_{coll} \rangle \tag{8.6}$$

where $\langle N_{part} \rangle$ and $\langle N_{coll} \rangle$ are the average values of the number of participants and collisions for each experimental centrality range. Using this simple expression, at midrapidity, it is found that $\alpha = 1.26 \pm 0.09 \pm 0.20$ and $\beta = 0.15 \mp 0.04 \mp 0.05$ for $\sqrt{s_{NN}} = 200$ GeV and $\alpha = 1.24 \pm 0.08 \pm 0.20$ and $\beta = 0.12 \mp 0.04 \mp 0.06$ for $\sqrt{s_{NN}} = 130$ GeV, where the first uncertainty assumes a 3% point-to-point error for the $dN_{ch}/d\eta$ values and the second uncertainty results from the $\langle N_{part} \rangle$ and $\langle N_{coll} \rangle$ uncertainties. This indicates the fraction from the hard-scattering mechanism remains almost constant for these two energies. However, this conclusion has to be somewhat questioned because of the heavy reliance on non-experimental values of $\langle N_{part} \rangle$ and $\langle N_{coll} \rangle$. Furthermore, Equation 8.6 might not be adequate in describing the particle production mechanism of heavy-ion collisions.

Similar to Figure 8.7 and 8.8, the energy dependence of the charged-particle production per participant nucleon pair is plotted in Figure 8.17. The Au+Au collisions at $\sqrt{s_{NN}} = 200$ GeV

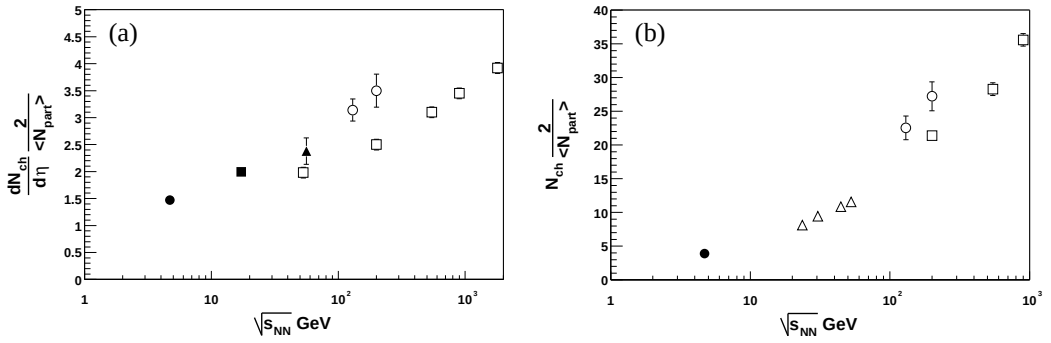

Figure 8.17: Energy dependency of charged particle production per participant nucleon pair. (a) Pseudorapidity density per participant nucleon pair at midrapidity. (b) Total number of charged particles per participant pair. The open circles represent results from this analysis. The closed circle is Au+Au data from the E877 experiment [67]. The closed square is Pb+Pb data from the NA49 experiment [68]. The closed triangle is from the PHOBOS experiment [69]. For $p\bar{p}$ collisions, the open squares are from the UA5 experiment [70], and the open triangles are from the ISR experiment [70].

produce more charged particles per participant nucleon pair than the $p\bar{p}$ collisions by 40% at midrapidity. From the left figure, it seems that there are two different trends: one for $p\bar{p}$ collisions and one for heavy-ions. The plot of total number of charged particles per participant pair also shows similar results. For convenience, Tables 8.1 and 8.2 summarize the above results.

Finally, another interesting phenomenon is seen for the fragmentation region of the reaction by shifting the pseudorapidity distribution scaled by the number of participant pairs by the beam rapidity. Figure 8.18 shows these pseudorapidity distributions for different centralities, energies and heavy-ions reactions. As clearly seen, at the pseudorapidity that is close to the beam rapidity, $dN_{ch}/d\eta$ per participant nucleon pair is almost identical for the different systems. This behavior has been labeled as a "limiting fragmentation mechanism" [72] and is believed to correspond to a saturation of the excitations of a beam nucleus by a Lorentz-contracted target nucleus in the rest frame of the beam nucleus [73].

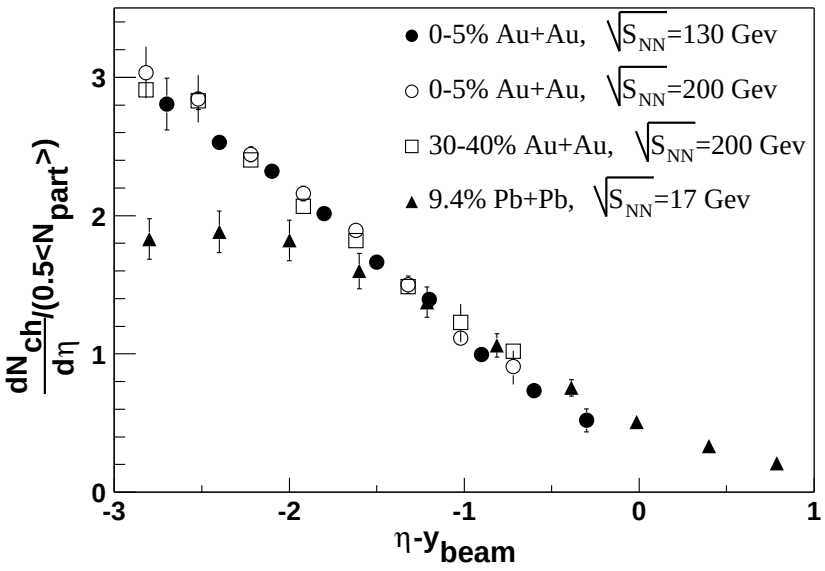

Figure 8.18: Limiting fragmentation behavior
Only few systematic errors are shown for clarity.

Table 8.1: Au+Au Multiplicity Results at $\sqrt{s_{NN}} = 130$ GeV
N_{ch} is the total charge within $|\eta| < 4.7$

Centrality	$\eta = 0$	$\eta = 1.5$	$\eta = 3.0$	$\eta = 4.5$	N_{ch}	$\langle N_{part} \rangle$	$\langle N_{coll} \rangle$
0-5%	553±36	554±37	372±37	107±15	3860±300	352	820
5-10%	447±29	454±31	312±36	94±13	3180±250	299	630
10-20%	345±23	348±25	243±27	79±10	2470±190	235	431
20-30%	237±16	239±16	172±18	59±8	1720±130	165	259
30-40%	156±11	159±11	117±13	43±6	1160±90	114	152
40-50%	98±7	104±7	77±9	30±4	750±60	75	85

Table 8.2: Au+Au Multiplicity Results at $\sqrt{s_{NN}} = 200$ GeV
N_{ch} is the total charge within $|\eta| < 4.7$

Centrality	$\eta = 0$	$\eta = 1.5$	$\eta = 3.0$	$\eta = 4.5$	N_{ch}	$\langle N_{part} \rangle$	$\langle N_{coll} \rangle$
0-5%	625±55	627±54	470±44	181±22	4630±370	357	1000
5-10%	501±44	515±48	397±37	156±18	3810±300	306	785
10-20%	377±33	386±35	309±28	125±14	2920±230	239	552
20-30%	257±23	267±23	216±17	90±10	2020±160	168	335
30-40%	174±16	182±16	149±14	64±7	1380±110	114	192
40-50%	110±10	115±11	95±9	43±5	890±70	73	103

Chapter 9

Summary and Conclusions

In an effort to create a Quark-Gluon Plasma (QGP), the Relativistic Heavy-ion Collider (RHIC) has been operated at its currently highest energy to achieve Au+Au collisions. It is believed that the presence of many nucleon-nucleon collisions involved in a single relativistic heavy-ion collision is one of the key elements needed to produce a QGP. To characterize global features of such a collision, at the BRAHMS experiment, the charged-particle productions from Au+Au collisions at the center of mass energy of $\sqrt{s_{NN}}$ = 130 GeV and $\sqrt{s_{NN}}$ = 200 GeV are measured with three independent detector systems: the Silicon Strip Detector Array (SiMA), the Scintillation Tile Detector Array (TMA) and the Beam-Beam Counter arrays (BBC).

The detailed description of the SiMA, the TMA and the BBC detectors are discussed in Chapter 4. These detector systems sense the passage of a charged particle with associated energy loss in the detector element. With the calibration procedure presented in Chapter 6, it is shown that these detector systems are capable of measuring the accurate number of charged particles in heavy-ion collisions. To categorize the severity of a heavy-ion collision, the observed number of charged particles is used to select an event class called centrality. In this analysis, six centrality ranges, 0-5%, 5-10%, 10-20%, 20-30%, 30-40% and 40-50%, are identified. Then, for each centrality range, the pseudorapidity distribution of charged particles has been measured using the SiMA, the TMA and the BBC detectors. For 0-5% central collisions, the observed charged-particle pseudorapidity densities at midrapidity, $dN_{ch}/d\eta|_{\eta=0}$, were 553±36 and 625±55 at $\sqrt{s_{NN}}$ = 130 GeV and $\sqrt{s_{NN}}$ = 200 GeV, respectively, while their total integrated number of charged particles within $|\eta| < 4.7$ were 3860±300 and 4630±370, respectively. At $\sqrt{s_{NN}}$ =

200 GeV, this pseudorapidity density leads to an energy density of approximately 3 GeV/fm^3 and temperature of about 160 MeV, which is in line with the expected conditions needed for the production of a quark-gluon plasma.

Without a single clear signature of the creation of a QGP, the comparison between theoretical model calculations and the experimental results are crucial in the study of a relativistic heavy-ion collision. Hence, three theoretical models are considered for comparison: the Hijing, the AMPT and the Saturation models. The Hijing model provids an accurate prediction for the charged-particle production at midrapidity. However, its charged-particle pseudorapidity distribution is narrower than the observed distribution. The AMPT model, which uses the Hijing model as input, reproduces the observed charged-particle distribution within the experimental uncertainties. The inclusion of final state rescattering seems to make the distribution wider than that of Hijing. The Saturation model, which is based on the assumption that the number density of partons in a relativistic heavy-ion collision can be saturated, also reproduces the experimental distributions quite accurately. However, the experimental uncertainties are too large to distinguish between the AMPT and the Saturation models.

Furthermore, to compare the mechanism of Au+Au collisions with that of p$\bar{\text{p}}$ collisions, the number of participant nucleon pairs is introduced as a scaling factor. It is shown that at $\sqrt{s_{NN}} = 200$ GeV, $dN_{ch}/d\eta|_{\eta=0}$ per participant nucleon pair from the central Au+Au collisions had 40% enhancement over that from p$\bar{\text{p}}$ collisions. The concept of the number of participant nucleon pairs also naturally introduces the concept of the number of nucleon-nucleon collisions involved in a single heavy-ion collision. It is suggested that with the use of these parameters, the fraction of particle production from soft and hard interactions can be estimated by the following expression: $dN_{ch}/d\eta = \alpha \cdot \langle N_{part} \rangle + \beta \cdot \langle N_{coll} \rangle$ where $\langle N_{part} \rangle$ and $\langle N_{coll} \rangle$ are the average values of the number of participants and collisions for each centrality range. Using this expression, at midrapidity, it is found that $\alpha = 1.26 \pm 0.09 \pm 0.20$ and $\beta = 0.15 \mp 0.04 \mp 0.05$ for $\sqrt{s_{NN}} = 200$ GeV and $\alpha = 1.24 \pm 0.08 \pm 0.20$ and $\beta = 0.12 \mp 0.04 \mp 0.06$ for $\sqrt{s_{NN}} = 130$ GeV. However, since neither $\langle N_{part} \rangle$ or $\langle N_{coll} \rangle$ is an experimentally observed quantity, this conclusion must be somewhat questioned. The future RHIC experiment with lighter nuclei may reduce some of these uncertainties.

Obviously, the measurement of charged particle production alone can not confirm the creation of a QGP from a heavy-ion collision. However, the estimated values of the initial energy

density and temperature created by Au+Au collisions are in line with the expected conditions for creation of a QGP. Hopefully, many additional results such as a nuclear flow signal and a suppression of J/Ψ particles will provide enough information to confirm the creation of this elusive matter.

Reference

[1] J. J. Thomson, Phil. Mag. **44**, 293 (1897).

[2] H. Nagaoka, Phil. Mag. **7**, 445 (1905).

[3] J. J. Thomson, Phil. Mag. **7**, 237 (1904).

[4] J. J. Thomson, Phil. Mag. **11**, 769 (1906).

[5] E. Rutherford, Phil. Mag. **21**, 669 (1911).

[6] E. Rutherford, Phil. Mag. **27**, 488 (1914).

[7] H. Geiger and E. Marsden, Proc. Roy. Soc **82**, 495 (1909).

[8] H. Geiger and E. Marsden, Phil. Mag. **25**, 1 (1913).

[9] N. Bohr, Phil. Mag. **26**, 1 (1913).

[10] J. Chadwick, Nature **129**, 312 (1932).

[11] J. Chadwick, Proc. Roy. Soc. A **136**, 692 (1932).

[12] P. Dirac, *Principles of Quantum Mechanis* (Oxfrod University Press, Oxford, England, 1930).

[13] C. D. Anderson, Phys. Rev. **43**, 491 (1933).

[14] H. Yukawa, Proc. Phys.-Math. Soc. Japan **17**, 48 (1935).

[15] C. M. G. Lattes *et al.*, Nature **159**, 694 (1947).

[16] M. Gell-Mann, Phys. Rev. **125**, 1067 (1962).

[17] Y. Ne'eman, Nucl. Phys **26** (1961).

[18] M. Gell-Mann, Phys. Lett. **8**, 214 (1964).

[19] D. Coward *et al.*, Phys. Rev. Lett. **20**, 292 (1968).

[20] D. Coward *et al.*, Phys. Rev. Lett. **23**, 930 (1969).

[21] D. J. Gross and F. Wilczek, Phys. Rev. Lett. **30**, 1343 (1973).

[22] J. C. Collins and M. J. Perry, Phys. Rev. Letters **34**, 1353 (1975).

[23] B. A. Freedman and L. D. McLerran, Phys. Rev. D **16**, 1130 (1977).

[24] P. K. R. Anishetty and L. McLerran, Phys. Rev. D **22**, 2793 (1980).

[25] J. D. Bjorken, Phys. Rev. D **27**, 140 (1983).

[26] M. Gyulassy and T. Matsui, Phys. Rev. D **29**, 419 (1984).

[27] J. R. O. H. W. Lewis and S. A. Wouthuysen, Phys. Rev. **73**, 127 (1948).

[28] W. Heisenberg, Nature **164**, 65 (1949).

[29] J. J. Loard, J. Fainberg, and M. Schein, Phys. Rev. **80**, 970 (1950).

[30] R. L. Jaffe, W. Busza, F. Wilczek, and J. Sandweiss, Rev. Mod. Phys. **72**, 1125 (2000).

[31] A. S. Goldhaber, Phys. Rev. Lett. **35**, 748 (1975).

[32] C.-Y. Wong, *Introduction to High-Energy Heavy-Ion Collisions* (World Scientific, Singapore, 1994).

[33] G. B. Arfken and H. J. Weber, *Mathematical Methods for Physicists* (Academic Press, Sandiego, 1995).

[34] M. Abramowitz and I. A. Stegun, *Handbook of Mathematical Functions* (Dover, New York, 1972).

[35] A. Bialas, M. Blesynski, and W. Czyz, Nucl. Phys. B **111**, 461 (1976).

[36] U. Becker *et al.*, Phys. Rev. Lett. **37**, 1731 (1976).

[37] T. Abbott *et al.*, Phys. Rev. Lett. **66**, 1567 (1991).

[38] D. Dekkers *et al.*, Phys. Rev. **137**, B962 (1965).

[39] S. Nagamiya *et al.*, Nucl. Phys. A **544**, 5 (1992).

[40] E. Eichten, K. Gottried, T. Kinoshita, K. D. Lane, and T. M. Yan, Phys. Rev. D **21**, 203 (1980).

[41] D. Gross, R. D. Pisarski, and L. G. Yaffe, Rev. Mod. Phys. **53**, 43 (1981).

[42] T. Matsui and H. Satz, Phys. Lett. B **178**, 416 (1986).

[43] R. Hanbury-Brown and R. Q. Twiss, Nature **178**, 1046 (1956).

[44] L. Hove, Z. Phys. **C21**, 93 (1983).

[45] M. Gyulassy, Nucl. Phys. **A418**, 59 (1984).

[46] R. C. HWA, *Quark Gluon Plasma* (World Scientific Publication, Singapore, 1990).

[47] S. Jeon and V. Koch, Phys. Rev. Lett. **85**, 2076 (2000).

[48] B. H. Samset, Vertex determination in the BRAHMS experiment and measurements of centrality dependent charged particle production in au-au collision at $\sqrt{s_{NN}} = 130$ GeV, Master's thesis, University of Oslo, 2001.

[49] K. Ashktorab *et al.*, BRAHMS experiment at RHIC, to be published, 2002.

[50] L. Landau, J. Phys. U.S.S.R. **8**, 201 (1944).

[51] T. F. J. Bogart, *Laplace Transforms and Control Systems Theory for Technology* (Wiley, New York, 1982).

[52] R. Debbe, Y. K. Lee, and F. Videbaek, Plastic scintillator centrality detector for BRAHMS, to be published., 2002.

[53] W. R. Leo, *Techniques for Nuclear and Particle Physics Experiments* (Springer, New York, 1987).

[54] F. D. Brooks, Nucl. Instrum. Methods **162**, 477 (1979).

[55] Y. Blyakhman, *Beam-Beam Counters and Charged Particle Multiplicity in the BRAHMS Experiment at RHIC*, PhD thesis, New York University, 2001.

[56] M. Gyulassy and X.-N. Wang, LBL Report **34246** (1997).

[57] M. Gyulassy and X.-N. Wang, Phys. Rev. D **44**, 3501 (1991).

[58] K. Kajantie, P. V. Landshoff, and J. Lindfors, Phys. Rev. Lett. **59**, 2527 (1987).

[59] Z. wei Lin *et al.*, Phys. Rev. C **64**, 011902 (2001).

[60] S. A. Bass *et al.*, Prog. Part. Nucl. Phys **41**, 225 (1998).

[61] M. Bleicher *et al.*, J. Phys. G: Part. Phys. **25**, 1859 (1999).

[62] J. Aichelin and H. Stocker, Phys. Lett. B **176**, 14 (1986).

[63] D. Kharzeev and E. Levin, Phys. Lett. B **523**, 79 (2001).

[64] D. Kharzeev and M. Nardi, Phys. Lett. B **507**, 121 (2001).

[65] I. Bearden *et al.*, Phys. Lett. B **523**, 227 (2001).

[66] I. Bearden *et al.*, Phys. Rev. Lett. **88**, 202301 (2002).

[67] J. Barrette *et al.*, Phys. Rev. C **51**, 3309 (1995).

[68] J. Bachler *et al.*, Nucl. Phys, A **661**, 45 (1999).

[69] B. B. Back *et al.*, Phys. Rev. Lett **85**, 3100 (2000).

[70] D. E. Groom *et al.*, Euro Phys Jour **C15**, 1 (2000).

[71] K. Adcox *et al.*, Phys. Rev. Lett **88**, 022302 (2002).

[72] P. Deines-Jones *et al.*, Phys. Rev. C **62**, 014903 (2000).

[73] J. Benecke, T. T. Chou, C. N. Yang, and Y. E, Phys Rev. **188**, 2159 (1969).

Appendix A

Proof of Properties of Angular Function

A.1 $-i\hat{\sigma}\cdot\nabla = -i\hat{\sigma}\cdot\hat{r}\frac{\partial}{\partial r} + i\hat{\sigma}\cdot\hat{r}\frac{\hat{\sigma}\cdot\mathbf{L}}{\hbar r}$

To prove this equation, consider the following cross product in the component form:

$$\begin{aligned}
\frac{1}{r^2}\left[\mathbf{r}\times\mathbf{r}\times\nabla\right]_i &= \frac{1}{r^2}\epsilon_{ijk}r_j\left(\mathbf{r}\times\nabla\right)_k && \text{(A.1)}\\
&= \frac{1}{r^2}\epsilon_{ijk}r_j\epsilon_{klm}r_l\partial_m && \text{(A.2)}\\
&= \frac{1}{r^2}\epsilon_{ijk}\epsilon_{klm}r_jr_l\partial_m \quad . && \text{(A.3)}
\end{aligned}$$

By using the relation $\epsilon_{ijk}\epsilon_{ilm} = \delta_{jl}\delta_{km} - \delta_{jm}\delta_{kl}$ and $\epsilon_{ijk} = \epsilon_{jki} = \epsilon_{kij}$, the above equation becomes

$$\begin{aligned}
\frac{1}{r^2}\left[\mathbf{r}\times\mathbf{r}\times\nabla\right]_i &= \frac{1}{r^2}\epsilon_{kij}\epsilon_{klm}r_jr_l\partial_m && \text{(A.4)}\\
&= \frac{1}{r^2}\left(\delta_{il}\delta_{jm} - \delta_{im}\delta_{jl}\right)r_jr_l\partial_m && \text{(A.5)}\\
&= \frac{1}{r^2}\left(r_jr_i\partial_j - r_jr_j\partial_i\right) && \text{(A.6)}\\
&= \frac{1}{r^2}\left(r_i\mathbf{r}\cdot\nabla - r^2\nabla_i\right) \quad . && \text{(A.7)}
\end{aligned}$$

With $\mathbf{L} = \mathbf{r} \times \mathbf{p} = \mathbf{r} \times (-i\hbar\nabla)$, solving for ∇_i gives

$$\begin{aligned} \nabla_i &= \frac{r_i}{r}\frac{\partial}{\partial r} - \frac{1}{r^2}\left[\mathbf{r} \times \mathbf{r} \times \nabla\right]_i & \text{(A.8)} \\ &= \frac{r_i}{r}\frac{\partial}{\partial r} - \frac{1}{r^2}\left(\mathbf{r} \times \frac{\mathbf{L}}{-i\hbar}\right)_i & \text{(A.9)} \\ &= \frac{r_i}{r}\frac{\partial}{\partial r} - i\frac{1}{\hbar r^2}\left(\mathbf{r} \times \mathbf{L}\right)_i \quad . & \text{(A.10)} \end{aligned}$$

Hence

$$-i\hat{\sigma} \cdot \nabla = -i\hat{\sigma} \cdot \hat{r}\frac{\partial}{\partial r} - \frac{1}{\hbar r^2}\hat{\sigma} \cdot (\mathbf{r} \times \mathbf{L}) \quad . \tag{A.11}$$

Now, by using the Pauli's matrix relationship, $\sigma_i\sigma_j = \delta_{ij} + i\epsilon_{ijk}\sigma_k$ and noting $\mathbf{r} \cdot \mathbf{L} = 0$, the last term of equation A.11 can be modified:

$$\begin{aligned} \hat{\sigma} \cdot (\mathbf{r} \times \mathbf{L}) &= \sigma_i \left(\mathbf{r} \times \mathbf{L}\right)_i & \text{(A.12)} \\ &= \sigma_i \epsilon_{ijk} r_j L_k & \text{(A.13)} \\ &= \epsilon_{jki} \sigma_i r_j L_k & \text{(A.14)} \\ &= -i\left(\sigma_j\sigma_k - \delta_{jk}\right) r_j L_k & \text{(A.15)} \\ &= -i\left(\hat{\sigma} \cdot \mathbf{r}\, \hat{\sigma} \cdot \mathbf{L} - \mathbf{r} \cdot \mathbf{L}\right) & \text{(A.16)} \\ &= -i\hat{\sigma} \cdot \mathbf{r}\, \hat{\sigma} \cdot \mathbf{L} \quad . & \text{(A.17)} \end{aligned}$$

Therefore,

$$-i\hat{\sigma} \cdot \nabla = -i\hat{\sigma} \cdot \hat{r}\frac{\partial}{\partial r} + i\hat{\sigma} \cdot \hat{r}\frac{\hat{\sigma} \cdot \mathbf{L}}{\hbar r} \quad . \tag{A.18}$$

A.2 $\hbar\hat{\sigma} \cdot \mathbf{L}\Omega_{jlm}$ and $\hbar\hat{\sigma} \cdot \mathbf{L}\Omega_{jl'm}$

From the definition of total angular momentum,

$$\mathbf{J} = \mathbf{L} + \mathbf{S} \quad . \tag{A.19}$$

Then,

$$\begin{aligned} \mathbf{J}^2 &= (\mathbf{L}+\mathbf{S})^2 && \text{(A.20)} \\ &= \left(\mathbf{L}+\frac{\hbar}{2}\hat{\sigma}\right)^2 && \text{(A.21)} \\ &= \mathbf{L}^2+\left(\frac{\hbar}{2}\hat{\sigma}\right)^2+2\mathbf{L}\cdot\left(\frac{\hbar}{2}\hat{\sigma}\right) \quad . && \text{(A.22)} \end{aligned}$$

Applying $\hbar\mathbf{L}\cdot\hat{\sigma}$ to Ω_{jlm} gives

$$\begin{aligned} \hbar\mathbf{L}\cdot\hat{\sigma}\,\Omega_{jlm} &= \left\{\mathbf{J}^2-\mathbf{L}^2-\left(\frac{\hbar}{2}\hat{\sigma}\right)^2\right\}\Omega_{jlm} && \text{(A.23)} \\ &= \left\{j\,(j+1)-l\,(l+1)-\frac{1}{2}\left(\frac{1}{2}+1\right)\right\}\hbar\Omega_{jlm} \quad . && \text{(A.24)} \end{aligned}$$

For $j=l+\frac{1}{2}$,

$$\begin{aligned} j\,(j+1)-l\,(l+1)-\frac{3}{4} &= \left(l+\frac{1}{2}\right)\left(l+\frac{3}{2}\right)-l\,(l+1)-\frac{3}{4} && \text{(A.25)} \\ &= l \quad . && \text{(A.26)} \end{aligned}$$

For $j=l-\frac{1}{2}$,

$$\begin{aligned} j\,(j+1)-l\,(l+1)-\frac{3}{4} &= \left(l-\frac{1}{2}\right)\left(l+\frac{1}{2}\right)-l\,(l+1)-\frac{3}{4} && \text{(A.27)} \\ &= -l-1 \quad . && \text{(A.28)} \end{aligned}$$

Hence,

$$\hbar\mathbf{L}\cdot\hat{\sigma}\,\Omega_{jlm}=\begin{cases} l\,\hbar\Omega_{jlm} & for \quad j=l+\frac{1}{2} \\ (-l-1)\;\hbar\Omega_{jlm} & for \quad j=l-\frac{1}{2} \end{cases} \quad . \qquad \text{(A.29)}$$

For $\hbar\hat{\sigma}\cdot\mathbf{L}\Omega_{jl'm}$, use l' in equation A.24 with equation 2.44.

$$\hbar\mathbf{L}\cdot\hat{\sigma}\,\Omega_{jl'm}=\left\{j\,(j+1)-l'\,(l'+1)-\frac{1}{2}\left(\frac{1}{2}+1\right)\right\}\hbar\Omega_{jl'm} \quad . \qquad \text{(A.30)}$$

For $j = l + \frac{1}{2}$,

$$j\,(j+1) - l'\,(l'+1) - \frac{3}{4} = \left(l+\frac{1}{2}\right)\left(l+\frac{3}{2}\right) - (l+1)\,(l+2) - \frac{3}{4} \tag{A.31}$$

$$= -l-2 \quad . \tag{A.32}$$

For $j = l - \frac{1}{2}$,

$$j\,(j+1) - l'\,(l'+1) - \frac{3}{4} = \left(l-\frac{1}{2}\right)\left(l+\frac{1}{2}\right) - (l-1)\,l - \frac{3}{4} \tag{A.33}$$

$$= l-1 \quad . \tag{A.34}$$

Hence,

$$\hbar\mathbf{L}\cdot\hat{\sigma}\;\Omega_{jl'm} = \begin{cases} (-l-2)\,\hbar\Omega_{jl'm} & for \quad j = l+\frac{1}{2} \\ (l-1)\,\hbar\Omega_{jl'm} & for \quad j = l-\frac{1}{2} \end{cases} \quad . \tag{A.35}$$

Using the equation 2.53, the previous equation A.29 and A.35 can be written as

$$\hbar\mathbf{L}\cdot\hat{\sigma}\Omega_{jlm} = (-\kappa-1)\,\hbar\Omega_{jlm} \quad , \text{ and} \tag{A.36}$$

$$\hbar\mathbf{L}\cdot\hat{\sigma}\Omega_{jl'm} = (\kappa-1)\,\hbar\Omega_{jl'm} \quad . \tag{A.37}$$

Or, with the equation 2.54:

$$\hbar\mathbf{L}\cdot\hat{\sigma}\,\Upsilon_{\kappa m} = (-\kappa-1)\,\hbar\Upsilon_{\kappa m} \quad , \text{ and} \tag{A.38}$$

$$\hbar\mathbf{L}\cdot\hat{\sigma}\,\Upsilon_{-\kappa m} = (\kappa-1)\,\hbar\Upsilon_{-\kappa m} \quad . \tag{A.39}$$

A.3 $\hat{\sigma}\cdot\hat{r}\Omega_{jlm} = -\Omega_{jl'm}$

Look at commutation relation of J_i and P with $\hat{\sigma}\cdot\hat{r}$. For $J_i = L_i + S_i$,

$$[L_i,\ \hat{\sigma}\cdot\hat{r}] = \left[-i\hbar\epsilon_{ijk}r_j\partial_k,\ \frac{1}{r}\sigma_m r_m\right] \tag{A.40}$$

$$= -\frac{i\hbar}{r}\epsilon_{ijk}r_j\,[\partial_k,\ \sigma_m r_m] \tag{A.41}$$

$$= -\frac{i\hbar}{r}\epsilon_{ijk}r_j\sigma_k \quad . \tag{A.42}$$

$$
\begin{aligned}
[S_i,\ \hat{\sigma}\cdot\hat{r}] &= \left[\frac{\hbar}{2}\sigma_i,\ \frac{1}{r}\sigma_j r_j\right] && \text{(A.43)}\\
&= \frac{\hbar}{2r}\left[\sigma_i,\ \sigma_j r_j\right] && \text{(A.44)}\\
&= \frac{\hbar}{2r}\left(\sigma_i\sigma_j r_j - \sigma_j r_j \sigma_i\right) && \text{(A.45)}\\
&= \frac{\hbar}{2r}\left\{\left(\delta_{ij} + i\epsilon_{ijk}\sigma_k\right) r_j - \left(\delta_{ji} + i\epsilon_{jik}\sigma_k\right) r_j\right\} && \text{(A.46)}\\
&= \frac{\hbar}{2r}\left\{\left(r_i + i\epsilon_{ijk} r_j \sigma_k\right) - \left(r_i + i\epsilon_{jik} r_j \sigma_k\right)\right\} && \text{(A.47)}\\
&= \frac{i\hbar}{r}\epsilon_{ijk} r_j \sigma_k \quad . && \text{(A.48)}
\end{aligned}
$$

Therefore,

$$
[J_i,\ \hat{\sigma}\cdot\hat{r}] = 0 \quad . \tag{A.49}
$$

For $P = e^{i\phi}\gamma^0$,

$$
\begin{aligned}
\gamma^0\hat{\sigma}\cdot\hat{r} &= \hat{\beta}\frac{\hat{\sigma}_i r_i}{r} && \text{(A.50)}\\
&= -\frac{\hat{\sigma}_i r_i}{r}\hat{\beta} \quad . && \text{(A.51)}
\end{aligned}
$$

Therefore,

$$
[P,\ \hat{\sigma}\cdot\hat{r}]_+ = 0 \quad . \tag{A.52}
$$

Then, it naturally follows

$$
\begin{aligned}
J_i\hat{\sigma}\cdot\hat{r}\Omega_{jlm} &= \hat{\sigma}\cdot\hat{r}J_i\Omega_{jlm} \quad , \text{ and} && \text{(A.53)}\\
P\hat{\sigma}\cdot\hat{r}\Omega_{jlm} &= -\hat{\sigma}\cdot\hat{r}P\Omega_{jlm} \quad . && \text{(A.54)}
\end{aligned}
$$

This implies that $\hat{\sigma}\cdot\hat{r}\Omega_{jlm}$ has the same j and m of Ω_{jlm}, but it has the opposite parity. Therefore,

$$
\hat{\sigma}\cdot\hat{r}\Omega_{jlm} = -\Omega_{jl'm} \quad . \tag{A.55}
$$

Or, using κ introduced in the equation 2.53,

$$
\hat{\sigma}\cdot\hat{r}\Upsilon_{\kappa m} = -\Upsilon_{-\kappa m} \quad . \tag{A.56}
$$

Appendix B

Four-Current in Dirac Equation

B.1 Derivation of four-current density in Dirac Equation

The Dirac equation can be written as

$$i\hbar\frac{\partial\psi}{\partial t} = \frac{\hbar c}{i}\sum_{k=1}^{3}\hat{\alpha}_k\frac{\partial\psi}{\partial x^k} + m_0c^2\hat{\beta}\psi \quad . \tag{B.1}$$

And its conjugate is

$$-i\hbar\frac{\partial\psi^\dagger}{\partial t} = -\frac{\hbar c}{i}\sum_{k=1}^{3}\frac{\partial\psi^\dagger}{\partial x^k}\hat{\alpha}_k^\dagger + m_0c^2\psi^\dagger\hat{\beta}^\dagger \quad . \tag{B.2}$$

Multiplying the first equation by $\psi^\dagger$ from the left and the second equation by ψ from the right

$$i\hbar\psi^\dagger\frac{\partial\psi}{\partial t} = \frac{\hbar c}{i}\sum_{k=1}^{3}\psi^\dagger\hat{\alpha}_k\frac{\partial\psi}{\partial x^k} + m_0c^2\psi^\dagger\hat{\beta}\psi \quad , \text{ and} \tag{B.3}$$

$$-i\hbar\frac{\partial\psi^\dagger}{\partial t}\psi = -\frac{\hbar c}{i}\sum_{k=1}^{3}\frac{\partial\psi^\dagger}{\partial x^k}\hat{\alpha}_k^\dagger\psi + m_0c^2\psi^\dagger\hat{\beta}^\dagger\psi \quad . \tag{B.4}$$

Knowing $\hat{\alpha}^\dagger = \hat{\alpha}$ and $\hat{\beta}^\dagger = \hat{\beta}$, subtraction of the above equations from each other gives

$$i\hbar\frac{\partial}{\partial t}\left(\psi^\dagger\psi\right) = \frac{\hbar c}{i}\sum_{k=1}^{3}\frac{\partial}{\partial x^k}\left(\psi^\dagger\hat{\alpha}_k\psi\right) \quad . \tag{B.5}$$

By rearranging this equation,

$$\frac{\partial}{\partial t}\left(\psi^{\dagger}\psi\right)+\sum_{k=1}^{3}\frac{\partial}{\partial x^{k}}\left(c\psi^{\dagger}\hat{\alpha}_{k}\psi\right)=0 \quad . \tag{B.6}$$

Comparing this with the continuity equation,

$$\frac{\partial}{\partial t}\rho+\nabla\cdot\vec{j}=0 \quad . \tag{B.7}$$

gives the current density as

$$\vec{j}=c\psi^{\dagger}\hat{\alpha}_{k}\psi \quad . \tag{B.8}$$

Or, the continuity equation in covariant form with $\psi^{\dagger}\gamma^{0}=\bar{\psi}$, $\gamma^{0}=\hat{\beta}$ and $\gamma^{i}=\hat{\beta}\hat{\alpha}^{i}$ is written as

$$\frac{\partial}{\partial x^{i}}\left(c\bar{\psi}\gamma^{i}\psi\right)=0 \quad . \tag{B.9}$$

Then, the four current density is

$$j^{i}=c\bar{\psi}\gamma^{i}\psi \quad . \tag{B.10}$$

Appendix C

Ultra-relativistic Gas

C.1 Fermi Gas

The thermodynamic properties of an ultra-relativistic gas are obtained by the use of statistical mechanics. The logarithm of the grand partition function is

$$\ln Z = \sum_{\epsilon} \ln\left(1 + \exp\left\{-\beta\left(\epsilon - \mu\right)\right\}\right) + \sum_{\epsilon} \ln\left(1 + \exp\left\{-\beta\left(\epsilon + \mu\right)\right\}\right) \quad , \tag{C.1}$$

where

$$\mu = \textit{chemical potential} \tag{C.2}$$

$$\beta = \frac{1}{kT} \quad . \tag{C.3}$$

The total number of states of a Fermi gas of volume V in the phase space is

$$\Sigma = g \int \frac{d^3\vec{r} d^3\vec{p}}{h^3} = g \frac{4\pi V}{h^3} \int_0^\infty p^2 dp \quad . \tag{C.4}$$

Since the gas is ultra-relativistic, $\epsilon = pc$ Then,

$$\Sigma = g \frac{4\pi V}{h^3 c^3} \int_0^\infty \epsilon^2 d\epsilon \quad . \tag{C.5}$$

Therefore, the density of states is

$$g(\epsilon) = \frac{\partial \Sigma}{\partial \epsilon} = g\frac{4\pi V}{h^3 c^3}\epsilon^2 \quad . \tag{C.6}$$

Therefore, the equation C.1 can be written in the integral form

$$\ln Z = g\frac{4\pi V}{h^3 c^3}\int_0^\infty d\epsilon\, \epsilon^2 \left[\ln\left(1+\exp\left\{-\beta\left(\epsilon-\mu\right)\right\}\right) + \ln\left(1+\exp\left\{-\beta\left(\epsilon+\mu\right)\right\}\right)\right] \quad . \tag{C.7}$$

Integrating by parts,

$$\begin{aligned}
\ln Z &= g\frac{4\pi V}{h^3 c^3}\left[\frac{1}{3}\epsilon^3 \ln\left(1+\exp\left\{-\beta\left(\epsilon-\mu\right)\right\}\right)\right]_0^\infty \\
&+ g\frac{4\pi V}{h^3 c^3}\frac{\beta}{3}\int_0^\infty d\epsilon\, \frac{\epsilon^3}{1+\exp\left\{\beta\left(\epsilon-\mu\right)\right\}} \\
&+ g\frac{4\pi V}{h^3 c^3}\left[\frac{1}{3}\epsilon^3 \ln\left(1+\exp\left\{-\beta\left(\epsilon+\mu\right)\right\}\right)\right]_0^\infty \\
&+ g\frac{4\pi V}{h^3 c^3}\frac{\beta}{3}\int_0^\infty d\epsilon\, \frac{\epsilon^3}{1+\exp\left\{\beta\left(\epsilon+\mu\right)\right\}} \quad .
\end{aligned} \tag{C.8}$$

Since two surface terms are zero, it becomes

$$\ln Z = g\frac{4\pi V}{h^3 c^3}\frac{\beta}{3}\int_0^\infty d\epsilon\, \left[\frac{\epsilon^3}{1+\exp\left\{\beta\left(\epsilon-\mu\right)\right\}} + \frac{\epsilon^3}{1+\exp\left\{\beta\left(\epsilon+\mu\right)\right\}}\right] \quad . \tag{C.9}$$

Substituting $x = \beta(\epsilon-\mu)$ in the first term and $x = \beta(\epsilon+\mu)$ in the second term yields

$$\ln Z = g\frac{4\pi V}{h^3 c^3}\frac{\beta}{3}\left[\frac{1}{\beta}\int_{-\beta\mu}^\infty dx \frac{\left(\frac{x}{\beta}+\mu\right)^3}{e^x+1} + \frac{1}{\beta}\int_{\beta\mu}^\infty dx \frac{\left(\frac{x}{\beta}-\mu\right)^3}{e^x+1}\right] \tag{C.10}$$

$$\begin{aligned}
&= g\frac{4\pi V}{h^3 c^3}\frac{1}{3\beta^3}\left[\int_0^\infty dx \frac{(x+\beta\mu)^3}{e^x+1} + \int_0^\infty dx \frac{(x-\beta\mu)^3}{e^x+1}\right. \\
&\quad \left. + \int_{-\beta\mu}^0 dx \frac{(x+\beta\mu)^3}{e^x+1} - \int_0^{\beta\mu} dx \frac{(x-\beta\mu)^3}{e^x+1}\right]
\end{aligned} \tag{C.11}$$

$$\begin{aligned}
&= g\frac{4\pi V}{h^3 c^3}\frac{1}{3\beta^3}\left[\int_0^\infty dx \frac{2x^3+6\beta^2\mu^2 x}{e^x+1}\right. \\
&\quad \left. + \int_{-\beta\mu}^0 dx\, (x+\beta\mu)^3 \left(\frac{1}{e^x+1}+\frac{1}{e^{-x}+1}\right)\right]
\end{aligned} \tag{C.12}$$

$$= g\frac{4\pi V}{h^3 c^3}\frac{1}{3\beta^3}\left[\int_0^\infty dx \frac{2x^3+6\beta^2\mu^2 x}{e^x+1} + \int_{-\beta\mu}^0 dx\, (x+\beta\mu)^3\right] \quad . \tag{C.13}$$

Using the following facts

$$\int_0^\infty dx \frac{x^3}{e^x+1} = \frac{7\pi^4}{120} \quad , \tag{C.14}$$

$$\int_0^\infty dx \frac{x}{e^x+1} = \frac{\pi^2}{12} \quad , \text{ and} \tag{C.15}$$

$$\int_{-\beta\mu}^0 dx\,(x+\beta\mu)^3 = \frac{1}{4}\left[(x+\beta\mu)^4\right]_{-\beta\mu}^0 = \frac{1}{4}(\beta\mu)^4 \quad . \tag{C.16}$$

The equation C.13 becomes

$$\ln Z = g\frac{4\pi V}{h^3c^3}\frac{1}{3\beta^3}\left[2\frac{7\pi^4}{120} + 6\beta^2\mu^2\frac{\pi^2}{12} + \frac{1}{4}(\beta\mu)^4\right] \tag{C.17}$$

$$= \frac{gV}{h^3c^3}\frac{4\pi}{3}(kT)^3\left[\frac{7\pi^4}{60} + \left(\frac{\mu}{kT}\right)\frac{\pi^2}{2} + \frac{1}{4}\left(\frac{\mu}{kT}\right)^4\right] \quad . \tag{C.18}$$

After getting the grand partition function, it is very simple matter to get some properties of the gas. For example, to obtain the pressure of the gas, use the following relationship

$$\ln Z = \frac{pV}{kT} \quad . \tag{C.19}$$

The pressure is then

$$p = \frac{kT\ln Z}{V} \tag{C.20}$$

$$= \frac{g}{h^3c^3}\frac{4\pi}{3}(kT)^4\left[\frac{7\pi^4}{60} + \left(\frac{\mu}{kT}\right)\frac{\pi^2}{2} + \frac{1}{4}\left(\frac{\mu}{kT}\right)^4\right] \tag{C.21}$$

$$= \frac{g}{\hbar^3c^3}\frac{(kT)^4}{3}\left[\frac{7\pi^2}{120} + \left(\frac{\mu}{kT}\right)\frac{1}{4} + \frac{1}{8\pi^2}\left(\frac{\mu}{kT}\right)^4\right] \quad . \tag{C.22}$$

Similarly, the net number of fermions, N_{net}, could be calculated in the very similar manner.

$$
\begin{aligned}
N_{net} &= N_+ - N_- && \text{(C.23)}\\
&= g\frac{4\pi V}{h^3c^3}\int_0^\infty d\epsilon\ \left[\frac{\epsilon^2}{\exp\{\beta(\epsilon-\mu)\}+1}-\frac{\epsilon^2}{\exp\{\beta(\epsilon+\mu)\}+1}\right] && \text{(C.24)}\\
&= g\frac{4\pi V}{h^3c^3}\left[\frac{1}{\beta}\int_{-\beta\mu}^\infty dx\frac{\left(\frac{x}{\beta}+\mu\right)^2}{e^x+1}-\frac{1}{\beta}\int_{\beta\mu}^\infty dx\frac{\left(\frac{x}{\beta}-\mu\right)^2}{e^x+1}\right] && \text{(C.25)}\\
&= g\frac{4\pi V}{h^3c^3}\frac{1}{\beta^3}\left[\int_0^\infty dx\frac{(x+\beta\mu)^2}{e^x+1}-\int_0^\infty dx\frac{(x-\beta\mu)^2}{e^x+1}\right.\\
&\quad \left.+\int_{-\beta\mu}^0 dx\frac{(x+\beta\mu)^2}{e^x+1}+\int_0^{\beta\mu} dx\frac{(x-\beta\mu)^2}{e^x+1}\right] && \text{(C.26)}\\
&= g\frac{4\pi V}{h^3c^3}\frac{1}{\beta^3}\left[4\beta\mu\int_0^\infty dx\frac{x}{e^x+1}+\int_0^{\beta\mu} dx\,(x-\beta\mu)^2\right] && \text{(C.27)}\\
&= g\frac{4\pi V}{h^3c^3}\frac{1}{\beta^3}\left[4\beta\mu\frac{\pi^2}{12}+\frac{1}{3}(\beta\mu)^3\right] && \text{(C.28)}\\
&= g\frac{4\pi V}{h^3c^3}(kT)^3\left[\left(\frac{\mu}{kT}\right)\frac{\pi^2}{3}+\frac{1}{3}\left(\frac{\mu}{kT}\right)^3\right] && \text{(C.29)}\\
&= g\frac{V}{\hbar^3c^3}\left[\frac{1}{6}\mu(kT)^2+\frac{1}{6\pi^2}\mu^3\right] \quad . && \text{(C.30)}
\end{aligned}
$$

C.2 Bose Gas

By the same technique used for a fermion gas, the grand partition function for a Bose gas can also be obtained. The logarithm of the grand partition function is given as

$$\ln Z = -\sum \ln\left(1-\exp\{-\beta\epsilon\}\right) \quad . \qquad \text{(C.31)}$$

It can be changed to the integral form using the equation C.6.

$$
\begin{aligned}
\ln Z &= -g\frac{4\pi V}{h^3c^3}\int_0^\infty d\epsilon\,\epsilon^2\ln\left(1-\exp\{-\beta\epsilon\}\right) && \text{(C.32)}\\
&= -g\frac{4\pi V}{h^3c^3}\left[\frac{1}{3}\epsilon^3\ln\left(1-\exp\{-\beta\epsilon\}\right)\right]\\
&\quad +g\frac{4\pi V}{h^3c^3}\frac{\beta}{3}\int_0^\infty d\epsilon\,\frac{\epsilon^3}{\exp\{\beta\epsilon\}-1} && \text{(C.33)}\\
&= g\frac{4\pi V}{h^3c^3}\frac{1}{3\beta^3}\int_0^\infty dx\,\frac{x^3}{e^x-1} \quad . && \text{(C.34)}
\end{aligned}
$$

Using the following fact

$$\int_0^\infty dx\, \frac{x^3}{e^x - 1} = 6\frac{\pi^4}{90} \quad , \tag{C.35}$$

the grand canonical partition function is written as

$$\begin{aligned} \ln Z &= g\frac{4\pi V}{h^3c^3}\frac{2}{\beta^3}\frac{\pi^4}{90} && \text{(C.36)} \\ &= g\frac{8\pi V}{h^3c^3}\left(kT\right)^3\frac{\pi^4}{90} \quad . && \text{(C.37)} \end{aligned}$$

Using the equation C.19, the pressure of the Bose gas is

$$\begin{aligned} p &= \frac{kT\ln Z}{V} && \text{(C.38)} \\ &= g\frac{8\pi}{h^3c^3}\left(kT\right)^4\frac{\pi^4}{90} && \text{(C.39)} \\ &= \frac{g}{\hbar^3c^3}\left(kT\right)^4\frac{\pi^2}{90} \quad . && \text{(C.40)} \end{aligned}$$

Appendix D

Members of the BRAHMS Collaboration

I. G. Bearden[7], D. Beavis[1], C. Besliu[10], Y. Blyakhman[6], B. Budick[6], H. Bøggild[7], C. Chasman[1], C. H. Christensen[7], P. Christiansen[7], J. Cibor[3], R. Debbe[1], E. Enger[12], J. J. Gaardhøje[7], K. Hagel[8], O. Hansen[7], A. Holm[7], A. K. Holme[12], H. Ito[11], E. Jakobsen[7], A. Jipa[10], J. I. Jørdre[9], F. Jundt[2], C. E. Jørgensen[7], R. Karabowicz[4], T. Keutgen[8], E. J. Kim[1], T. Kozik[4], T. M. Larsen[12], J. H. Lee[1], Y. K. Lee[5], G. Løvhøiden[12], Z. Majka[4], A. Makeev[8], B. McBreen[1], M. Mikelsen[12], M. Murray[8], J. Natowitz[8], B. S. Nielsen[7], J. Norris[11], K. Olchanski[1], J. Olness[1], D. Ouerdane[7], R. Płaneta[4], F. Rami[2], C. Ristea[10], D. Röhrich[9], B. H. Samset[12], D. Sandberg[7], S. J. Sanders[11], R. A. Sheetz[1], P. Staszel[7], T. F. Thorsteinsen[9+], T. S. Tveter[12], F. Videbæk[1], R. Wada[8], A. Wieloch[4], and I. S. Zgura[10]

[1] Brookhaven National Laboratory, Upton, New York 11973, [2] Institut de Recherches Subatomiques and Université Louis Pasteur, Strasbourg, France, [3] Institute of Nuclear Physics, Krakow, Poland, [4] Jagiellonian University, Krakow, Poland, [5] Johns Hopkins University, Baltimore, Maryland 21218, [6] New York University, New York, New York 10003, [7] Niels Bohr Institute, University of Copenhagen, Denmark, [8] Texas A&M University, College Station, Texas 77843, [9] University of Bergen, Department of Physics, Bergen, Norway, [10] University of Bucharest, Romania, [11] University of Kansas, Lawrence, Kansas 66045, [12] University of Oslo, Department of Physics, Oslo, Norway, [+] *Deceased*